OPTICAL SPECTROSCOPY OF WIDE-BAND-GAP SEMICONDUCTORS: RAMAN AND PHOTOLUMINESCENCE OF GALLIUM NITRIDE, ZINC OXIDE AND THEIR NANOSTRUCTURES

Except where reference is made to the work of others, the work described in this dissertation is my own or was done in collaboration with my advisory committee. This dissertation does not include proprietary or classified information.

_____

Dake Wang

Certificate of Approval:

_____	_____
Chin-Che Tin Professor Physics	Minseo Park, Chair Assistant Professor Physics
_____	_____
Jianjun Dong Associate Professor Physics	John Williams Professor Physics

_____

Joe F. Pittman
Interim Dean
Graduate School

OPTICAL SPECTROSCOPY OF WIDE-BAND-GAP SEMICONDUCTORS: RAMAN AND PHOTOLUMINESCENCE OF GALLIUM NITRIDE, ZINC OXIDE AND THEIR NANOSTRUCTURES

Dake Wang

A Dissertation

Submitted to

the Graduate Faculty of

Auburn University

in Partial Fulfillment of the

Requirement for the

Degree of

Doctor of Philosophy

Auburn, Alabama
December 15, 2006

OPTICAL SPECTROSCOPY OF WIDE-BAND-GAP SEMICONDUCTORS: RAMAN AND PHOTOLUMINESCENCE OF GALLIUM NITRIDE, ZINC OXIDE AND THEIR NANOSTRUCTURES

Dake Wang

_____
Signature of Author

_____
Date of Graduation

DISSERTATION ABSTRACT

OPTICAL SPECTROSCOPY OF WIDE-BAND-GAP SEMICONDUCTORS: RAMAN AND PHOTOLUMINESCENCE OF GALLIUM NITRIDE, ZINC OXIDE AND THEIR NANOSTRUCTURES

Dake Wang

Doctor of Philosophy, December 15, 2006
(B.S. Sichuan University, Chengdu, China, August 1997)

164 Typed Pages

Directed by Minseo Park

Micro-Raman and photoluminescence (PL) were performed to study GaN and ZnO and their nanostructures. Various ZnO nanostructures were successfully synthesized at low temperatures using thermal chemical vapor deposition method. The ultraviolet lasing in optically pumped ZnO nanonails was observed for the first time. The lasing threshold was found to be 17 MW cm^{-2}. Very sharp emission peaks (full width at half maximum of 0.08 nm) were observed in the emission spectrum, indicating a high Q factor of the cavity formed by the hexagonally shaped nanonail head. The analysis of the lasing spectra strongly suggests the whispering gallery mode lasing from a hexagonally shaped head of the single ZnO nanonails. The as-grown ZnO nanorods

were thermal annealed under different ambient conditions and their photoluminescence were collected after each annealing processes. The observed change in photoluminescence strongly suggests that positively charged impurity ions or interstitial Zn ions are the recombination centers for green luminescence observed in the present sample. A model based on the interplay between the band bending at the surface and the migration of positively charged impurity ions or Zn ions was proposed, which satisfactorily explains the observed photoluminescence. Raman scattering was performed to study the aligned GaN nanorods grown by plasma-assisted molecular-beam epitaxy. It was determined from the E_2 peak that the GaN nanorods are relatively strain free. The free carrier concentration, as well as electron mobility was obtained by the line shape analysis of the coupled A_1(LO) phonon plasmon mode for the first time for semiconductor nanostructures. Since the position of the LO phonon peak was found to be dependent on both the temperature and the LO phonon-plasmon coupling, special attention has been paid to exclude the temperature-induced peak shift. The local temperature of the nanorod sample was estimated based on the ratio of Stokes to anti-Stokes Raman peak intensity. GaN MISFET with re-grown by selected area MOVPE n^+ layer has been analyzed by micro-Raman and micro-PL. The material properties were extracted by using both spectroscopies.

ACKNOWLEDGEMENTS

The author would like to extend his deepest thanks to Dr. Minseo Park for his supervising this dissertation and being a great academic advisor during the author's graduate study in Auburn University.

The author would like to thank Ms. Hee Won Seo and Mr. An-jen Cheng for their contributions on the thermal CVD system and the growth of ZnO nanostructures. The author would like to thank Mr. N. Sathitsuksanoh for helping with XRD experiment.

The author would like to express his appreciation to Mr. Yi Zhou, Dr. Chin-Che Tin, Dr. Jianjun Dong, Dr. John Williams, Dr. German Mills and Dr. An-ban Chen for their help and discussion.

The author would like to express his appreciation to Dr. Jungho Park, Dr. Jooho Moon, Dr. Y. N. Saripalli, Dr. M. A. L. Johnson, Dr. Y. S. Park, Dr. C. M. Park, Dr. T. W. Kang, and Dr. W. -C. Yang for their contribution of various samples investigated in this dissertation work.

Style manual or journal used: Bibliography conforms to those of the Journal of Applied Physics

Computer software used: Microsoft Word 2003 for Windows

TABLE OF CONTENTS

LIST OF FIGURES

LIST OF TABLES

CHAPTER 1

INTRODUCTION

The research community has witnessed a surge of research activities in semiconductor nanostructure materials in recent years. Carbon nanotubes and derivatives of them have been one of the major interests of the semiconductor nanomaterial research community for many years. Recently, more and more effort has been invested to study nanostructures made of wide-band-gap semiconductors such as GaN and ZnO, as demonstrated by a myriad of publications in this field.

Wide-band-gap semiconductor nanostructures have been attracting intensive attention because of their unique properties resulting from the low dimensionality and the advantages provided by the wide-band-gap semiconductor materials. Nanostructures with size range from submicron to a few nanometers have the same lattice constants and crystal structures as their bulk counterparts, which are confirmed by X-ray diffraction and transmission electron microscopy. Thus, many bulk properties are still preserved. However, their very large surface to volume ratio makes their physical, optical and electrical properties markedly different from their bulk counterpart. Furthermore, one nanostructure unit is usually one continuous piece of single crystal, which is in sharp contrast with the structural defects ridden wide-band-gap semiconductor bulk materials.

The electron-hole interaction will also be greatly enhanced due to the increased electronic density of states. Similar enhancement occurs for the electron-phonon interactions. With the size of the nanostructures shrunken to a few nanometers or smaller, quantum confinement effects of charge carriers and lattice vibrations begin to strongly affect their behaviors. With such a small volume, no constituent atoms in a nanostructure are very far from the surface. It can therefore be expected that the surface electronic and vibrational modes will play significantly more important roles in the case of nanostructures.

Wide-band-gap semiconductors such as diamond, silicon carbide, gallium nitride and zinc oxide etc. possess a band gap larger than 2 eV. Many wide-band-gap semiconductors lie on the boarder line between semi-insulators and semiconductors. However, their electronic properties can be tailored by proper doping. Their low intrinsic carrier concentrations and high breakdown voltage allow high-temperature and high-power applications (diamond, silicon carbide etc.). For direct-band-gap materials such as gallium nitride and zinc oxide, the high electronic energy of band-to-band transitions allows emission in the green, blue, or even UV region of the spectrum. In addition, many of these materials have favorable mechanical and thermal characteristics.

The novel properties possessed by semiconductor nanostructures such as the greatly enhanced Purcell factor can be exploited in a plethora of optoelectronic applications. Optoelectronic devices such as light-emitting-device and laser diode based on bulk or thin film gallium nitride have been commercially available. Zinc oxide has been used as phosphorescent material for years. The interest in this material has been rekindled due to its room temperature excitonic emission capability and many other material merits. In spite of the success of gallium nitride based devices and the progress

made in zinc oxide research, the science and technology of the wide-band-gap semiconductor nanostructures optoelectronics is still far from mature. Many problems, from the material preparation to the device fabrication as well as the basic physics related to those materials remained unsolved. The optical properties of these materials need to be elucidated to improve their applications in optoelectronics. In spite of the wide spread use of gallium nitride and zinc oxide, the understanding of their physical properties, including many crucial optical properties, is still very limited. Even less has been understood for their nanostructures.

In this dissertation, the light-matter interaction occurring in gallium nitride and zinc oxide, as well as their nanostructures, has been studied by optical spectroscopy such as photoluminescence and Raman spectroscopy. The mechanisms of many important optical processes have been studied in detail. Optical spectroscopy was also employed as a useful tool to extract valuable information from the materials. The structure of the dissertation is outlined as follow.

The synthesis of zinc oxide nanostructures is described in Chapter 3. Two different thermal chemical vapor deposition growth systems are introduced. The morphologies and sizes of the as-grown zinc oxide nanostructures were analyzed. The visible luminescence of zinc oxide nanostructures synthesized by the two different growth systems was studied, including the effect of different native defects introduced under oxygen-deficient and oxygen-rich growth environments. Raman scattering experiments were performed on zinc oxide nanostructures. Raman spectra collected from zinc oxide nanostructures were compared with that of zinc oxide bulk crystals. Various broadening and enhancement effects in different Raman modes were discussed. Since the

longitudinal optical phonons are capable of ionizing the free exciton in zinc oxide, a better understanding of optical phonon modes and their interaction with other elemental excitations in zinc oxide nanostructures is necessary if room temperature excitonic emission is to be achieved. Correlations between the morphologies and the luminescence/Raman characteristics of the nanostructures were discussed. The uniformity of the samples in terms of optical properties was also discussed for the two different growth systems.

In Chapter 4, one zinc oxide nanostructure (nanonail) was studied for lasing characteristics. Ultraviolet lasing involving the whispering-gallery-mode in optically pumped ZnO nanonails has been demonstrated. This is the first time that ultraviolet lasing in whispering-gallery-mode has ever been observed in ZnO nanostructures. Since zinc oxide nanostructure ensembles are known to be able to achieve ultraviolet lasing *via* a random lasing mechanism, special care has been taken to exclude the possibility of such lasing. Theoretical models based on the plane-wave approximation were employed to study the resonant modes formed in the nanonail cavity. Results have shown that classical models are still valid in nanostructures with size comparable to the wavelength of the light. Ultra-sharp emission peaks were observed in the spectrum of a single nanonail, indicating a high quality factor of the cavity formed by the hexagonally shaped nanonails. The emission characteristics of the tightly confined whispering-gallery-mode were found to be very different from that of the leaky Fabry-Perot mode usually found in zinc oxide nanostructures. The lasing threshold was determined by varying the power density of the excitation laser.

The controversial topic of the blue-green visible luminescence of zinc oxide was explored in Chapter 5. Post-growth annealing was carried out to investigate the photoluminescence of ZnO nanorod samples, synthesized by the oxygen-deficient growth system, which exhibit strong blue-green luminescence. Thermal annealing in oxygen-deficient/oxygen-rich ambient conditions is a useful tool to study non-stoichiometry related defects in zinc oxide. Numerous research papers have been published that report on the effect of thermal annealing on the luminescence properties of zinc oxide, although the results were often inconsistent and even contradictory. Two crucial aspects have been neglected in previous research on this topic. The first aspect is the inevitable change in the surface adsorption of various gas species during the annealing process and consequently the change in the surface band bending, which can not be omitted due to the large-surface-to-volume ratio of the nanostructures. The second aspect is the dynamics and the mobility of point defects in zinc oxide, and consequently their spatial distributions in the nanostructures. In spite of existing evidence which indicate that some point defects can easily diffuse or migrate under the influence of electric field and/or the elevated temperature, no attention has been paid to this point. In our work, a model based on the interplay between band bending near the surface and migration of positively charged impurity ions or zinc ions was proposed, which satisfactorily explained the observed photoluminescence. The observed change in photoluminescence after annealing the samples strongly suggested that positively charged impurity ions or interstitial zinc ions are the recombination centers for the blue-green luminescence observed in our zinc oxide sample. The large surface-to-volume ratio and structural stability provided by the

nanostructures were important for the success of the annealing experiment and the correct interpretation of the luminescence.

In Chapter 6, we have investigated the Raman scattering of aligned GaN nanorods. It was determined by Raman spectroscopy that the GaN nanorods are relatively strain-free. The free carrier concentration as well as electron mobility of the GaN nanorods were obtained by line shape analysis of coupled A_1(LO) phonon-plasmon mode. It was the first time for this Raman scattering-based characterization technique to be applied on semiconductor nanostructures. Electrical measurements have been carried out to determine the electronic parameters of semiconductor nanostructures. However, good repeatable electrical contacts were by no means easily achievable. Our characterization technique thus provides a non-contact, non-destructive alternative. Since the position of the LO phonon peak was found to be dependent on both the temperature and the LO phonon-plasmon coupling, it is crucial to consider the temperature effect in determining the frequency of the uncoupled LO phonon mode for the line shape analysis. The local temperature of the nanorod sample was estimated based on the ratio of Stokes to anti-Stokes Raman peak intensity.

In Chapter 7, micro-Raman and micro-photoluminescence spectroscopy were used collectively to analyze a gallium nitride based metal-insulator-semiconductor field-effect-transistor. The source and drain regions of this device were constructed by the re-grown gallium nitride n^+ layer grown by selected area metal-organic-vapor-phase-epitaxy. The material properties of the re-grown gallium nitride n^+ layer and the intrinsic gallium nitride layer in the re-grown region were extracted by using both spectroscopies. The free-carrier concentration of the re-grown layer and the intrinsic layer were

determined by line shape analysis of the coupled plasmon-phonon mode to be 4.7×10^{17} cm^{-3} and $< 3 \times 10^{16}$ cm^{-3} respectively. The silicon dopant concentration in the re-grown layer was found to be 2×10^{19} cm^{-3} by the red-shift in the photoluminescence peak. Both Raman and PL spectrum show that the deposited gallium nitride layer is of very high quality. The two spectroscopies can complement each other, and the result obtained by one can be crosschecked by the other. This chapter presented a very useful optical analytical method for wide-band-gap semiconductor material and device analysis, as well as a comprehensive review of Raman and photoluminescence spectroscopy.

CHAPTER 2

LITERATURE REVIEW

Zinc oxide is a group II-VI binary compound semiconductor, and belongs to the C_{6v}^4 space group.[1] Zinc oxide crystals may take the wurtzite structure (hexagonal symmetry), zinc blende (cubic symmetry), and rock salt structure (cubic symmetry). Unless under high pressure, zinc oxide crystals will stabilize in the wurtzite structure. However, zinc blende structure can be formed by growth on a cubic substrate.[2, 3, 4] As a result of the sp^3 hybridization of the oxygen 2p orbital and zinc 3d orbital, each oxygen/zinc ion is surrounded by four zinc/oxygen ions at the corners of a tetrahedron, in zinc blende or wurtzite structures. The chemical bonding between zinc and oxygen has mixed character of the covalent and ionic bonding. The crystal structure of zinc oxide does not possess any inversion symmetry, thus it is a piezoelectric material.

The wurtzite structure has a hexagonal unit cell with two lattice constants. At room temperature, the lattice constant a = 0.32495 nm, and is in the basal plane; the lattice constant c = 0.52069 nm, and is in the direction of c-axis. The c/a ratio is 1.602, which is close to the 1.633 ratio of the ideal hexagonal closed packed structure.[5, 6] The wurtzite structure is composed of two interweaving hexagonal closed packed sublattices of zinc and oxygen. Each sublattice has unit cells with four like atoms. The two sets of

sublattices are separated by u = 0.3825 in fractional coordinates along the c-axis. The value of u in zinc oxide crystals is deviated from the ideal wurtzite structure (u = 0.375). The parameter u is related to the c/a ratio in such a way that the four tetrahedral distances remain unchanged by the difference in c/a ratio which is affected by the electronegativities of zinc and oxygen.[7] The (0001) crystal plane of zinc oxide is terminated with zinc, and the (000$\underline{1}$) plane is terminated with oxygen. The polar nature of the crystal leads to vastly different surface properties of these two planes.

The (0001) planes in zinc oxide possess the highest surface energy among the low-index planes provided that no surface reconstruction or passivation has taken place. As a result, the zinc oxide nanostructures usually have the highest growth rate along the c-axis so as to minimize the surface area of the (0001) planes. This has been most commonly observed in the vapor phase growth process.

At T = 300K, the wurtzite structure of zinc oxide has a direct bandgap of 3.37 eV. The direct interband transition takes place between the bottom of the lowest conduction band and the top of the valence band at the Γ point in the Brillouin zone. The lowest conduction band of zinc oxide is s-type, whereas the valence band is a six-fold degenerate p-type and is split into three subbands due to spin-orbit interaction and crystal-field effect.[8]

The bandgap of zinc oxide can be tuned from 2.8 to 4.0 eV by alloying with cadmium and magnesium. The bandgap of zinc oxide can be widened by alloying zinc oxide with magnesium oxide which has a wider bandgap of 7.7 eV,[9] or narrowed by alloying with cadmium oxide which has a smaller bandgap of 2.3 eV.[10] The problem with zinc oxide/magnesium oxide alloying is the limited solubility of magnesium in zinc oxide

(< 4 mol %).[11] The different crystal structure of magnesium oxide (cubic structures) presents another problem.

At room temperature, the highest electron and hole mobility in bulk zinc oxide single crystals was determined by Hall measurement to be 205 and 180 $cm^2 \cdot V^{-1} \cdot s^{-1}$, respectively.[12,13] This value is comparable to the theoretical value of the room temperature electron mobility (~300 cm^2/Vs) predicted by Monte Carlo simulations. Compared with bulk zinc oxide, the room temperature electron mobility of zinc oxide epilayers is lower (< 100 cm^2/Vs).[14] It was found that the surface roughness of the film was related with its electrical properties, and the mobility was increased with increasing grain size. The saturation electron drift velocity in zinc oxide is 3×10^7 cm/s, which is comparable to that of gallium nitride.[15]

Wurtzite zinc oxide is a native n-type semiconductor due to the deviation from stoichiometry. Nominally undoped zinc oxide can have a very high electron concentration on the order of 10^{21} cm^{-3}.[16] It has been shown that zinc interstitial rather than oxygen vacancy is the dominant native shallow donor in zinc oxide with an ionization energy of about 30-50 meV.[17] However, it is still under debate as which native defect is the dominant donor.[18] It has been suggested that the n-type conductivity of unintentionally doped zinc oxide is mainly from hydrogen with ionization energy about 30 meV.[19,20] n-type doping in zinc oxide can be achieved by doping with group III elements (aluminum, gallium, and indium can substitute zinc), or by doping with group VII elements (chlorine and iodine can substitute oxygen).[21,22,23] High-quality high-conductive zinc oxide films have been produced by doping with aluminum, gallium and indium. Some films grown by a metal-organic-chemical-vapor-deposition method have

achieved a resistivity as low as 1.2×10^{-4} Ω cm.[24] With the high level of background n-type conductivity presented in zinc oxide, p-type doping of zinc oxide is quite difficult, as always encountered in wide-band-gap semiconductors. P-type doping may be achieved by substituting zinc sites by group I elements such as lithium and sodium, or by substituting oxygen sites with group V elements such as nitrogen, phosphorous and arsenic.[25, 26, 27]

The growth of high quality bulk zinc oxide crystals is relatively easier to achieve as compared with that of gallium nitride. Bulk zinc oxide crystals can be grown by hydrothermal,[28, 29] vapor phase,[30, 31] and hydride/halide vapor-phase epitaxy.[32, 33] Among them, the hydrothermal growth is more suited for growth of large zinc oxide crystal. Its drawback is the inevitable incorporation of alkali metals into zinc oxide. The growth is anisotropic with the highest growth rate in the [0001] direction (~0.25 mm/day).[34] Very high quality bulk zinc oxide can be produced *via* a vapor transport growth process.[35] Polycrystalline zinc oxide thin films can be deposited by magnetron sputtering[36] and chemical vapor deposition.[37] Improved sputtering techniques such as radio-frequency magnetron sputtering[38] and other deposition techniques such as molecular-beam epitaxy,[39] pulsed-laser deposition,[40] and metal organic chemical vapor deposition[41] are capable of producing high quality zinc oxide single crystal films.

The self-assembled of zinc oxide nanostructures can be achieved by using a variety of growth techniques, and almost all of the growth techniques used for zinc oxide thin film growth can be employed to synthesize zinc oxide nanostructures. The various growth techniques of zinc oxide can be categorized based on the different growth mechanisms such as vapor-liquid-solid, vapor-solid, and catalyst-free self-nucleation

process. Vapor-liquid-solid growth is probably the most widely used method, in which the metal catalyst particles are used to assist the growth of the nanostructures. Transmission electron microscopy reveals the existence of metal nanoparticles on the top of the nanostructures synthesized via vapor-liquid-solid process.[42,43,44] Various metals such as gold, silver, copper and transition metals can be used as a catalyst.[45,46,47] Due to the eutectic phase formed by the metal alloy, liquid alloy droplets are formed at the initial stage of the growth process. Following the formation of the liquid alloy droplets, gaseous species are absorbed onto the liquid droplets. Nucleation centers are formed upon supersaturation of the liquid alloy. With continuous feeding of reactant species, nanostructures start to grow from the nucleation sites. The diameter of the nanowire synthesized via vapor-liquid-solid growth largely depends on the size of the liquid alloy droplet.[48] In the case of catalyst-free growth, zinc oxide nucleation takes place on the surface of the substrate. Epitaxial growth is possible on lattice-matched substrates. The growth rate of the vapor-solid process is much lower than that of the vapor-liquid-solid process due to a less efficient absorption of reactant at the nucleation sites. In the vapor-solid process, crystal growth takes place at the interface of solid and vapor, whereas it takes place at the interface of solid and liquid in vapor-liquid-solid process.

The intrinsic optical properties of zinc oxide are related to the electronic transition involving free electrons and holes, as well as free and bound excitons. The free exciton binding energies associated with the A (heavy hole), B (light hole) and C (crystal-field split band) valence bands are 63, 50 and 49 meV, respectively.[49] The exciton binding energies are much larger than the room temperature thermal energy (25 meV), making the excitonic recombination processes possible even at room temperature, whereas in

other wide-band-gap semiconductor such as gallium nitride, the electron-hole-plasma transition is the dominate recombination processes. Since the separated electrons and holes are more vulnerable to be trapped by the various defects presented in the crystal, it is desirable to have a material with a large exciton binding energy for optoelectronic applications. Low-temperature absorption,[50,51] reflection[52,53] photoreflectance,[54,55] and photoluminescence[56,57,58] spectroscopies were usually employed to study the transition energies related to the intrinsic excitons in zinc oxide. Low-temperature (< 10K) photoluminescence has revealed multiple emission lines resulting from the electronic transitions near the band edge. They include free excitonic emissions and their phonon replicas, neutral donor bound excitons, neutral acceptor bound excitons, two-electron satellites, shallow donor-shallow acceptor pair transitions, and so on. At room temperature, all the aforementioned emission lines are not resolved, and only a relatively broad and featureless emission band can be seen. Although the exciton binding energy of zinc oxide is very large, the energy of its longitudinal optical phonon is equally energetic (72 meV). The free excitons can be easily ionized upon scattering by longitudinal optical phonons. It was found that the electro-phonon coupling strength decreases with decreasing size of the zinc oxide nanostructures.[59] This fact implies that a more reliable excitonic recombination processes can exist in zinc oxide nanostructures than in zinc oxide bulk. Zinc oxide strongly absorbs photons with energy larger than the band gap, and the absorption coefficient was found to be ~160,000 cm^{-1} at 325 nm.[60]

The extrinsic optical properties of zinc oxide are related to the native point defects, impurities and other defects. These defect states form discrete energy levels in the band gap. Some of them can be expressed through visible luminescence *via* radiative

recombination processes. The mechanism of the defect related electron-hole recombination process in zinc oxide has been intensively investigated, and yet it still remains a controversial subject. Among the different mechanisms proposed to explain the visible luminescence, oxygen vacancies have been widely considered as the most probable candidate, although no consensus could be reached regarding the charge state of the oxygen vacancy; *i.e.*, singly ionized[61] or doubly ionized oxygen vacancy[62]. Oxygen annealing was usually employed to modify the level of oxygen deficiency in zinc oxide. However, contradictory results regarding the effect of annealing on the luminescence property of zinc oxide have been reported. In some experiments,[63, 64, 65] oxygen annealing has enhanced the intensity of the visible luminescence band and has reduced the intensity of the band edge ultraviolet luminescence band. However, in some other experiments, the exact opposite trend was observed.[66, 67] It was also found that the change in relative intensities of the visible and ultraviolet luminescence band depends on the annealing temperature.[68, 69]

Recently, optically pumped room temperature stimulated emission and lasing have been reported in many zinc oxide nanostructures where zinc oxide serves as both the active material (gain material) and optical cavity. In the lasing actions reported, most of the cavities formed by zinc oxide nanostructures exhibits a Fabry-Perot type of resonance in which the top and bottom facets of the nanostructure serve as two reflecting mirrors while the sidewall of the structure provides lateral confinement.[70,71,72,73] On the other hand, random lasing is also observed in samples with a high density of nanowires.[74,75] The cavity formed by the two end facets of zinc oxide nanowires cannot provide a high level of confinement due to the limited reflectivity at the end facets for normal incident

light, and the high diffraction loss when the lateral size of the cavity is much smaller than the wavelength. This results in a relatively low quality factor.[76] It has been shown that whispering gallery modes possess a very high quality factor, where light is confined on the circumference of a dielectric disk or sphere.[77,78] Lasing in whispering gallery modes has been observed in both gallium nitride microdisks[79] and a hybrid zinc oxide/silica microdisk.[80] Very recently, the presence of whisper gallery modes has been demonstrated in tapered zinc nanoneedles with hexagonal cross section and a lateral size even smaller than the wavelength,[81] although the spectra only show broad emission bands in the visible spectral range and no lasing action was reported.

CHAPTER 3

GROWTH AND CHARACTERIZATION OF ZINC OXIDE NANOSTRUCTURES

3.1 Introduction

Zinc oxide (ZnO) has been recognized as an important functional material which has applications in sensors,[82] solar cells,[83] surface acoustic wave devices,[84] and varistors[85]. ZnO is a semiconductor with a large band gap of 3.37 eV and a large exciton binding energy of 60 meV as compared with thermal energy at room temperature (25 meV), making it a promising material for UV laser and optoelectronic application. Recently, there has been a vigorous research activity in the growth of ZnO nanostructures. Some of the well established growth methods for ZnO nanowire and nanoprticle are the vapor-liquid-solid (VLS) growth,[86,87] metal-organic vapor-phase epitaxy (MOVPE),[88,89] plasma-assist chemical vapor deposition,[90] metalorganic chemical vapor deposition,[91] pulsed laser deposition,[92] electrophoretic deposition,[93] and spray pyrolysis[94] etc. In some of these processes, nanoparticles of Au or Ni are frequently utilized as catalysts. However, ZnO nanowires have also been successfully synthesized using thermal evaporation even without a metal catalyst.[95]

Recently, Yao *et al*. has produced needle-like rods with a hexagonal head at 750-800˚C *via* thermal evaporation.[96] Very recently, Lao *et al.* have also synthesized nail

shaped nanorods at 950-970˚C using a thermal evaporation and condensation.[97] The nanostructure was named "nanonail" due to the similarity of its morphology to a nail. However, these growth processes require a relatively high temperature, and there is a scarceness of optical and electrical properties of these samples reported. The luminescence and Raman spectroscopy of ZnO nanostructures demonstrate different characteristics from its bulk or thin film counterparts due to their very large surface to volume ratio, the intrinsic defects presented in the materials, the strong electric field from band bending and other unique properties. In nanostructures with size of a few nanometers or smaller, quantum confinement can occur for both the charge carriers and optical phonons leading to emission or scattering peak shift and broadening in luminescence and Raman spectra. Some ZnO nanostructures such as nanonail and nanopillar possess well-formed crystal facets, thus providing an ideal dielectric cavity for photon confinement. With such a resonant cavity and the high optical gain provided by ZnO, room temperature lasing can be achieved in the ultra-violet spectral range.[98] Some ZnO nanostructures such as nanoneedles provide excellent platforms for field emission applications. ZnO nanostructures are unintentionally n-typed doped and possess good electric conductivity, and their resistance to ion bombardment making them especially attractive for field emission applications in poor vacuum and a low pressure air environment.[99] When studying ZnO nanostructures, it is important to realize that the optical and electrical properties of these structures are profoundly affected by their surface conditions, more specifically their ambient environment.

In this work, we have successfully synthesized ZnO nanostructures at a relatively low temperature (450-700˚C) *via* thermal CVD process, and performed optical

characterization such as Raman and photoluminescence spectroscopy. The as-grown ZnO nanostructures were also analyzed by scanning electron microscopy and X-ray diffraction measurement. The ZnO nanostructures studied in the present research were grown by Ms. Hee Won Seo and Mr. An-jen Cheng.

3.2 Thermal CVD deposition of ZnO nanostructures

The synthesis of ZnO nanonails has been carried out using a single-zone resistive heating tube furnace (Lindberg, 54233) (Figure 3.1). Zinc powder (99.998%, Aldrich) was placed in an alumina boat ($10\times1.5\times1$ cm^3) located inside the quartz tube reactor (~1 m long, and an inner diameter of 5 cm). Argon gas (Grade 5) was used as carrier gas; the gas flow rate was controlled by a mass flow meter from 500 sccm to 1000 sccm. The residual oxygen in the reactor tube and in the partially oxidized zinc powder, and/or in the Ar gas was used as the oxygen source. The residual water vapor inside the reactor tube also participated as a reagent in the growth of ZnO (the reactor tube was not baked before the deposition). There are two possible reactions involved in the growth of ZnO:

$$Zn + O_2 \rightarrow ZnO \qquad (3.1)$$

$$Zn + H_2O \rightarrow ZnO + H_2 \qquad (3.2)$$

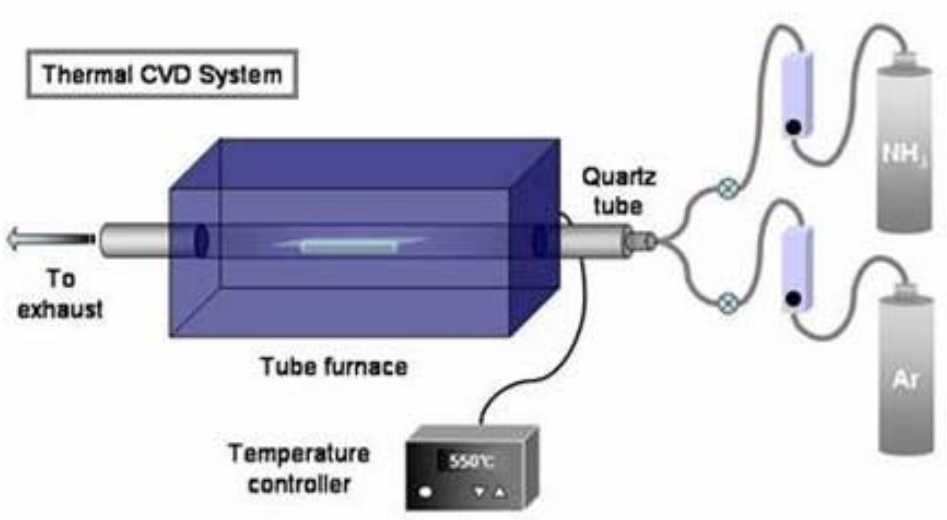

Figure 3.1: Schematic diagram of the thermal CVD system for ZnO nanonail synthesis (NH_3 is used for etching of the sputtered catalytic metallic layer, and is *not* used during the deposition of ZnO).

Silicon wafers were cleaned by the RCA wafer cleaning process, dipped in deionized water for 15 min, and then dried by flowing nitrogen. For catalyst-assisted deposition, Si substrates [(100) or (111)] were treated with $NiCl_2 \cdot 6H_2O$ (99.999%) or $HAuCl_4 \cdot 3H_2O$ solution (solution concentrations vary from 0.01 M to 1 M, Figure 3.2). As an alternative, Si substrates were coated with Ti or Pt by sputtering. The as-sputtered Si substrates were etched in flowing ammonia to form nanometer-sized metal islands. The prepared substrate was then placed on top of the boat which contained the zinc powder. All chemicals were used as delivered without further purification.

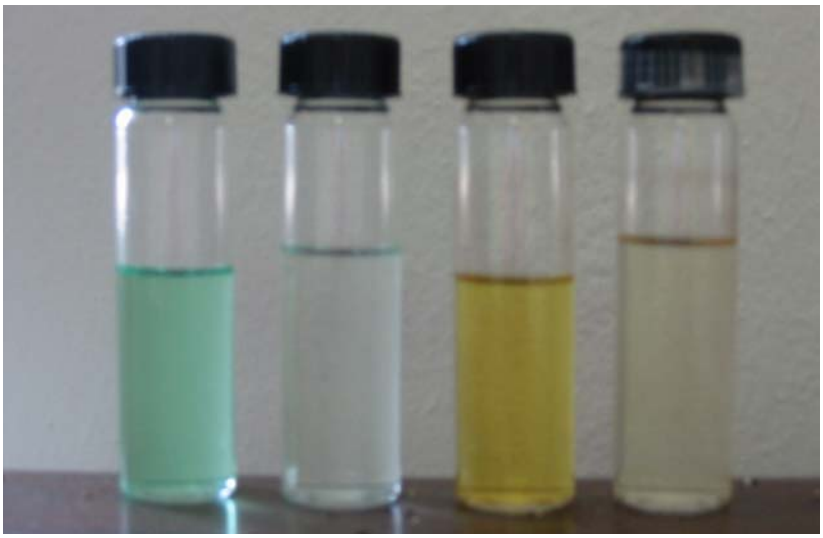

Figure 3.2: As-prepared catalyst solutions, from left to right: $NiCl_2 \cdot 6H_2O$ (0.1 M), $NiCl_2 \cdot 6H_2O$ (0.01 M), $HAuCl_4 \cdot 3H_2O$ (0.01 M), $HAuCl_4 \cdot 3H_2O$ (0.001 M).

Prior to heating the samples, the tube was purged with Argon gas for 10 min at a flow rate of from 100 sccm to 1000 sccm. The temperature of the furnace was set within the range from 450 to 700^{o}C. The alumina boat was placed in the middle section of the tube furnace where the temperature of the furnace was uniform and closest to the set point as measured by a thermocouple. The average rate at which the furnace temperature was ramped is usually at about 30^{o}C per min. Once the desired temperature was reached, it was maintained at the set point for 30 min to 1 hr. After the furnace was turned off, the tube was kept filled with by Argon gas until the sample cooled down to the room temperature.

The catalyst-assisted synthesis of ZnO nanostructures takes four steps. First, $NiCl_2 \cdot 6H_2O$ or $HAuCl_4 \cdot 3H_2O$ ethanol solution is dispersed on a Si (100) wafer, forming a thin film of solution on the substrate. Upon heating to 450-500^{o}C in the furnace,

$NiCl_2 \cdot 6H_2O$ or $HAuCl_4 \cdot 3H_2O$ thermally decomposes and Ni or Au particles are formed *via* the Ostwald ripening process.[100] These islands can be made from an eutectic metal-Si alloy droplets with diameters of tens of nanometers.[101] As the temperature is ramped up (> 419°C), Zn vapor is formed in the tube; which then preferentially adsorbs and condenses on the Ni or Au nanoparticles. The whole nucleation can be described as a Vapor-Liquid-Solid (VLS) process with the help of catalytic particles to reduce the surface free energy. Following the nucleation, ZnO starts to grow from the nuclei provided, there is sufficient supply of reactants. ZnO will largely grow along c axis due to the faster growth rate along that direction than the lateral direction. The incremental growth of ZnO nanowires taking place at the droplet interface constantly pushes the catalyst particles upwards.

If the catalyst is not consumed during the deposition, instead of a VLS process, the ZnO growth follows a Vapor-Solid (VS) process in which the zinc vapor and oxygen directly deposited onto the substrate to form ZnO crystal.[102]

Nucleation density of ZnO is determined by the activation energy and temperature as,[103]

$$N = A \exp(-G / RT) \qquad (3.3)$$

where N is the nucleation density, T is growth temperature, $G = G_V + G_S$ is activation energy of nucleation. G_V is volume free energy, which is related to the oxygen concentration as: $G_V \propto -\ln P(O_2)$. G_S is the surface free energy. Catalytic particles are introduced to change the local curvature on an otherwise flat surface, thus effectively lowering the surface free energy and total activation energy over those locations. On the

other hand, the relatively low oxygen concentration in the reactor tube makes G_V the volume free energy fairly large. Due to the lattice mismatch between ZnO and Si (100), island growth is still possible even without catalytic particles but the density of the nuclei, and thus the density of the nanostructures, will be lower under the same growth condition. It was observed that nucleation became much easier if Si (111) was used as the substrate, and very high density of ZnO nanostructures were deposited on Si (111) without the help of catalyst particles. It was interesting that the morphology of the nanostructures deposited on Si (111) was drastically different from those deposited on Si (100), despite the fact that identical growth parameters were adopted in both cases.

A major drawback of the thermal CVD system discussed above (hereafter called the oxygen-deficient growth system) is the lack of an independent control of the oxygen source. The growth environment presented in such a system is almost always oxygen deficient unless very small amount of zinc is used during the growth. Indeed, it is usually found that a large portion of the zinc power placed in the alumina boat is left un-reacted due to the limited supply of oxygen. Therefore, the yield of this growth system is determined by the amount of residual oxygen in the reactor tube (which is very hard to control) rather than by the amount of zinc powder.

To increase the product yield, and more importantly to reduce the oxygen-deficiency related defects in the as-grown samples, a separate oxygen gas source was added to the original growth system. Figure 3.3 shows the schematic diagram for the updated thermal CVD reactor (schematic diagram contributed by Mr. An-jen Chen). A thermocouple is located close to the inner quartz tube in order to precisely measure the reaction temperature. The pressure in the quartz tube can be controlled by a manual

throttle valve or an automated exhaust valve controller, which is connected to a mechanical pump and a manometer pressure gauge. Argon (carrier gas) and O_2 (reactant gas) are introduced into the tube precisely by using mass flow controllers to control the amount of flow rate. A photograph of the updated thermal CVD system is shown in Figure 3.4.

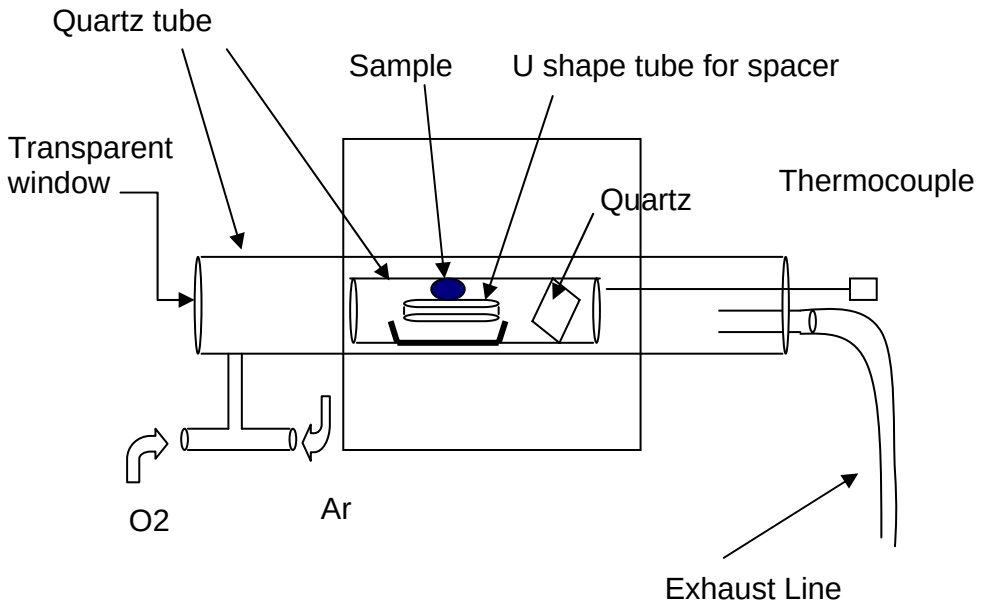

Figure 3.3: Schematic diagram of the updated thermal CVD growth system. [104]

Prior to the deposition of ZnO nanostructures using the updated system, the reactor tube was pumped down to a low vacuum (20 mTorr), and then purged with Argon gas. The sample was heated up to the growth temperature at a rate of ~30^{o}C per min. When the growth temperature was reached, oxygen gas was administered at a flow rate of 15-100 sccm. The growth temperature was maintained at 550-725^{o}C for about 30 min. Argon gas was kept flowing (flow rate: 100-1500 sccm) during the entire growth process

till the temperature has dropped back to room temperate. The gas pressure inside the tube was regulated at ~100 Torr during growth.

The local pressure of zinc vapor on the substrates is a key factor in the thermal CVD process. A quartz plate was placed in front of the boat as a baffle to reduce the speed of the carrier and reactant gas flow (Figure 3.3). To better confine the zinc vapor around the substrate, the substrate and boat were placed inside a short quartz tube (20 cm long) with a smaller diameter (2 cm) than that of the main reactor tube (5 cm in diameter). A spacer was placed in between the substrate and boat to optimize their distance.

It should be pointed out that the deposition of ZnO may take place along the entire length of the reactor tube, and white fluffy materials were often found on the tube wall after deposition. One added benefit provided by using the extra small reactor tube is that it can be easily replaced or removed from the thermal CVD system for cleaning, without breaking the vacuum sealing at both ends of the main reactor tube.

Figure 3.4: The updated thermal CVD growth system.

The precise timing and control of oxygen gas flow is critical for the success of the ZnO depositions. If oxygen gas is allowed to enter the reaction tube too early and zinc vapor has not sufficiently formed on the substrate, oxygen gas simply reacts with the zinc powder and the growth process terminates prematurely. This being the case, very little ZnO can be deposited on the substrate (Figure 3.5 c). Instead, dark-grey colored powder and small chips of oxidized zinc are formed on top of the zinc powders placed in the boat, while zinc powder at the bottom of the boat remains largely un-reacted. On the other hand, if oxygen gas is introduced into the tube too late, the zinc source is prematurely

exhausted by the residual oxygen or carried away out of the tube. In this case, the growth process is just similar to that resulting in the oxygen-deficient growth system. In order to obtain well-formed nanostructures, it is important that a small oxygen gas flow rate is used at the initial stage of the growth and the oxygen concentration is kept low in the reactor tube at all time. A surge in oxygen concentration usually leads to the overgrowth of the nanostructures into microstructures or the formation of ZnO polycrystalline films; it also reduces the volatility of the zinc source thus making the deposition on substrates more difficult.

The as-deposited samples consist of gray-white wax-like coatings on substrates (Figure 3.5 b). Thick and dense depositions tend to result in whiter coloration than thin and sparse depositions. Both sides of the Si wafer were often coated with ZnO. Under visual inspection, patches with uniform coloration and texture can be seen for coatings deposited on the upper surface of the substrate, the size of those patched varies from several millimeters to a few centimeters. The coatings deposited on the lower surface of the substrates appeared less uniform than those deposited on the upper surface. They were also less controllable and could have changed dramatically from one run to the other. Therefore, they were often discarded prior to further analysis.

Figure 3.5: (a) Si substrate on alumina boat before the thermal CVD growth, (b) after growth, (c) a typical example of under-deposited substrate; the growth was probably terminated prematurely (note that zinc left in the boat).

3.3 Morphology, size and crystallization

The as-grown samples were analyzed by scanning electron microscopy (SEM, Zeiss). Figure 3.6 shows some typical ZnO nanostructures synthesized by the oxygen-deficient thermal CVD growth system (SEM images contributed by Ms. Heewon Seo).

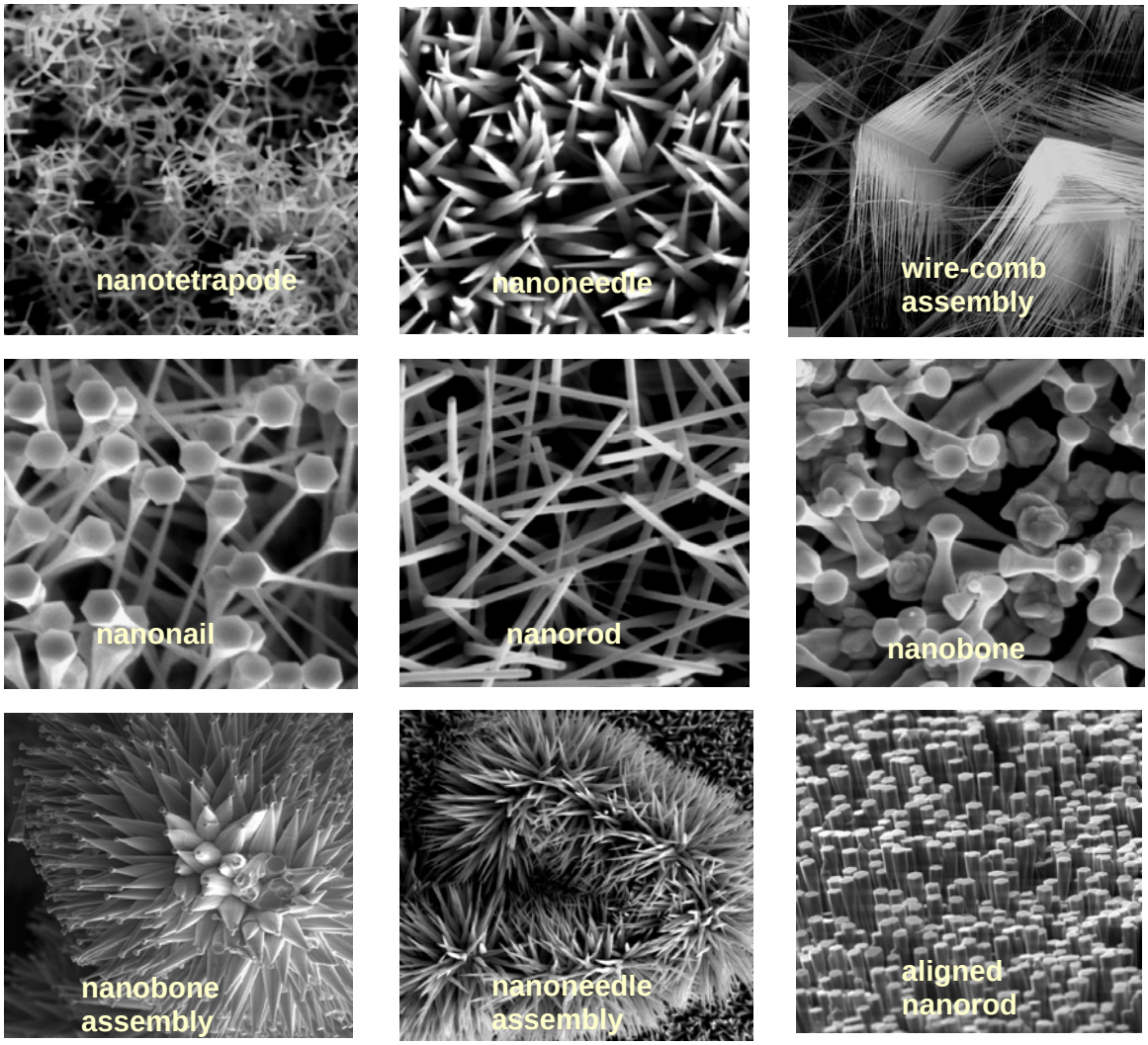

Figure 3.6: SEM images of some ZnO nanostructures synthesized by the oxygen-deficient thermal CVD growth method. All nanostructures were deposited on Si (100) substrate.

The size and morphology of the ZnO nanostructures can exhibit large variations depending on the different combinations of growth parameter as well as the catalysis used. Many factors can affect the size and morphology of the nanostructures. There are several controllable or semi-controllable parameters such as growth temperature,

temperature rate (ramping rate and cooling rate), vapor pressure (environment pressure and substrate (local) pressure), carrier gas (gas species and its flow rate), evaporation and deposition time period, oxygen flow rate and concentration, the total gas pressure in the reactor, and the characteristics of the substrate.

The following are factors which are uncontrollable but also affect the growth product profoundly such as the gas flow turbulence formed inside reactor, the formation of oxidized layer on the surface of zinc powder etc. Most of these are direct results of the inherent shortcomings of the thermal CVD deposition method. Therefore, it was often found that several different morphologies may be present on the same substrate, and different nanostructures were synthesized even if the same set of growth parameters were employed. Based on this consideration, it seems difficult to attribute any particular morphology and size to one set of several growth parameters. However, the formation of different morphologies and sizes were not completely random. Although several different morphology and size can be found simultaneously, there were always some types of morphology that were more common than others. The advent of the prevalent morphologies was associated with the growth parameters employed, when the growth parameters were changed the major features of the nanostructure changed accordingly. Although variations in shape and size existed when the same set of growth parameters were employed, the variations were small in terms of the averaged shape and size of the nanostructures, e.g. if in one growth most of the nanostructures are nanoneedles and nanorods with several tens of nanometers in diameters, in the next experiment using the same growth condition the major features will still be nanoneedles and nanorods with similar size although the quantity and distribution of each feature are usually different.

The controllability and repeatability of the shape and size of the nanostructures synthesized by the updated thermal CVD system are better than those synthesized by the oxygen-deficient growth system, due to its better control over the growth environment.

Despite the diverse morphologies presented in ZnO nanostructures, they all share a common feature: all morphologies display certain degree of axial symmetry (Figure 3.7). The symmetry axis is the c-axis of ZnO crystal, since this is the preferred growth direction. The shape of the nanostructures is determined by the growth rate in the c-plane with respect to that along the c-axis at different growth stages. A uniform growth rate over the entire formation period will result in a rod-like structure with uniform cross-section. The diameter and the aspect ratio of the rod primarily depend on the size of the catalyst alloy droplet (in the VLS process), and the relative growth rate perpendicular and parallel the c-axis respectively.

More complicated morphologies such tripods, tetrapods, comb-like structures and irregular branching structures can be broken down into smaller simpler constituent structures. ZnO nanostructures such as the nanoring, helical nanospring, nanobow etc. have been reported. [105, 106, 107] These nanostructures do not have a well-defined symmetry axis or have symmetry axis other than the c-axis of the crystal. Nevertheless, the c-axis is still the preferred growth direction for these nanostructures; their special shapes are formed by bending and twisting the c-axis so as to relieve the residual strain in the materials. No such structures were synthesized using our thermal CVD system.

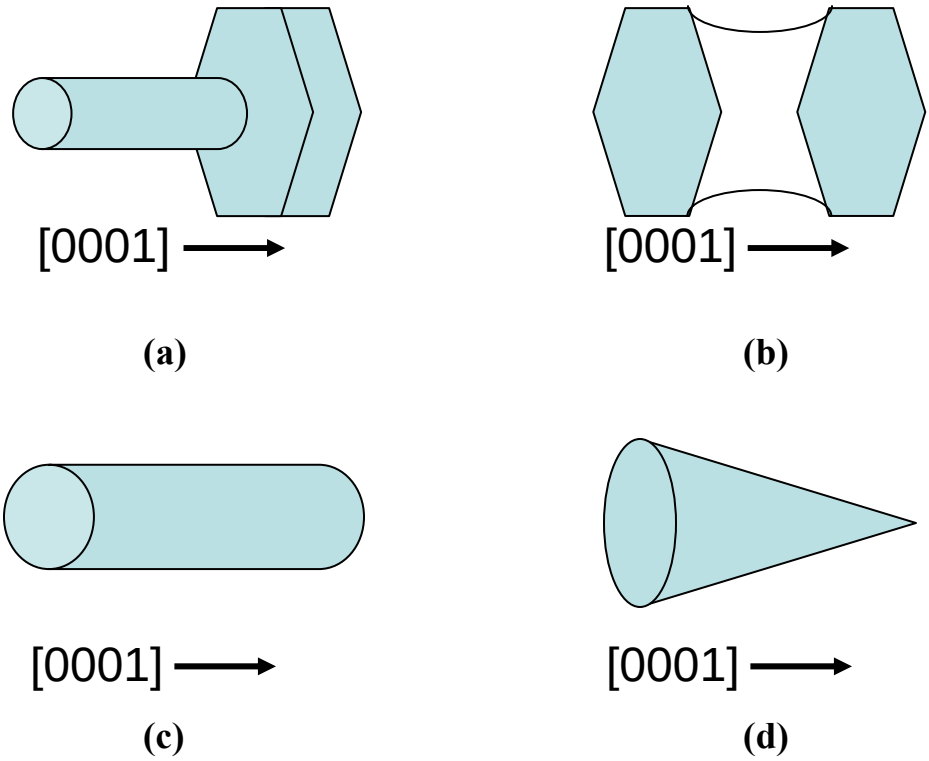

Figure 3.7: Schematic diagrams of several most common ZnO nanostructures synthesized by thermal CVD system: (a) nanonail, (b) nanobone, (c) nanorod, (d) nanoneedles.

Figure 3.8 shows a typical XRD pattern of the as-grown ZnO nanostructures. (XRD pattern collected by Mr. N. Sathitsuksanoh) Diffraction peaks from all major crystal planes can be found due to the random orientation of the nanostructures. ZnO nanostructures possess the same lattice constants and wurtzite crystal structure as the bulk ZnO crystals. The FWHM of all diffraction peaks are smaller than 0.2 ^{o}, indicating an excellent crystallization, in accord with the well known finding that each ZnO nanostructure is also a single monolithic ZnO crystal.

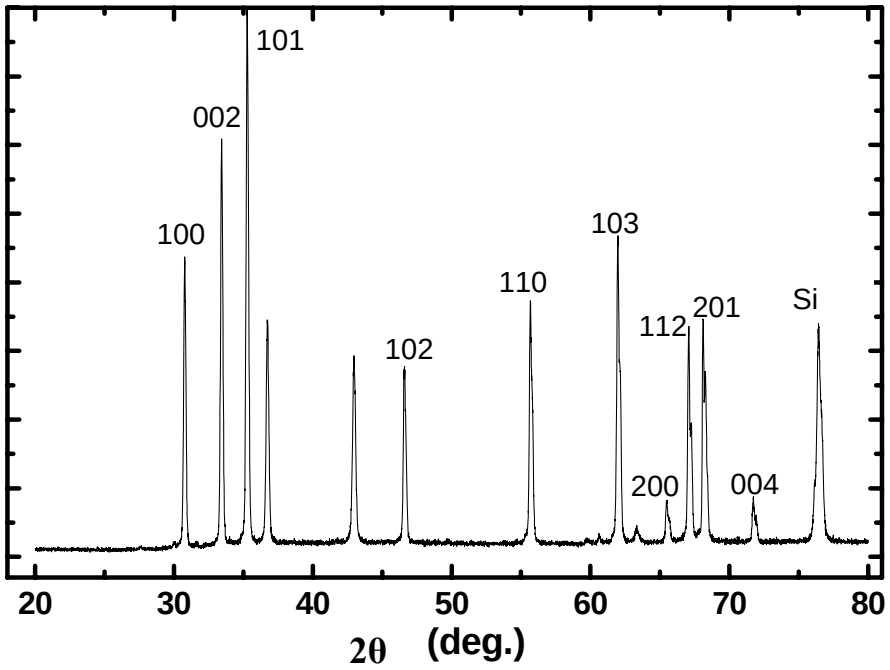

Figure 3.8: Typical XRD pattern of ZnO nanostructures.

3.4 Photoluminescence spectroscopy of ZnO nanostructures

Room temperature photoluminescence (PL) spectroscopy was performed using the 325 nm line (20 mW) and the 441.6 nm line (80 mW) from a He-Cd laser. PL spectra were collected using a spectrometer (JY-550) equipped with holographic gratings (2400 lines/mm, 3600 lines/mm), and a thermoelectrically-cooled charge coupled device (CCD) detector (2048 × 512 pixels). The spectral resolution of the system is ~ 0.01 nm, and the UV laser beam was focused onto a spot of ~10 μm in diameter on the sample surface using a ×27 lens (N.A.=0.4). The PL spectra collected should be regarded as the ensemble spectra of several tens to several hundred nanostructures.

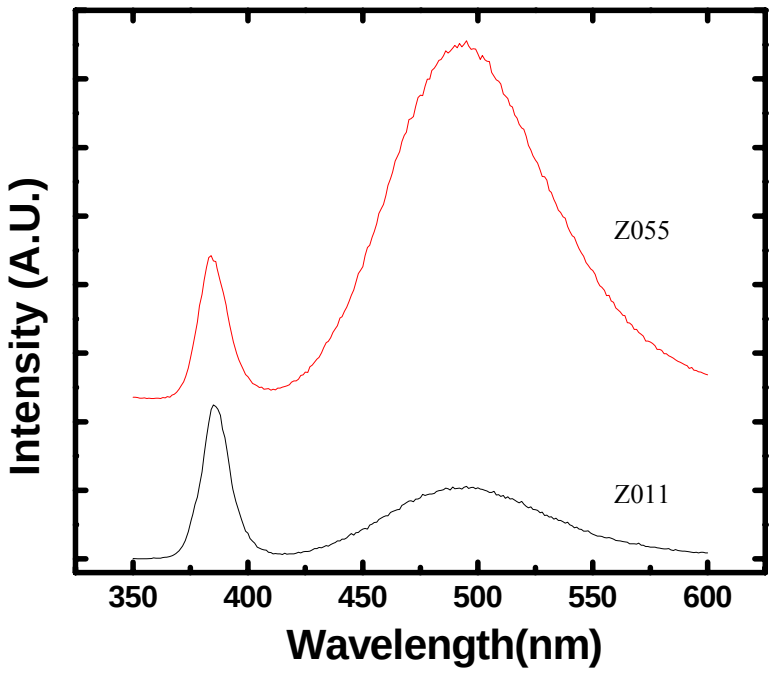

Figure 3.9: Room temperature PL spectra of ZnO nanorods collected from two different samples synthesized via the oxygen-deficient thermal CVD process.

The room temperature PL spectra of ZnO nanostructures synthesized by the oxygen-deficient thermal CVD procedure are shown in Figure 3.9. The two spectra were collected from two different samples (Sample #: Z011 and Z055) deposited using the same growth conditions. Both spectra exhibit a near-band-edge (NBE) emission peak at about 3.21 eV, and a broad blue-green visible emission band at about 2.48 eV. The NBE emission is mostly due to the excitonic transitions, while the blue-green emission is due to electronic transitions at defect states (the mechanism of this visible luminescence is discussed in details in Chapter 6). Broad emission bands may exist at the longer

wavelength side of the blue-green emission band, but their intensities are much weaker than that of the blue-green band. The FWHM of the NBE is about 0.1 eV. The peak of NBE is comprised of many emission lines together with their longitudinal-phonon replica, which cannot be resolved with room temperature PL measurements. At room temperature a strong exciton-LO phonon coupling leads to homogenous broadening and a fairly broad NBE peak. Therefore, the FWHM of the NBE peak bears little indications of the quality of the ZnO crystals. The quantum confinement effect was not considered because the sizes of the ZnO nanostructures studied in this work are much larger than the sizes needed for quantum confinement. Therefore, the inhomogeneous broadening in the luminescence bands due to the size variation in the nanostructures probed can be safely disregarded.

The major difference between the two spectra in Figure 3.9 is the relative intensity of the UV NBE emission peak to the blue-green band. It is interesting that the nanostructures deposited on both samples were nanorods with similar sizes and morphology. Clearly, there is no simple relationship between morphology and luminescence characteristics of ZnO nanostructures. It was often found that ZnO nanostructures with similar morphology and size possessed PL spectrum with quite different visible luminescence intensities, while similar PL spectra may come from different nanostructures. Nevertheless, the PL spectra colleted from different locations of the same sample were all similar to each other, indicating a good uniformity in terms of luminescence characteristics for samples prepared using this growth method.

It is well known that the luminescence of ZnO varies as a function of temperature. The PL spectra of ZnO nanostructures collected at various temperatures are shown in

Figure 3.10. The NBE emission peak redshifted as a result of the reduced band gap at elevated temperatures (Figure 3.11), and was also broader due to enhanced phonon scattering (Figure 3.11). The photon energy of the NBE as a function of temperature can be described by Varshini's empirical formula:

$$E_g(T) = E_o - \alpha T^2 / (T + \beta) \tag{3.4}$$

where E_o is the photon energy of the NBE emission at absolute zero. Equation 3.4 was used to fit the experiment data in Figure 3.11. The obtained α, β, and E_o are 1.5×10^{-3} eV/K, 244 K, and 3.38 eV, respectively. The obtained energy position at 0 K agrees well with the reported values for the energy position of the free exciton in ZnO.[108, 109]

Both the NBE and visible luminescence were being quenched with increasing temperature, but the intensity of visible luminescence decreased much faster. It was almost completely quenched at temperatures above 60°C (Figure 3.12). Interestingly, no shift was observed for the blue-green emission as the temperature increased, indicating that the defect levels involved in the blue-green luminescence are not associated with the band edges.[36] To the contrary, the electronic transitions associated with the NBE emission take place among effective-mass like states and band edges. Note that the thermal quenching behaviors of NBE and visible luminescence cannot be described by simple functional forms that containing a single exponential, such as:

$$I = I_0 \cdot [1 - \exp(-E_A / k_B T)] \tag{3.5}$$

where I_0 is the luminescence intensity at absolute zero, and E_A is corresponding thermal activation energy of the quenching mechanism.

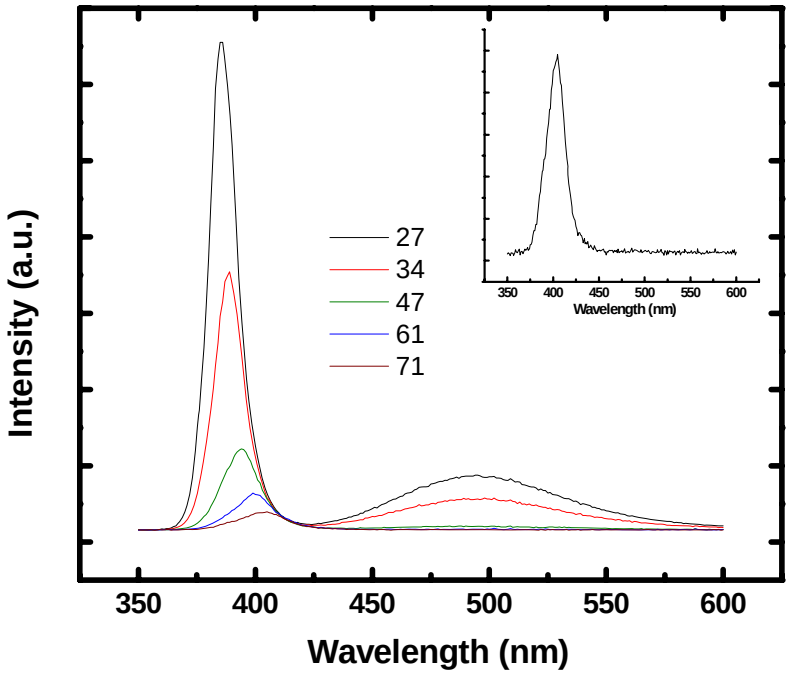

Figure 3.10: PL spectrums of ZnO nanostructures collected at different temperatures from 27°C to 71 °C. Inset shows the PL spectrum collected at 71 °C at a higher magnification.

Because of the small volume of the nanostructures and the lack of a heat sink near the nanostructures, the effective thermal conductivity of ZnO nanostructure ensembles was greatly reduced as compared to ZnO bulk materials. [110] The high power intensity of a focused laser beam and the strong absorption of UV laser light also elevate the local temperature of the illuminated nanostructure ensemble greatly. In view of the sensitivity of the PL event to temperature, caution must be exercised in conducting the experiment. In the present work, neutral density filters were progressively applied to reduce the power

of the incident light until no more change was observed in PL spectrum. Unless otherwise specified, this experimental protocol was employed for collecting all the PL spectra presented in this dissertation work.

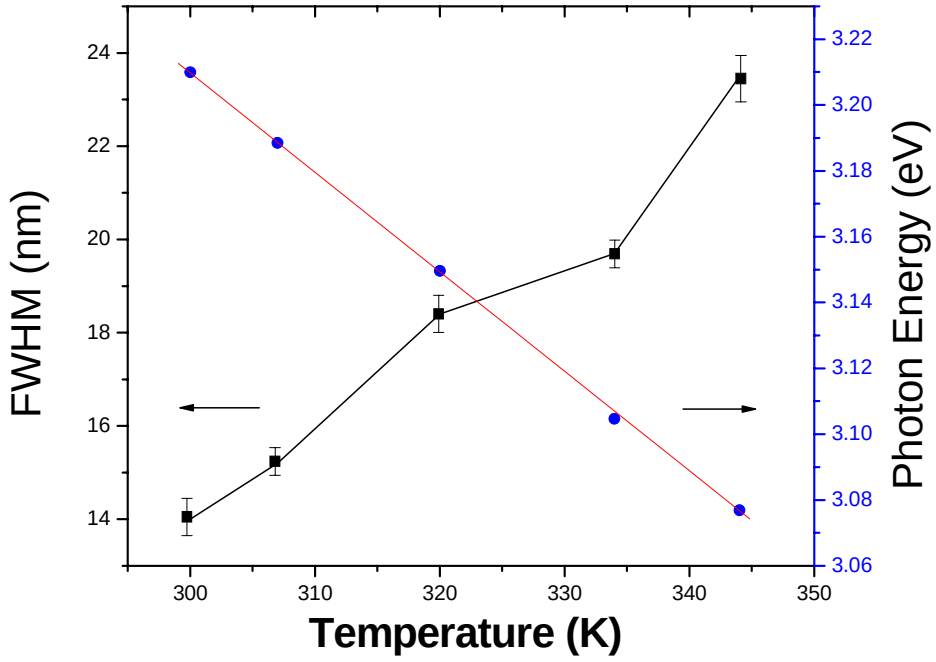

Figure 3.11: The FWHM and photon energy of NBE as a function of temperature. The red solid line is a fit according to Varshini's function.

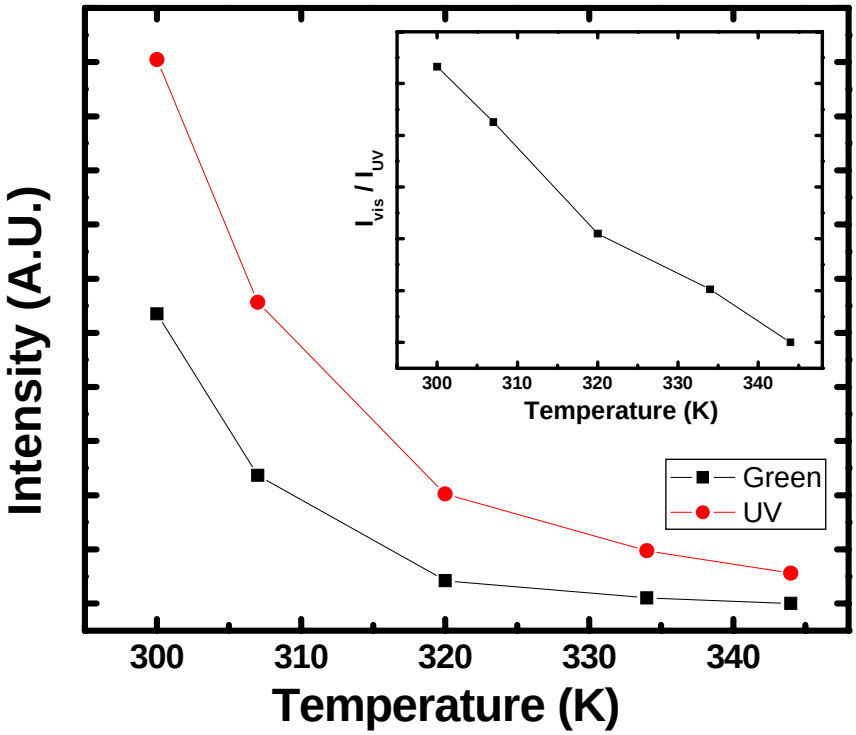

Figure 3.12: Intensity of NBE and visible emission as a function of temperature. The inset shows the change in the ratio of the intensity of NBE to visible emission with increasing temperatures.

The room temperature PL spectra of ZnO nanostructures synthesized by the updated thermal CVD method are shown in Figure 3.13 (b) and (c). Spectrum b and c were collected from different locations on the same sample (Sample #: Z0510). A typical PL spectrum of ZnO nanostructures synthesized *via* the oxygen-deficient thermal CVD system is also presented for comparison. All three spectra showed the ultra-violet near-band-edge (NBE) emission at about 3.21 eV. The visible emission from the sample

deposited via the oxygen-deficient CVD method was dominated by a broad blue-green emission band at about 2.48 eV. For a sample deposited by using the updated CVD system, the blue-green emission band at 2.48 eV was greatly reduced or completely disappeared. Spectrum c in Figure 3.13 shows a dramatically different PL spectrum: the blue-green band has given away to very strong violet-blue emission bands and broad bands in the yellow-orange-red range.

A common observation is that the blue-green emission was a result of an oxygen deficiency during the growth process, while the yellow-orange emission bands were observed in the PL spectrum collected from the samples grown with excess oxygen supply.[111, 112, 113] Therefore, it is expected that the blue-green emission band should dominate over other visible emission bands in the PL spectrum collected from samples synthesized by the oxygen-deficient CVD system (spectrum a in Figure 3.13). Indeed, the visible luminescence of those samples was always dominated by the blue-green luminescence. On the other hand, the PL spectrum of ZnO nanostructures synthesized in oxygen-rich condition (spectrum b and c in Figure 3.13) should display suppressed blue-green emission and enhanced yellow-orange emissions. When the balance between zinc and oxygen was reached and the defects due to the non-stoichiometry are minimized, the PL spectrum was essentially free of visible emission as shown in spectrum b of Figure 3.13.

The PL spectra of our ZnO samples are also in accord with the observation that the blue and the yellow-orange emission band always appear together, while the blue-green band is not related to the other emission bands.[2, 114]

As demonstrated in the PL spectra presented above, the PL characteristics of the ZnO samples deposited via the updated CVD system were much less uniform as compared with those of samples deposited using the oxygen-deficient CVD system. Quite different PL spectra were often found at locations in close proximity (< 0.5 mm apart), despite the fact that the morphology and size of the nanostructures are similar at these locations. We believe that the large variation in the PL characteristics is possibly related to the gas flow turbulence and vortex formed around the small quartz tube and the baffle, which causes large changes in local oxygen and zinc vapor concentrations.

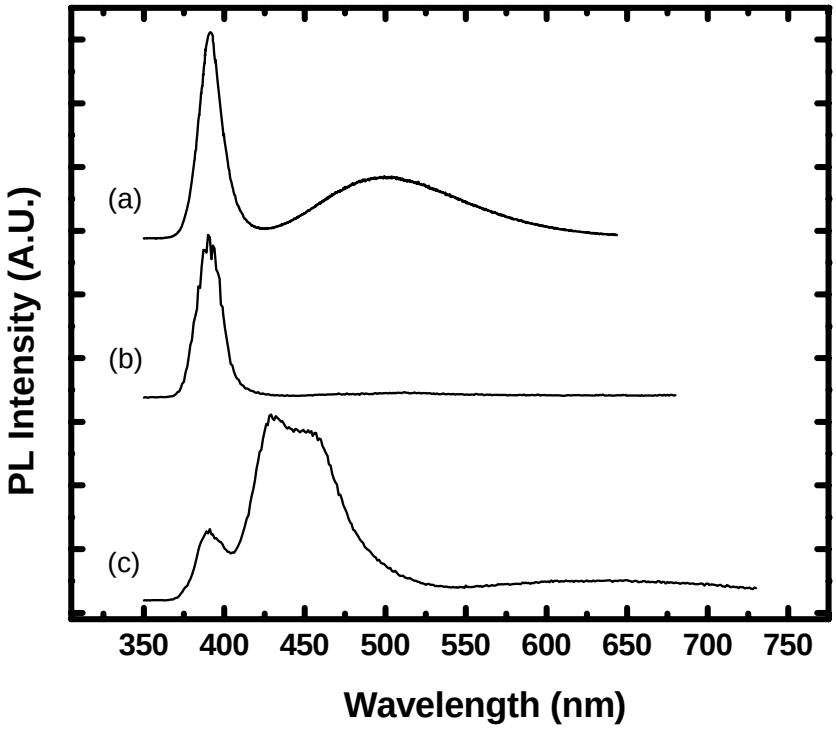

Figure 3.13: Room temperature PL spectra of ZnO samples deposited using the oxygen-deficient CVD procedure (a), and the updated CVD system [(b) and (c)]. Note that spectra (b) and (c) were collected from different locations on the same sample.

It has been shown that the intensity of the blue-green emission is strongly influenced by the surface condition of the ZnO nanostructures.[115, 116, 117] We have shown that through surface band bending, chemisorbed oxygen played a crucial role in the recombination process of the blue-green emission.[118] Equivalently important is the concentration and the spatial distribution of defect states, at which the recombination process of the blue-green emission takes place. It is believed that the recombination process occurs between the two defect-levels, and one of them involves interstitial zinc or its complex.[119, 120, 121] As the interstitial zinc and oxygen vacancies are most easily formed in oxygen-deficient growth conditions,[122] it is understood that the blue-green emission is dominant in samples deposited in an oxygen-deficient environment. On the other hand, the yellow-orange emission is believed to be related to interstitial oxygen or its complex.[3, 123]

Since the oxygen-rich growth environment will lead to a more pronounced surface adsorption of oxygen, one should expect a strongest blue-green emission in the sample grown using the highest flow-rate of oxygen, provided that the concentrations and distributions of the defect states of blue-green emission are similar among the three samples grown using different oxygen flow-rate. Therefore, the absence of the blue-green emission in the two samples grown with sufficient oxygen supply can be ascribed to the reduced concentration of defect states at which the blue-green emission takes place. The presence of other emission bands in the sample grown with high oxygen flow-rate can thus be explained as a result of the introduction of intrinsic defects such as interstitial oxygen and zinc vacancies.

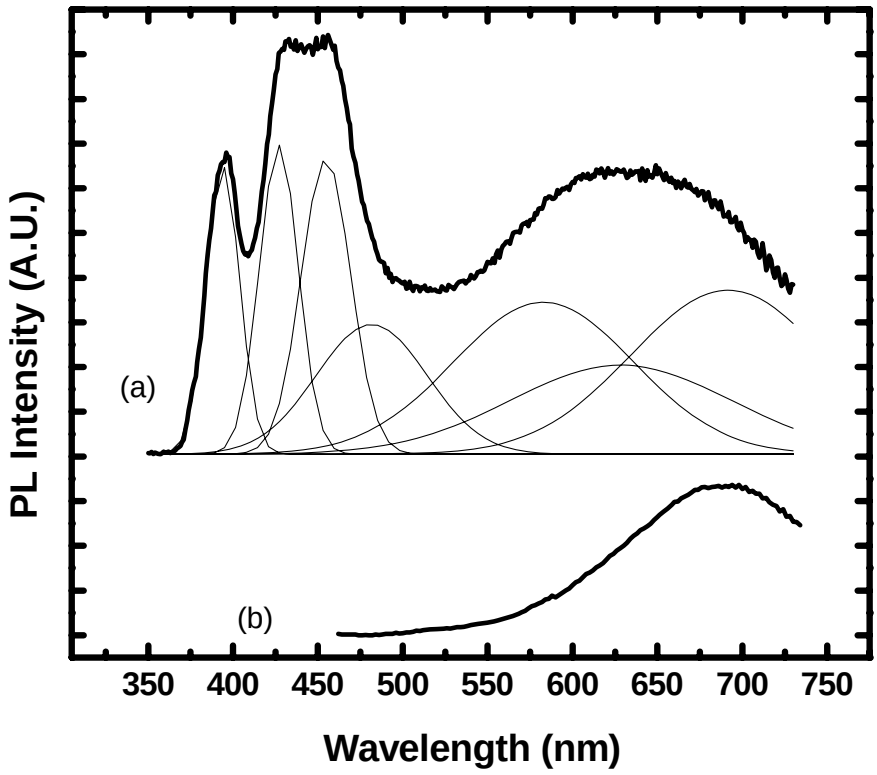

Figure 3.14: Room temperature PL spectrum of the sample deposited with a high oxygen flow-rate collected using 325 nm line (a) and 441.6 nm line (b) of He-Cd laser. The thin solid lines indicate emission bands derived from curve-fitting multiple Lorentzian functions to the PL spectrum.

In Figure 3.14 the PL spectrum of a sample deposited with a high oxygen flow-rate is fitted with seven Lorentzian peaks: ultra-violet (3.21 eV), violet (2.9 eV), blue (2.71 and 2.6 eV), green (2.19 eV), yellow (2 eV), and red (1.8 eV). The PL spectrum of the same sample collected using the 441.6 nm line of the He-Cd laser (Figure 3.14b) only shows the red emission band. On the contrary, no emission bands were observed for the

other two samples when the 441.6 nm line was used as excitation. The inability to generate the blue-green emission (~ 2.48 eV) using below-band-gap excitation,[124] lies in the recombination process which occurs between a shallow donor level and a deep defect level. Electron-hole pairs need to be generated by above-band-gap excitation first, and then the photo-generated electrons and holes can be trapped by shallow and deep level defect states, respectively.

The fact that the red emission can be generated by below-band-gap excitation implies that it does not depend on the photo-generation of both conduction electrons and holes. We speculate that the recombination process of red emission occurs between photo-generated holes bound at a deep-level state and conduction electrons or electrons bound at another deep-level state. Another scenario is that the red emission process may take place through the intra-defect transition between the ground state and the excited state of a defect level/defect complex (Frank-Condon principle). It has been reported that the green (2.19 eV) and yellow (2 eV) emission bands can be generated by photons with an energy higher than 3 eV,[125] thus they were not observed in the PL spectrum (Figure 3.14b) collected using 441.6 nm line as an excitation.

3.5 Raman spectroscopy of ZnO nanostructures

Room temperature Raman spectroscopy was performed using the 441.6 nm line from a He-Cd laser (80 mW). Raman spectra were collected using a spectrometer (JY-550) equipped with two 3-inch holographic gratings (2400 lines/mm, 3600 lines/mm), and a thermoelectrically-cooled charge coupled device (CCD) detector (2048 × 512 pixels). The laser beam was focused onto a spot with ~5 μm in diameter on the sample surface using a ×50 lens (N.A. = 0.45). The spectral resolution of the system is ~0.2 cm^{-1}. Micro-Raman spectroscopy was carried out using a backscattering geometry. The incident beam was linearly polarized, and the polarization states of the scattered beam were not analyzed. The entrance slit of the spectrometer was kept at 0.1 mm wide in order to minimize the artificial broadening of the Raman scattering peaks induced by the finite slit size.[126] Similar to PL spectroscopy, the Raman spectra collected should be regarded as the ensemble spectra of several tens to several hundreds nanostructures.

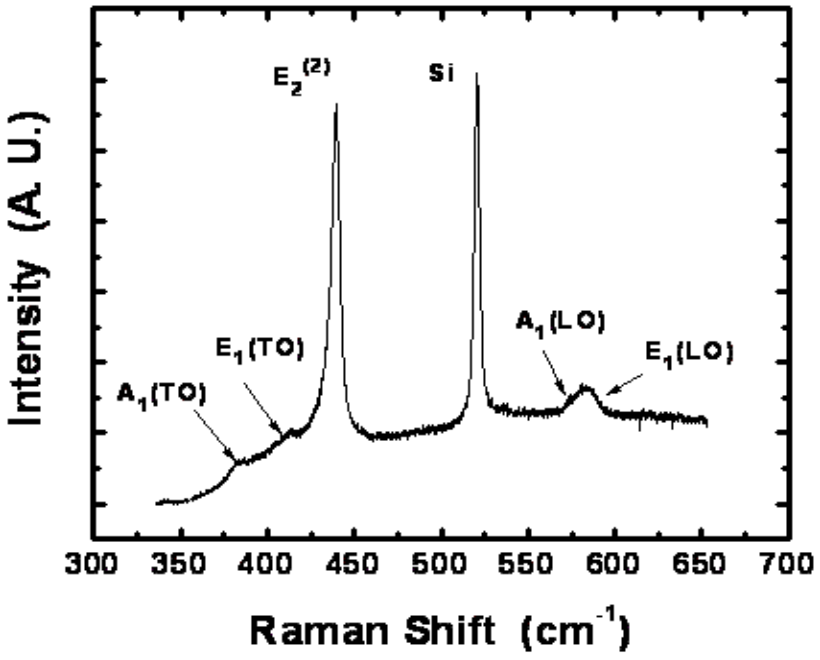

(a)

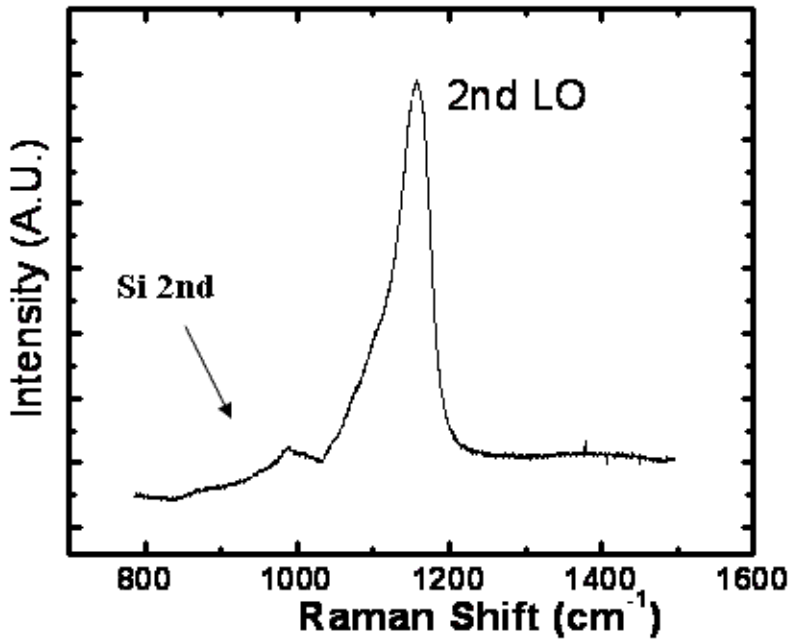

(b)

Figure 3.15: Room temperature Raman spectrum of ZnO nanorods. (a) low wavenumber region, (b) high wavenumber region.

Wurtzite GaN belongs to the C_{6v}^4 space group, and group theory predicts $A_1(z) + 2B_1 + E_1(x,y) + 2E_2$ optical modes at the Γ point of the Brillouin zone.[127] Among these optical modes, the two E_2 modes are Raman active, the A_1 and E_1 modes are both IR and Raman active, and the two B_1 modes are silent. Because of the polar nature of ZnO, the A_1 and E_1 modes are split into transverse (TO) and longitudinal (LO) components by the macroscopic electric field.

The same samples that were analyzed for PL measurements in the last section, the ZnO nanorods (Z011 and Z055) synthesized using the oxygen-deficient system and the nanostructures (Z0510) synthesized using the updated system, were studied in Raman scattering experiment. The room temperature Raman spectrum of ZnO nanorods is shown in Figure 3.15. The PL spectrum of ZnO nanorods is shown in Figure 3.9. Since the Raman spectra collected from the two nanorod samples were similar, only one spectrum is shown here. All Raman active modes were observed due to the random orientation of the nanorods. The overtone of the LO phonon mode is shown in Figure 3.15 b. The frequencies and FWHM of the Raman modes were obtained by fitting the spectrum with Lorentzian functions, the results are shown in Table 3.1.

Table 3.1: Frequencies and FWHM of the Raman modes of ZnO nanorods.

	Quasi-TO	E1(TO)	E2	Quasi-LO	LO overtone
Frequency (cm^{-1})	380.5	409.3	436.4[a]	583.3	1160
Linewidth (cm^{-1})	13.2	8.1	6.5	20.5	52

[a] corrected for temperature effect

In analogy to the PL spectroscopy results, quantum confinement of optical phonons was not considered because of the size of the ZnO nanostructures. Since the Raman spectra correspond to an ensemble spectrum of many nanostructures, the inhomogeneous broadening of the Raman scattering peaks due to the size variations of the nanostructures may play an important role.[128] Therefore, this broadening effect does not need to be considered in this work.

The linewidth of the Raman scattering peak is related to the lifetime of the correspondent phonon *via* the energy-time uncertainty relationship:[129]

$$\Delta E/\hbar = 1/\tau \qquad (3.6)$$

where ΔE is the linewidth of the phonon mode, τ is the lifetime of the mode, and ħ is the Planck constant. Using Equation 3.6 we obtained 0.82 ps and 0.65 ps for the phonon lifetime of the E_2 and E_1(TO) modes, respectively. The E_2 phonon lifetime for our samples is close to that of the ZnO bulk single crystals (0.87 ps, Table 3.2). Since the phonon lifetime is directly related to the quality of the crystal, it can be seen that our ZnO nanostructures are of high crystal quality.

The FWHM of the A_1(TO) (or more precisely quasi-TO) and quasi-LO phonon mode is significant larger than the linewidth of E_2 mode. The broadening in A_1(TO) mode is largely caused by mode mixing rather than different phonon lifetimes. Broadening of the LO phonon mode is caused by both mode mixing and plasmon-LO phonon coupling effect. It is well known that when the direction of phonon propagation is between the c-axis and the c-plane, a mixing of A_1 and E_1 modes will occur in wurtzite crystals where long-range electrostatic forces dominate over the anisotropic short-range force.[130, 131] As a result of mode mixing, the quasi-LO mode (QLO) exhibits a frequency

in between those of the E_1(LO) and A_1(LO) modes, and quasi-TO (QTO) mode adopt a frequency in between E_1(TO) and A_1(TO) modes, while E_1(TO) remains unaffected.[49, 50, 132, 133] The frequencies of QLO and QTO modes are described by the following equations:

$$\omega_{QLO}^2 = \omega_{E_1(LO)}^2 \sin^2\theta + \omega_{A_1(LO)}^2 \cos^2\theta \qquad (3.7)$$

$$\omega_{QTO}^2 = \omega_{E_1(TO)}^2 \cos^2\theta + \omega_{A_1(TO)}^2 \sin^2\theta \qquad (3.8)$$

where θ is the angle between the c-axis and the direction of phonon propagation. A larger angle θ will cause the quasi-TO and quasi-LO modes to up-shift more towards the E_1(TO) and E_1(LO) modes. Assuming that the nanorods are randomly orientated, the c-axis of the rods may take any angle between 0 and 90°, resulting in mode mixing.

The Raman spectrum (Figure 3.16) of an undoped ZnO bulk crystal (Eagle Picher, Inc.) was collected for the purpose of comparison and reference. Two spectra were collected: one from the c-plane and the other one from the a-plane of the crystal. Both the spectra were collected in back-scattering geometry, thus the scattering geometry is Z(-,-)$\underline{Z}$ and X(-,-)$\underline{X}$ for the c-plane and a-plane scattering respectively. According to the selection rule, E_2 and A_1(LO) modes are allowed modes in the Z(-,-)$\underline{Z}$ scattering geometry, while A_1(TO), E_1(TO) and E_2 modes are the allowed modes in the X(-,-)$\underline{X}$ scattering geometry. No mode mixing should be observed in both cases, provided that the scattering geometries are strictly followed. The appearance of a longitudinal acoustic (LA) overtone and a quasi-LO mode is probably due to the miscut of the ZnO wafer. The frequencies and linewidth of the Raman modes were obtained by fitting the spectrums with Lorentzian functions, and the results were shown in Table 3.2.

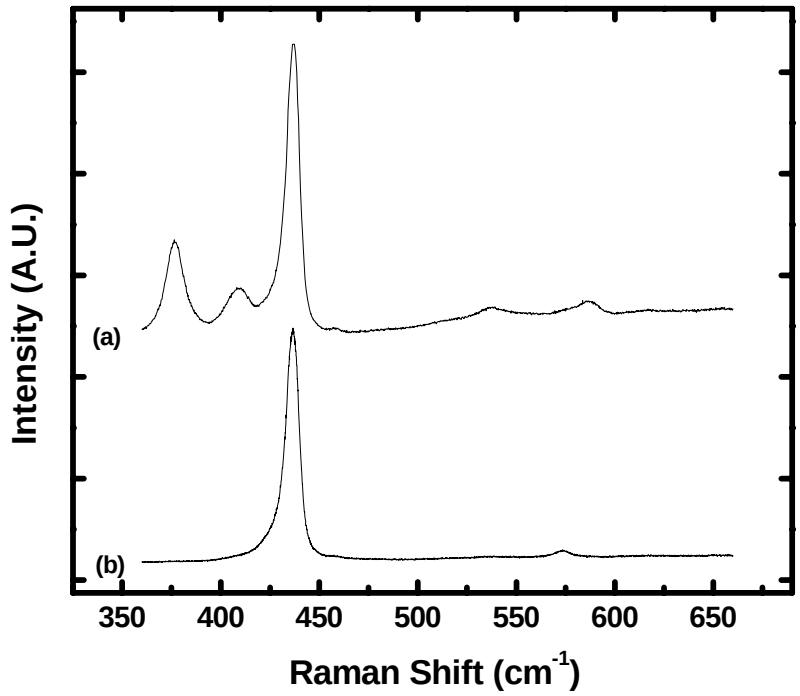

Figure 3.16: Room temperature Raman spectra collected from the a-plane (a) and the c-plane (b) of a bulk ZnO crystal using back-scattering geometry.

Table 3.2: Frequencies and FWHM of the Raman modes of a ZnO bulk crystal.

	A_1(TO)	E_1(TO)	E_2	LA overtone	A_1(LO)
Frequency (cm^{-1})	376.8	409.5	436.5	540	573.5
Linewidth (cm^{-1})	9.6	11.4	6.1	30	9.8

	Quasi-LO	E_1(LO) [a]
Frequency (cm^{-1})	585.9	591
Linewidth (cm^{-1})	15.2	11

[a] E_1(LO) mode was obtained by using a 90° scattering geometry.

The frequencies of the $E_1(TO)$ and E_2 modes of the ZnO nanorods are very close to those of the bulk crystal. It is well known that the frequency of E_2 mode is affected by the biaxial stress in c-plane of the wurtzite crystal. Therefore, the biaxial stress, which is the averaged stress over the entire length of the nanorod, was mostly released, assuming that the undoped bulk crystal is stress-free. Giving the frequencies of quasi-TO, $A_1(TO)$ and $E_1(TO)$ listed in Table 3.1 and 3.2, Equation 3.7 gives an effective angle θ of 71^o for the nanorods ensemble. Note that the effective angle only gives a rough estimation of the overall orientation of the nanorod ensemble. The overall broadening in the ensemble spectrum depends on the homogenous broadening of the quasi-TO mode from an individual nanorod and the inhomogeneous broadening due to the different orientations in different nanorods. The analysis of the quasi-LO mode is further complicated by the effect of plasmon-LO phonon coupling. Unless the charge concentration of the nanorods is very low, the angle θ or the frequency of the quasi-LO mode can not be estimated from Equation 3.8. A detailed description of plasmon-LO phonon coupling will be given in Chapter 6.

Thermal effects, which lead to the peak shift and broadening in Raman spectrum, can not be ignored for the same reasons mentioned in the last section. However, the problem is less severe in Raman experiments using a visible laser source, due to the much weaker absorption of visible light by ZnO. The same experimental protocol can be applied to reduce the thermal effect: the laser power can be progressively reduced till no change can be observed in the spectrum. Unfortunately, because of the inherently weak Raman signal, the incident laser light has to be very intense in order to have sufficient signal to noise ratio. With a reduced laser excitation, usually only the E_2 mode was still

detectable. In this way, the temperature induced peak shift of the E_2 mode can be readily obtained. The technique for the correction of the temperature effect in all Raman modes is described in Chapter 6.

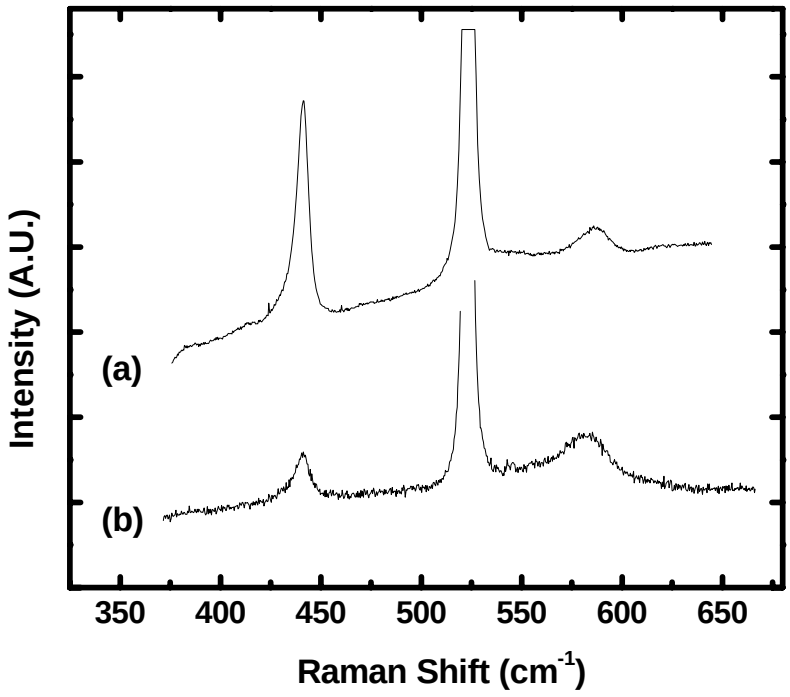

Figure 3.17: Raman spectra collected from two locations on the same sample (Z05100) synthesized using the updated growth system.

Similar to the PL spectra, the Raman spectra collected from different locations of the same sample were fairly uniform, provided that the sample was synthesized using the oxygen-deficient system. The opposite was true for samples synthesized using the updated growth system. Figure 3.17 shows two Raman spectra collected from different locations of the sample of Z0510 (synthesized using the updated system). The major

difference between the two spectra is the relative intensity between E_2 and quasi-LO phonon mode. The observed enhancement of the LO phonon mode can be ascribed either as due to the electronic energy levels in the band-gap (resonant Raman scattering), or to the band bending near the surface (electric field induced effect).[134, 135]

Given that the LO phonon mode scattering was due to the electric field induced effect, the LO phonon to E_2 phonon scattering intensity ratio was determined by the strength of the electric field in the depletion layers, and by the surface to volume ratio of the nanostructures. Although Raman scattering took place over the entire volume of the nanostructures, only a fraction of the total scattering volume was affected by the electric field. Since the morphology and size of the nanostructures at two locations were all similar, the ratio of the field-affected scattering volume to the total scattering volume was also similar. In addition, the two locations were in close proximity on the same sample, and they had been exposed to identical process/storage conditions, thus oxygen adsorption on the surfaces of the nanostructures should be similar. Since band bending is determined by the extent of oxygen adsorption, it is reasonable to assume that there was no big difference in the electric field among the nanostructures on the same sample. In view of these facts, the extent of the electric field effect should also be similar for the nanostructures at two locations.

It can be concluded that the large difference in the intensity of LO phonon scattering was most likely caused by the difference in the concentration of the energy levels formed in the band gap. These energy levels, in all probability, were formed by native defects created in crystal during growth. These defects may play roles in the visible luminescence processes as well. Although the same defect states may participate

in both Raman scattering and visible luminescence processes, no simple correlations between the characteristics of Raman and PL spectrums could be found; nor are there any simple correlations between the characteristics of Raman spectrum and the morphology of the nanostructures on this sample. Nevertheless, it was always found that if Raman spectra display a large variation at different locations on a certain sample, the PL spectrum will also display a large variation at those locations. In other words, any statement regarding the uniformity of the optical properties of certain sample is applicable to both Raman and PL spectra.

3.6 Conclusions

In summary, ZnO nanostructures were synthesized by using two different thermal CVD growth procedures: oxygen-deficient and oxygen-rich growth conditions. The as-grown nanostructures were of high crystal quality as confirmed by XRD and Raman measurements. SEM images revealed a wide array of morphologies and sizes in the ZnO nanostructures. It was often found that nanostructures with different morphology and size were able to coexist on the same sample. Some correlations can be found between the predominant morphology of a sample and the growth conditions employed to synthesize it, although no general conclusion can be drawn regarding the correlation between the morphology and the growth parameters. Better controllability for morphology and size can be achieved by using the up-dated thermal CVD system. The visible luminescence of ZnO nanostructures synthesized by the two different growth systems was markedly different due to the different native defects introduced under oxygen-deficient and oxygen-rich growth environments. The visible luminescence of the nanostructures

synthesized in an oxygen-deficient environment was dominated by the blue-green band, while the oxygen-rich nanostructures contained various emission bands other than the blue-green band. ZnO nanostructures were found to be mostly stress-free in Raman experiments. Various broadening and enhancement effects in different Raman modes were discussed. No general correlations could be found between morphologies and luminescence/Raman characteristics of the nanostructures. Samples synthesized with the up-dated growth system demonstrated less uniformed optical properties that those synthesized using the oxygen-deficient growth method.

CHAPTER 4

LASING IN WHISPERING-GALLERY-MODE IN ZINC OXIDE NANONAILS

4.1 Introduction

ZnO is a promising candidate for developing high-efficiency room temperature ultraviolet laser devices. Optically pumped room temperature lasing in ZnO thin films has been demonstrated.[136] Recent progress in the fabrication of nanostructured semiconductor materials has created new opportunities for developing submicron-sized or even nano-sized optoelectronic devices. Recently, optically pumped room temperature stimulated emission and lasing have been reported in many ZnO nanostructures where ZnO serves as both the active (gain) material and optical cavity. In the lasing actions reported, most of the cavities formed by ZnO nanostructures exhibit a Fabry-Perot (F-P) type of resonance in which the top and bottom facets of the nanostructure serve as two reflecting mirrors while the sidewall of the structure provides lateral confinement.[137, 138, 139, 140] On the other hand, random lasing is also observed in samples with a high density of nanowires.[141, 142]

The cavity formed by the two end facets of ZnO nanowires cannot provide a high level of confinement due to the limited reflectivity at the end facets for normal incident light, and the high diffraction loss when the lateral size of the cavity is much smaller than

the wavelength. This results in a relatively low quality factor (Q factor).[143] It has been shown that whispering gallery modes (WGM) possess a very high Q factor, where light is confined on the circumference of a dielectric disk or sphere.[144, 145] Lasing in WGM has been observed in both a GaN Microdisk,[146] and a hybrid ZnO/SiO_2 microdisk.[147] Very recently, the presence of WGM has been demonstrated in tapered ZnO nanoneedles with hexagonal cross section and a lateral size even smaller than the wavelength.[148] However, the spectra only show broad emission bands in the visible spectral range without signs of high Q factor cavities, and no lasing action was reported.

In this work, we have demonstrated ultraviolet lasing in WGM using ZnO nanonails synthesized by thermal chemical vapor deposition (CVD). Very sharp emission peaks [full width at half maximum (FWHM) = 0.08 nm] were observed in the spectrum of a single nanonail, indicating a high Q factor of the cavity formed by the hexagonally shaped nanonails.

4.2 Experiment

ZnO nanonails were grown on a Si substrate using thermal CVD. Detailed information about the growth process can be found elsewhere.[149] The morphology of the as-grown samples was analyzed by scanning electron microscopy (SEM, using a DSM 940 instrument). The 337 nm line of a pulsed nitrogen laser (Spectra-Physics, VSL-337ND-S, pulse width ~ 4 ns) was used for excitation. A Jobin-Yvon's spectrometer with a thermoelectrically-cooled charge coupled device (CCD) detector was used to collect the spectrum. The spectral resolution of the spectrometer is 0.0125 nm when a 2400 G/mm grating is used with a spectrometer entrance slit width of 0.01 mm.

4.3 Result and Discussion

Figure 4.1 shows the SEM micrographs of the nanonail (SEM image contributed by Ms. Heewon Seo). The hexagonal symmetry of the sample can be clearly demonstrated by inspection of the head of the nanonail. This shape suggests that the direction of the wire is along the c axis. A nanonail is composed of a shaft (or pin) of several micrometer long, and a hexagonal shaped head with a few hundreds of nanometers in diameter. The head of the nanonail possesses well defined symmetry and very smooth edge facets which are necessities for the realization of stimulated gain and lasing.

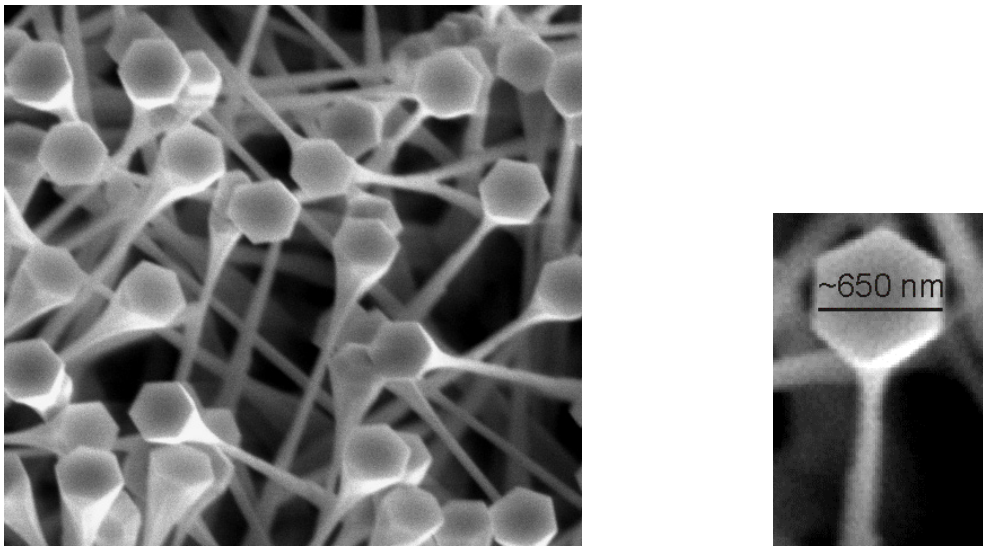

(a) **(b)**

Figure 4.1: (a) SEM image of ZnO nanonails grown using Au catalytic particles. (image size; 6 μm by 6 μm). (b) Expanded view of a single nanonail.

The ZnO nanonail sample was pumped by a pulsed UV laser positioning the beam normal to the sample surface. The laser light was focused to a spot of about 10 μm in diameter on the sample through a microscope objective. Near-band-edge emission signals of the ZnO nanonails were then collected with an optical fiber (N.A. = 0.22) placed at 45^{o} relative to the incident laser beam and at a distance of about 0.5 cm from the sample. At this distance, the acceptance angle of the optical fiber is ~11^{o}, which is limited by its core diameter (1 mm). The polarization of the emitted light was not analyzed.

Figure 4.2 shows the emission spectra under different excitation laser intensities. When the pump power density is lower than ~17 MWcm^{-2}, the spectra display only a broad spontaneous emission band with a FWHM of about 11 nm. Once the power density exceeds the threshold level of ~17 MWcm^{-2}, very sharp peaks with FWHM < 0.2 nm begin to show up on the top of the broad spontaneous emission band. As the pump intensity increases, the gain becomes large enough to enable cavity modes with higher loss to start lasing, while the intensity of spontaneous emission also increases. When the pump intensity reaches 22.4 MWcm^{-2}, there are already a total of 12 modes lasing. Further increases in intensity do not yield anymore new lasing modes, but only serve to broaden the peaks. The emission intensities were integrated over the spectral range and plotted against the pump intensity (see inset of Figure. 4.2), where the transition from spontaneous emission to lasing at ~17 MWcm^{-2} can be clearly seen.

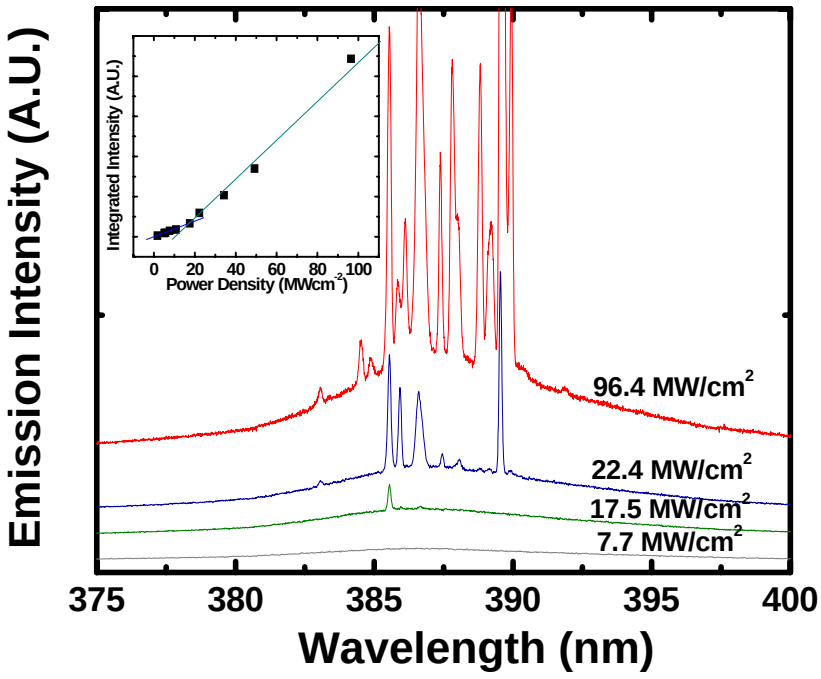

Figure 4.2: ZnO nanonail emission spectra at various pump intensities; 7.7, 17.5, 22.4 and 96.4 MW/cm^2 from the bottom to the top. The inset shows the integrated spectral emission intensity at various pump intensities. (The threshold pump intensity of ~17 MWcm^{-2} is at the crossing of the two dashed lines for spontaneous and stimulated emission.)

The three major mechanisms that provide resonant cavity and optical feedback for lasing in semiconductor nanostructures are the following. (1) Fabry-Pérot (FP) type resonant cavity is formed by the two end facets of the nanowire or nanopillar. (2) Closed-loop path is formed by the coherent multiple scatterings between neighboring nanowires,

which is referred to as random lasing. (3) Photons are confined by the total internal reflection at the ZnO-air boundary, where lasing occurs in WGMs.

The nanowires or nanoribbons in which F-P type of lasing is observed usually have relatively large end facets.[2, 3, 4] For nanowires with diameters < 100 nm the optical confinement is inefficient due to the large diffraction loss.[4] The special geometry along with the small size of the shaft part of the nanonail (Fig. 1) makes the F-P type lasing along the shaft (or pin) of our nanonail an unlikely candidate. Furthermore, the emission spectrum does not demonstrate the periodic spacing of emission peaks which can be theoretically expected in this type of F-P cavity.

Random lasing can also cause a super-narrow irregular emission peak.[6, 7] The essential characteristic of random lasing is the critical dependence on the excitation area; *i.e.*, the excitation area needs to be large enough so that a closed-loop with sufficient gain can be formed inside the area illuminated. The random lasing theory has shown that a linear relationship exists between $A^{2/3}$ and P_{th}^{-1}, where A is the threshold excitation area and P_{th} is threshold pump intensity.[6] Random lasing also demands that the particle size of the optical medium and the mean free path of the scattering to be much smaller than the wavelength of the laser emission. This is one of the reasons that random lasing is usually observed in nano-crystallized materials.

To verify the effect of the excitation area on the lasing threshold, an aperture was used to reduce the incident laser beam size. In Figure 4.3, three emission spectra were collected from the same location on the sample by using the same pump intensity but different excitation areas. The spectrum at the bottom of Figure 4.3 was collected by using an excitation area of 2 μm^2, where only a single emission peak can be seen at 388.8

nm in the spectrum. When the excitation area is increased to 6 μm^2, an additional small peak at 385.9 nm also begins to show up in the spectrum. Finally, two more peaks showed up in the spectrum at the top when the excitation area is increased to 11 μm^2. The increasing number of emission peaks as the excitation area is enlarged can be easily explained by the fact that more nanonails are illuminated by a pump laser as excitation area grows. When the excitation area is reduced to 2 μm^2, only a single nanonail can be completely covered by the pump laser spot, which is due to the average size of the nanonails and their density of distribution. What is different from random lasing is that the pump threshold is not affected by the change of the excitation area in spite of the increasing number of peaks. In all three spectra, the sample was pumped slightly over the threshold pump intensity 17 $MWcm^{-2}$, and all the sharp emission peaks disappeared when pump intensity was below the threshold level. Because the threshold of random lasing depends on the excitation area and large numbers of nanowires or powders are needed to form a resonant cavity in random lasing, we believe that the common threshold for all three different excitation areas and the fact that only a few nanonails are left within the reduced excitation area excludes the possibility of random lasing.

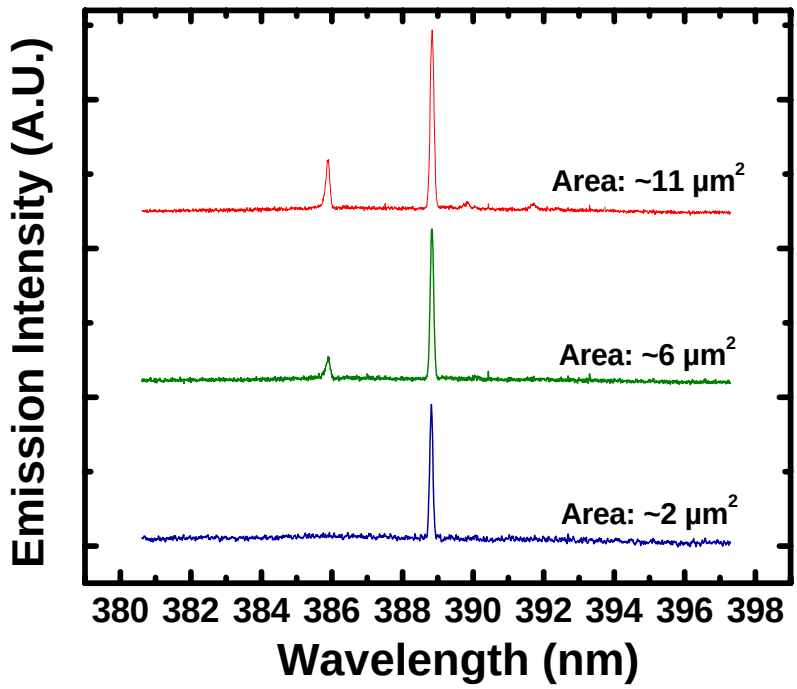

Figure 4.3: Emission spectra collected from the same location on the sample but different excitation areas. The pump intensity for all three spectra is 17.5 $MWcm^{-2}$ which is slightly higher than the threshold level.

Based on the shape of the nanonail and discussion presented above, we therefore suggest that the observed emission peaks can be attributed to the confined resonant modes inside the hexagonal shaped head of the nanonail. The hexagonal shaped dielectric cavity can support several different kinds of optical modes. Figure 4.4 shows three possible resonant cavity modes that can occur in the hexagonal head of the nanonails; (a) a F-P type, (b) a quasi-WGM, and (c) a WGM. In the F-P type mode in which the light

bounces back and forth between the two opposing edge facets (see Figure 4.4 (a)). The observation of this type of lasing has been reported by Zhao,[150] although the cavity size in their work was much larger. In the second type of resonant mode, the light travels around the cavity in a loop path. The light ray trace illustrated in Fig. 4(b) is one possible resonant mode where the photons strike the boundary at 30^{o} relative to the normal of the boundary surface (hereafter to be referred to as a quasi-WGM). The light ray trace illustrated in Figure 4.4 (c) is a WGM where the photons strike the boundary at 60^{o} relative to the normal. The quasi-WGM is less confined inside the cavity than the WGM and more light can leak out of the boundary surface due to the smaller incident angle.

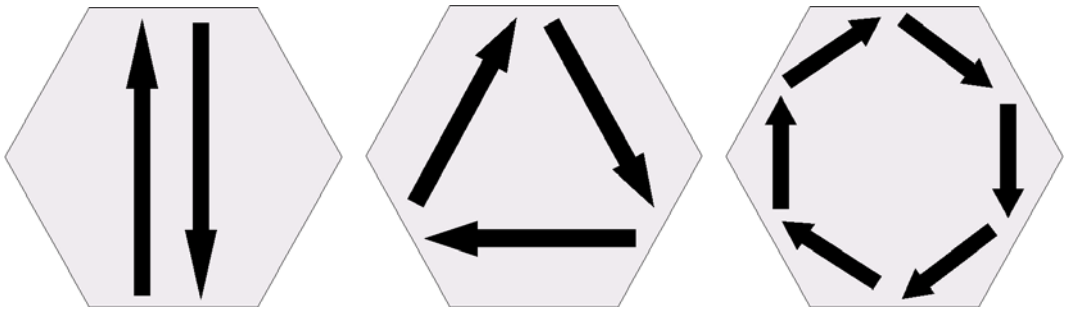

(a) **(b)** **(c)**

Figure 4.4: Schematics of three possible resonant cavity modes that can take place in the hexagonal head of the nanonails; (a) F-P type, (b) quasi-WGM, and (c) WGM.

The wavelength (λ) of the resonant WGM shown in the Fig. 4(c) can be calculated based on a simple plane wave model as[13]

$$\lambda = nL \Big/ \left[N + \frac{6}{\pi} \arctan\left(\beta\sqrt{3n^2 - 4}\right) \right] \qquad (4.1)$$

where n (= 2.3) is the refractive index of ZnO at 390 nm wavelength range, and the factor ß is determined by the polarization. L is the path length for a complete round trip which is equal to ~ 3 × 650 nm (650 nm is the size of the nanonail head, Figure 4.4(c)) for the WGM. The integer N is the mode number. WGMs are preferentially TM polarized.[13] Assuming a transverse-magnetic (TM) polarization, the mode number N is found to be 10 for the emission peak at 388.8 nm (Figure 4.3) using equation 4.1.

Using the refractive index of ZnO (n = 2.3), the critical angle of the total internal reflection at the ZnO-air boundary is calculated to be 25.8°. So the photons of the WGM are completely confined inside the cavity provided that all edge facets are free of defects. For the FP type mode the reflectivity at the boundary is 15.5%, resulting in partial confinement. The path length for a round trip is ~2 × 650 nm for FP mode and ~3 × 650 nm for the WGM. The mode spacing (Δλ) for both the WGM and the FP mode is given by

$$\Delta\lambda = \lambda^2 / (nL) \qquad (4.2)$$

where λ is the wavelength (388.8 nm), n is the refractive index (2.3), and L is the path length for a round trip. Eq. 2 gives mode spacings of 49.1 nm and 32.7 nm for the F-P mode and the WGM, respectively. Since the mode spacing is much greater than the line width of the ZnO spontaneous emission band, and those modes beyond the emission

spectrum range will not obtain optical gain from ZnO, we expect to see only one emission peak for each type of mode for a single nanonail in the spectrum.

With the excitation area reduced to 2 μm^2, we were able to probe a single nanonail at a time. Different locations showed a different emission spectra which depend on the specification of the nanonail being probed and its orientation with respect to the pump laser beam and collection optics. The majority of the spectra can be categorized into two groups; one group exhibits a very sharp peak (FWHM = 0.08 nm) and a flat background virtually free of spontaneous emissions (Figure 4.5 b), and the other group has relatively broad peak (FWHM = 0.52 nm) with a spontaneous emission background (Figure 4.5 a).

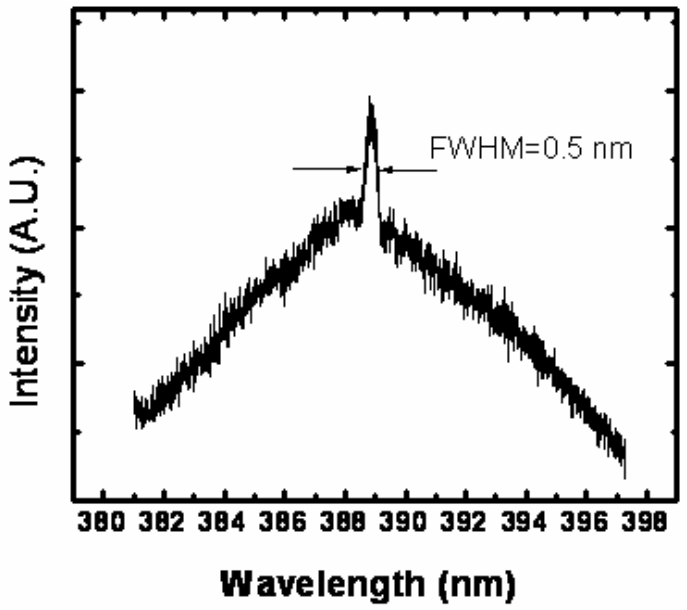

(a)

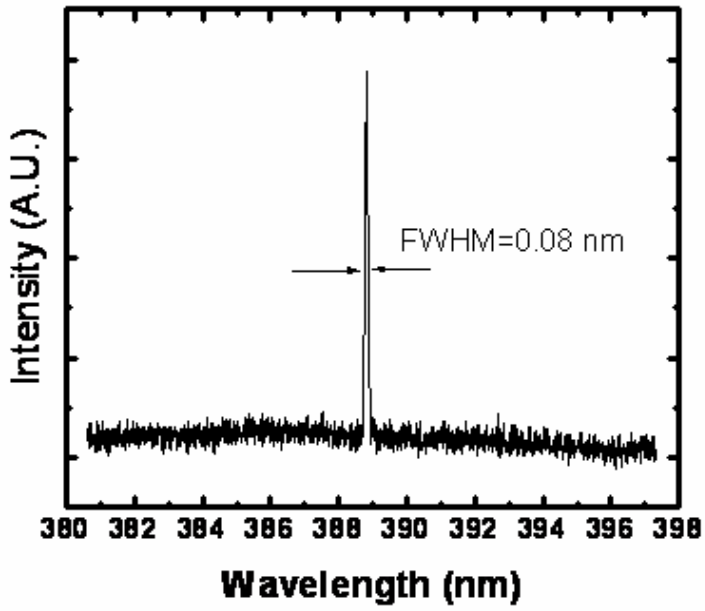

(b)

Figure 4.5: Lasing emission collected from single ZnO nanonails. (a) Emission peak corresponds to a resonant mode with small Q factor. (b) Emission peak corresponds to a resonant mode with high Q factor and very small loss.

The very small FWHM of the emission line observed in Figure 4.3 is an indication of a long photon life time as a result of the good optical confinement and small loss in the cavity. The Q factor for this emission mode can be calculated using $Q = \nu/\Delta\nu$, where ν is the peak frequency (7.72×10^{14} Hz), and $\Delta\nu$ is the peak width (1.59×10^{11} Hz). A Q factor of 4900 was obtained. If the optical absorption and scattering inside the cavity are neglected, the Q factor can be related to the reflectivity of the two facets in a F-P resonator by[151]

$$Q = \frac{2 n L_c \pi}{\lambda (1 - \sqrt{R_1 R_2})} \tag{4.3}$$

where R_1 and R_2 are the reflectivities of the two facets, and L_c is the cavity length. Using the reflectivity of 15.5% at the ZnO-air boundary for the normal incident, the calculated Q factor from Equation 4.3 is only 29. The Q factor could be even smaller if other losses like the scattering inside the cavity are also considered. Therefore, for a cavity having dimensions of the nanonail, F-P type resonance provides a very low Q factor. More generally, the Q factor of a regular polygonal cavity can be written as[152]

$$Q = \frac{\pi n m D R^{m/4}}{2\lambda(1 - R^{m/2})} \sin(\frac{2\pi}{m}) \tag{4.4}$$

where m is the number of facets of the cavity, D is the diameter of the circle that circumscribes the polygon, and R is the reflectivity of the facet. To get a Q factor of 4900 as demonstrated by the FWHM of the emission peak in Figure 4.5, the reflectivity needs to be 99.75% according to Equation 4.4, which can only be achieved by total internal reflection. Although total internal reflection predicts a 100% reflectivity, light can still

escape at the corners of the cavity.[10] We thus conclude that only the WGM type resonances are responsible for the high Q factor observed in the emission spectrum.

Numerical simulations were performed using Matlab ® to study the electric field intensity distribution of the resonant mode in a 2D hexagonal cavity. The boundary of the cavity was assumed to be perfectly reflective for the mode we studied ---- an assumption that is valid for the WGMs. Figure 4.6 shows one of the low order TE modes that can exists in such a cavity. It clearly shows a six-fold symmetry in the filed distribution. Note that the electric field is more concentrated near the circumference of the cavity than at its center, as can be expected from the nature of the WGMs.

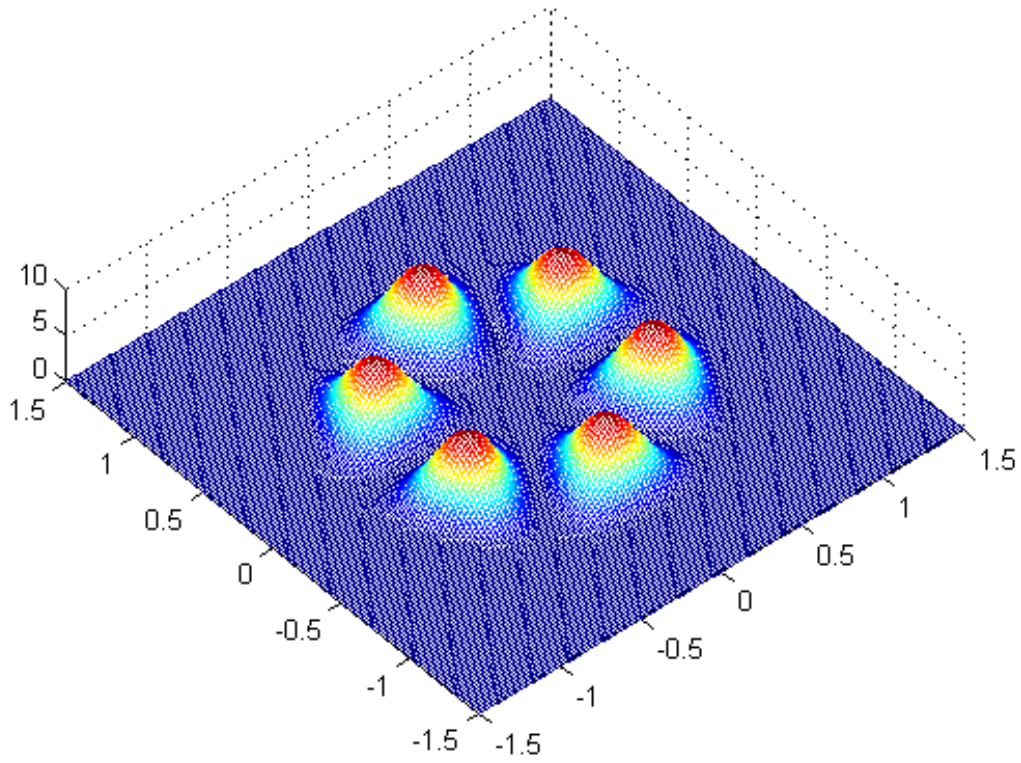

Figure 4.6: Electric field intensity distribution of mode TE_{31} in 2D hexagonal cavity with perfect confinement.

4.4 Conclusions

In summary, we have demonstrated that ultraviolet lasing occurs in single ZnO nanonails synthesized by thermal chemical vapor deposition. The lasing threshold was found to be 17MWcm^{-2}. Very sharp emission peaks (FWHM=0.08 nm) were observed in the single mode emission spectrum, indicating a high Q factor for the cavity formed by the hexagonal shaped nanonails. The possibilities of different lasing mechanism have been discussed. We suggest that the lasing action occurs in WGMs which are confined inside the head of the hexagonal cavity. This material may find application in fluorescent biosensors.

CHAPTER 5

EFFECT OF POST-GROWTH ANNEALING TREATMENT ON THE PHOTOLUMINESCENCE OF ZINC OXIDE NANORODS

5.1 Introduction

The large band gap of 3.37 eV and an exciton binding energy of 60 meV make ZnO a promising material for optoelectronic applications. In addition, one-dimensional ZnO structure such as a nanowire/rod exhibits novel properties due to the quantum confinement effects and/or its very large surface-to-volume ratio. The luminescence of ZnO exhibits a band edge UV emission peak and a broad visible emission band related to deep level defects. The mechanism of the defect related electron-hole recombination process in ZnO has been intensively investigated, but still remains a controversial subject.

Among the different mechanisms proposed to explain the visible luminescence, oxygen vacancies (V_O) have been widely considered as the most probable candidate, although no consensus could be reached regarding the charge state of the oxygen vacancy; *i.e.*, singly ionized[153] or doubly ionized.[154] Oxygen annealing was usually employed to modify the level of oxygen deficiency in ZnO. However, contradictory results regarding the effect of annealing on the emission properties of ZnO have been reported. In some experiments,[155, 156, 157] oxygen annealing has enhanced the intensity of

the visible luminescence band and has reduced the intensity of the band edge UV luminescence. However, in some other experiments, the exact opposite trend was observed,[158, 159] It was also found that the change in relative intensities of the visible and UV luminescence band depends on the annealing temperature.[160, 161] Different synthetic methods and post-growth treatments result in different surface conditions. The concentration and spatial distribution of intrinsic or extrinsic defects also varies among samples. When comparing such photoluminescence data, caution needs to be exercised since all of the above mentioned factors can contribute to the characteristics of photoluminescence (PL).

In this work, post-growth annealing was carried out to investigate the mechanism governing the visible luminescence in ZnO nanorods synthesized using a thermal chemical vapor deposition (CVD) method.

5.2 Experiment

The ZnO nanorods were grown on Si(100) substrates at 550^{o}C using a thermal CVD procedure. Zn powder (99.998%, Aldrich) was placed in an Al_2O_3 boat located inside the quartz tube reactor. Argon was used as a carrier gas. The residual oxygen in the reactor tube and/or in the Ar gas was exploited as an oxygen source.

Room temperature photoluminescence spectra were collected using a JY spectrometer with a thermoelectrically-cooled charge coupled device (CCD) detector. For excitation, the 325 nm (20 mW) line of a He-Cd laser (Kimmon Electric) was used. All PL spectra were collected using the same settings. Special care was taken to ensure that the same location in the sample was probed when collecting PL.

5.3 Result and discussion

Figure 5.1 shows a scanning electron micrograph (SEM image contributed by Ms. Heewon Seo) of the as-grown ZnO nanorods. It can be seen that the majority of the nanorods have a diameter of between 100 nm and 200 nm and a length of several micrometers; a few nanorods that have diameters smaller than 50 nm can also be found. The morphological and size distribution of the nanorods was fairly uniform across the sample. The original sample wafer was cut into three pieces (labeled as sample A, B, and C) and these samples were subject to different annealing/oxidation processes.

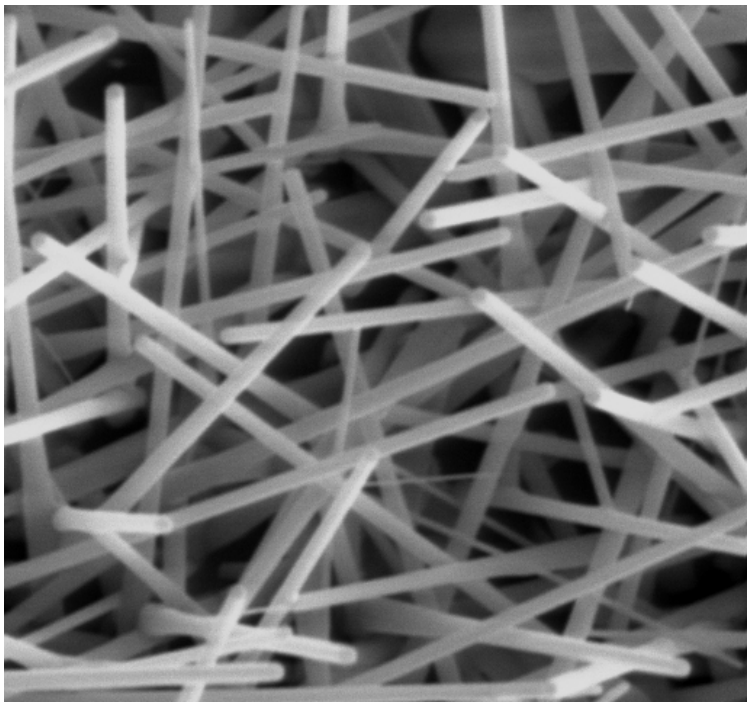

Figure 5.1: SEM image of the as-grown ZnO nanorods (Image size; $6 \times 6\,\mu m$).

The Raman spectrum (Figure 5.2) shows a strong and very sharp E_2 mode peak, which is an indication of long phonon life-time and high crystal quality. Before the annealing process, a room-temperature photoluminescence (PL) spectrum was collected (The spectrum from the unannealed sample are shown in Figure 5.3 and 5.4). As can be seen from the spectrum, the near-band-edge (NBE) peak and the green luminescence (GL) band are located at about 3.2 eV and 2.5 eV, respectively. No other obvious visible luminescence could be identified from the PL spectrum. The ratio of the integrated intensity of the NBE to that of the GL (I_{UV}/I_{Vis}) is 0.4.

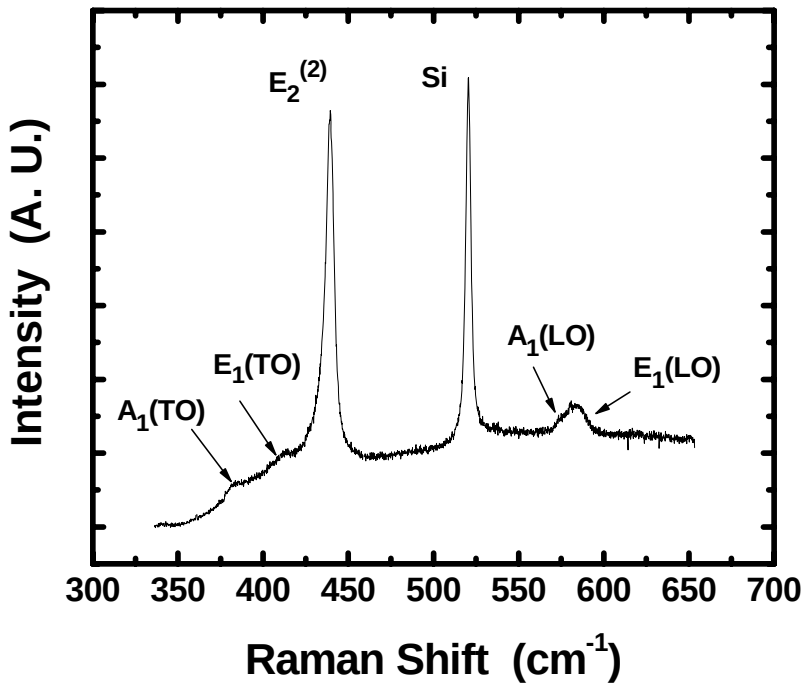

Figure 5.2: Room temperature Raman spectrum of the as-grown ZnO nanorods.

Sample A was annealed in an oxidation furnace under flowing oxygen at 400°C for 1hr. The PL spectrum of sample A collected after the oxygen annealing exhibited no changes.

Oxygen annealing of sample B was carried out at 800°C for 1hr. The PL spectrum of sample B collected just after the oxygen annealing is shown in Figure 5.3. The intensity of GL was enhanced and that of NBE was greatly reduced, decreasing I_{UV}/I_{Vis} to 0.023. Sample B was then annealed in a vacuum at 800°C for 1 hr after the annealing chamber was evacuated. After this subsequent vacuum annealing, the original PL spectrum (Figure 5.3) was recovered, increasing I_{UV}/I_{Vis} to 0.42.

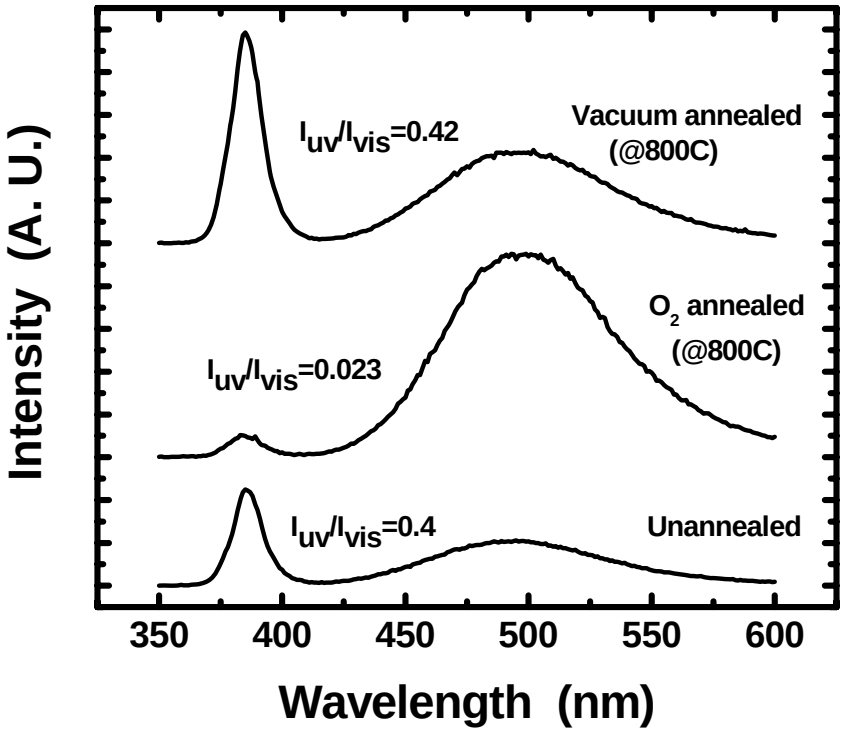

Figure 5.3: Room temperature PL spectra of the ZnO nanorods (sample B) collected before annealing, after O_2 annealing, and after subsequent vacuum annealing.

To make sure that the observed change in PL spectrum after oxygen annealing is related to the presence of oxygen, sample C was annealed in a vacuum at 800^{o}C for 1 hr. The PL spectrum (Figure 5.4) collected just after the vacuum annealing is similar to that of the as-grown sample but with an even greater I_{UV}/I_{Vis} of 0.9. Then, sample C was left in the oxidation furnace under oxygen flow at room temperature for 2 days. The PL spectrum (Figure 5.4) collected after the oxygen exposure is similar to that of the oxidized sample B and I_{UV}/I_{Vis} was reduced to 0.077.

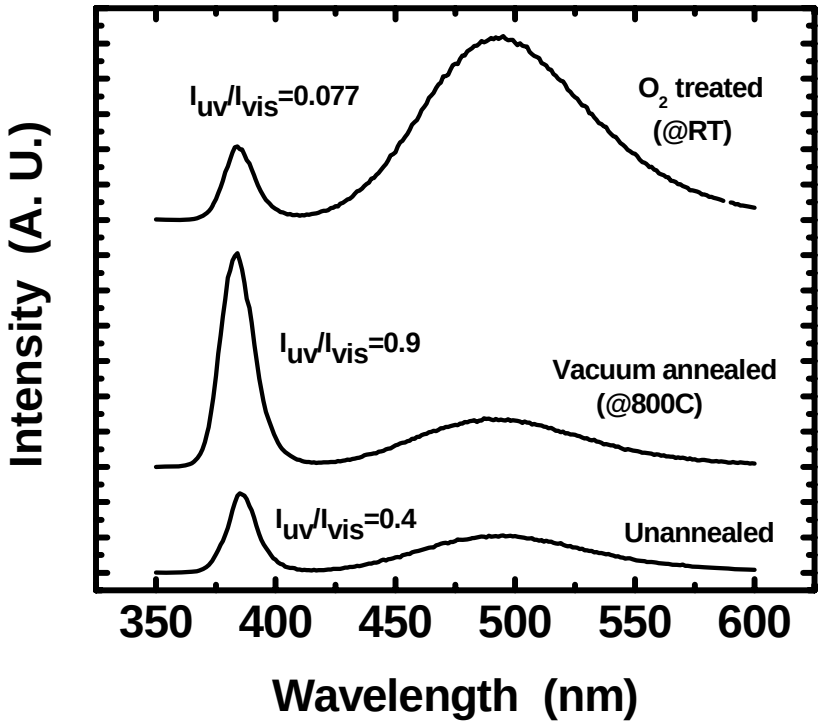

Figure 5.4: Room temperature PL spectra of the ZnO nanorods (sample C) collected before annealing, after vacuum annealing, and after the subsequent exposure to oxygen ambient for 2 days.

To make sure that the annealing condition used in this work does modify the level of oxygen deficiency in ZnO, two ZnO bulk crystals (MTI Corp.) were annealed along with sample B and sample C, respectively. After annealing, the electrical resistivities of the ZnO bulk crystals were measured. It was found that the resistivity of the oxygen annealed bulk crystal (annealed along with sample B) was increased by more than one order of magnitude as compared to that of the unannealed bulk crystal, while the resistivity of the vacuum annealed bulk crystal (annealed along with sample C) was decreased by more than two order of magnitude as compared to that of the unannealed sample. The excess zinc content or higher level oxygen deficiency in the vacuum annealed ZnO gives rise to the lower resistivity. The same resistivity dependence on the level of oxygen deficiency has been reported for ZnO grown or annealed in different ambient gas conditions.[162, 163] Despite the obvious changes in oxygen composition due to the annealing processes, our experiments, as well as those performed by other groups[3, 4, 5] that employed various annealing conditions, have shown the opposite trend in PL to what is predicted by the V_O model.

Although the detailed nature of the recombination center that is responsible for GL is still under debate, it is generally agreed that GL is a surface related process. Both a comparative study of nanowires with different surface to volume ratios[164] and direct imaging using cathodoluminescence microscopy[165] have shown that the GL process is localized at the surface of the nanowires. Li *et al*. has found that the GL can be suppressed by coating the ZnO nanostructure with a surfactant.[166] Surface passivation by coating ZnO thin film with alkali halide,[167] or a dielectric layer[168] can also suppress GL and enhance NBE.

Chemisorption of oxygen at the ZnO surface is known to cause an upward band bending by capturing electrons in a region near the surface.[169] This adsorption process can occur under air at room temperature, producing upward band bending in as-grown ZnO. Upon excitation, the photo-generated electrons and holes near the surface are swept to opposite directions across the depletion region, thus greatly reducing their chances of recombination through excitonic processes. Upon arriving at the surface, holes can be captured by the adsorbed oxygen ion, followed by transformation into a physisorbed state. The physisorbed oxygen is less stable and is prone to be desorbed from the surface, thus reducing the thickness of the depletion layer. This phenomenological model has been also utilized to explain the UV illumination enhanced PL effect of ZnO thin films.[170]

The depth of the surface recombination layer was estimated to be 30 nm.[9] Muth *et al.*[171] have measured the absorption coefficient of ZnO, and have found a large absorption coefficient of ~160,000 cm^{-1} at 325 nm, which corresponds to a penetration depth of ~60 nm. Since a substantial number of photo-generated electro-hole pairs fall within the surface depletion region, any change of the depletion layer will have a significant impact on the overall characteristics of luminescence. A direct consequence is the effect of ambient gas on the luminescence. The more the chemisorption of oxygen occurs at ZnO surface, the fewer holes are left in the bulk to recombine with electrons through excitonic processes. Instead, more holes will be trapped near the surface where they can recombine non-radiatively with electrons *via* surface states or radiatively *via* deep level defect states to generate GL.[2]

Lagowski *et al*. [14] found that the 0.72 eV thermal activation energy needed for the charge transfer through the surface potential barrier is the major limiting factor for determining the chemisorption rate. They found that the rate of charge transfer increases linearly with increasing oxygen pressure and exponentially with increasing temperature. In our experiment, annealing at an elevated temperature in an oxygen ambient greatly increases the number of chemisorbed oxygen, leading to the enhanced GL. On the other hand, vacuum annealing removes the excess chemisorbed oxygen and recovers the original PL.

Even with the formation of the depletion layer, the GL still cannot occur without enough deep level recombination centers that exist near the surface. Had V_O been the dominant recombination center for GL, we would have seen a decrease of GL after the oxygen annealing since the V_O had been removed. The same rationale can be applied to the vacuum annealing regardless of the change in band bending. Thus, something other than V_O is playing a dominant role as the recombination center for GL.

Cu impurities have also been considered as possible recombination centers that can lead to GL. Garces *et al*.[172] concluded that the broad structureless GL at 500 nm is due to DAP recombination between an electron bound to a shallow donor and a hole loosely bound to the Cu^+. At a high enough temperatures impurity ions can drift along the direction of an external electric field. Korsunska *et al.*[173] has reported an increase of GL intensity near the cathode and a decrease near the anode when an external electric field was applied across a ZnO single crystal at 600-700^{o}C. They attribute the change in GL to the electro-diffusion of Zn interstitial (Zn_i). The same group also reported that Cu

impurities in CdS drifted from anode to cathode in the form of Cu_i^+ under the influence of external electric field.[174]

We found that the observed change in PL after each annealing process can be explained by a model based on both band bending and migration of impurities. We believe that two major processes occur during the oxygen annealing: (1) an increase in the amount of chemisorption of oxygen at the surface, followed by band bending at the near surface region, and (2) migration of positively charged impurity ions or Zn_i to the surface under the influence of the built-in electric field in the depletion region. Since a substantial amount of photogenerated holes are swept to the surface, the segregation of the recombination centers for GL such as copper impurity ions or Zn_i-related complex in the surface region increases the chance of GL transitions near the surface. Owing to the concentration of Zn_i near the surface, conduction electrons transported to the surface region are more susceptible to the capture of the shallow donor state created by Zn_i, and subsequently recombine with the trapped holes to generate GL. Those holes not trapped by impurity ions or defect complexes are then captured by the adsorbed oxygen or other surface states, causing the desorption of oxygen or nonradiative recombination with photogenerated electrons. Due to the interception of the segregated impurity ions, fewer holes can reach the surface oxygen to cause the desorption. Thus, the segregated impurity ions can act as traps to reduce the number of photogenerated holes reaching the chemisorbed oxygen, which is also in favor of GL.

Let us now look at the two processes occurring during the vacuum annealing: (1) desorption of surface oxygen and a lesser degree of band bending when compared with the unannealed sample, and (2) migration of impurity ions or Zn_i, which is similar to

what oxygen annealing will produce but to a lesser extent. After the vacuum annealing, the width of the depletion layer is greatly reduced and the band becomes flat, resulting in a strong NBE and a weak GL in PL (Figure 5.4). After the subsequent exposure to oxygen ambient for 2 days, the surface will be covered with oxygen again, followed by band bending. This re-adsorption of oxygen decreases NBE and increases GL, as is shown in Figure 5.4. It is interesting to note that the PL of the sample C collected after exposure to oxygen ambient is more like that of the sample B after oxygen annealing, and shows more prominent GL when compared to the original PL of the as-grown sample. This is due to the fact that the redistribution of the defect states creates more recombination centers near the surface. Therefore, the result of the vacuum annealing and the subsequent exposure in oxygen is similar to that obtained by just a single oxygen annealing step. Finally, when the oxygen-annealed sample B was subsequently vacuum-annealed, the resulting PL was very similar to the original PL. This change, however, is solely due to the desorption of oxygen.

The band bending and the dynamics of photo-generated electron-hole pairs are illustrated in Figure 5.5 for the sample B when it undergoes three different stages; as-grown, after oxygen annealing and after subsequent vacuum annealing. A similar set of energy band diagrams can be given to the sample C by switching the order of Figure 5.5 (b) and (c).

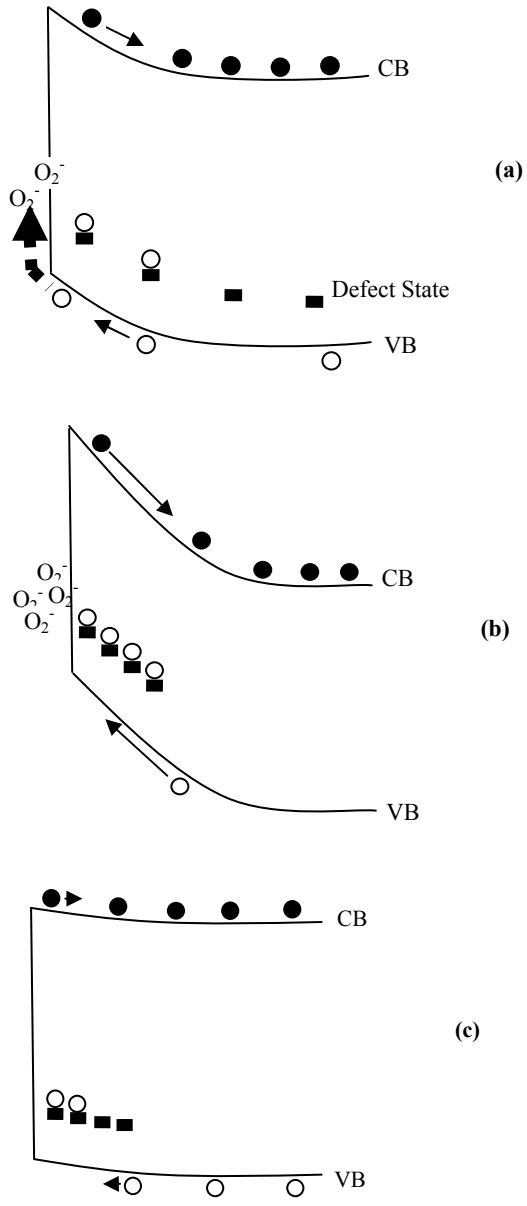

Figure 5.5: Schematics of the energy band diagram (not scaled) that illustrate the band bending and dynamics of the photogenerated electron-hole pairs near the surface of sample B when it was illuminated by above band-gap excitation at three different stages: (a) as grown, (b) after oxygen annealing, and (c) after subsequent vacuum annealing. The capturing of photogenerated holes by chemisorbed oxygen ions is depicted by the broken arrow. Also shown is the migration of the acceptor-like state created by impurity ions.

At a low annealing temperature of 400°C, adsorption and desorption of oxygen still occur at a lower rate, but significant diffusion of impurities or Zn_i in ZnO requires higher temperatures as dictated by the temperature dependence of the diffusion coefficient; $D = D_0 \exp(-E_A/k_BT)$. For zinc interstitial diffusion in ZnO, $D_0 = 1.7 \times 10^2$ cm^2/s, and $E_A = 3.3$ eV.[175] For Cu diffusion in ZnO, $D_0 = 2 \times 10^7$ cm^2/s, and $E_A = 4.8$ eV,[23] thus Cu diffusion requires even higher temperatures than Zn_i diffusion due to a larger activation energy E_A. The high temperature needed for the diffusion of impurity (or Zn_i) explains the insignificant change in the PL of sample A (annealed at 400°C).

As for the identity of this defect state, Cu^+ seems like a good candidate, but the source of Cu contamination in the growth process can not be determined. A Zn_i related complex has also been suggested as the recombination center of GL,[21] but interstitial Zn^+ was shown to diffuse to the surface to form [Zn^{2+}-O^{2-}] surface pairs,[176] which emit UV light. Radiative transition may occur from the conduction band or shallow donors to Zn vacancy acceptor at around 2.6 eV[177], but V_{Zn} is negatively charged in its stable state. Therefore, the upward band bending will drive V_{Zn} away from the surface. More information is needed to identify this deep level defect state.

Unlike the ZnO nanostructure, the influence of post-deposition annealing on ZnO films is also related to the change in the microstructure of the films. According to the structure zone model,[178] a process of coalescence and major grain growth result in a porous and cracked structure in the films when annealed at an elevated temperature.[8, 179] On the other hand, ZnO nanostructures usually exhibit a single crystal structure and have

a small dimension. Therefore, structural defects can easily migrate out, and the localized strain can be relieved by bending during the growth.

5.4 Conclusions

We have carried out oxygen and vacuum annealing experiment to study the mechanism of GL of ZnO nanorods synthesized by thermal CVD. Our experiment results reveal that V_O is not the dominant recombination center for GL observed in the present sample. A model based on the interplay between the band bending at the surface and the migration of positively charged impurity ions or Zn_i was proposed, which satisfactorily explains the observed change in PL after each annealing process. Its sensitivity to the oxygen ambient may be a useful property for the ZnO nanorod to be used in oxygen gas sensing applications.

CHAPTER 6

RAMAN CHARACTERIZATION OF ELECTRONIC PROPERTIES OF ALLIGNED GALLIUM NITRIDE NANORODS

6.1 Introduction

Raman spectroscopy is considered as one of the most versatile characterization tools since a plethora of information about materials can be extracted from a Raman study alone. For example, structural properties such as crystal orientation, disorder and stress, and electronic properties such as free carrier concentration, carrier mobility, piezoelectric polarization and band bending can be obtained. Traditionally, capacitance-voltage (C-V) and Hall measurements have been utilized to determine the concentration and mobility of free carriers in gallium nitride (GaN). Determination of electronic properties with Raman spectroscopy has major advantages over the above-mentioned techniques due to the following reasons: 1) Raman spectroscopy is a non-contact and non-destructive method. 2) Raman spectroscopy has superior spatial resolutions as compared to the other electronic characterization methods. By using micro-Raman spectroscopy, regions as small as ~1 μm in diameter can be probed with ease. This enables the depth-profiling of the films by probing the sidewall of the films. Recent development of near-field Raman spectroscopy promises much more improved spatial

resolution, which will play an important role in probing electronic properties of nanostructures such as nanowires and quantum dots. 3) Under proper materials combinations and by selecting the proper wavelength of excitation, electronic properties of a buried layer can be extracted, which may be difficult to realize with other techniques. 4) Electronic parameters of films on conducting substrates can be independently obtained.

In polar semiconductors, the longitudinal-optical (LO) phonons couple strongly with plasmon through the macroscopic electric field.[180] The coupling between the plasmon and the LO phonon produce two coupled LO phonon-plasmon (LPP) modes, the ω_+ (LPP^+) and the ω_- (LPP^-) (high- and low-frequency modes, respectively).[181] The coupling is through the macroscopic electric fields of these excitations. The high frequency LPP^+ mode behaves like an LO phonon at low carrier densities. The frequency of the LPP^+ mode increases with carrier concentration, and eventually corresponds to that of the plasmon. Such a mode was proposed by Varga,[182] and first observed in GaAs by Mooradian and Wright.

When plasmon damping is substantial, the coupling will be displayed as a shift of LO phonon mode. In GaN, it was observed that the LO phonon modes couple with the plasmon mode. Comparing with the uncoupled LO phonon peak, the LPP mode is shifted to higher frequency and asymmetrically broadened with increasing free carrier concentration. The LPP mode also depends on the LO phonon damping as well as the plasmon damping constant, and this fact can be exploited to extract the charge concentration and carrier mobility from Raman spectra. Raman spectroscopy has been used to deduce the electron concentration and electron mobility in thin films and bulk

GaN by many researchers.[183, 184, 185, 186, 187, 188, 189, 190] However, this method has not been applied to the analysis of electronic properties of nanowires, where it will be difficult to employ electronic techniques due to the difficulty of contact preparation. Therefore, in the present work, we have demonstrated that electronic properties of nanowires can be obtained *via* Raman spectroscopy. We also considered the effect of local laser heating on the Raman peak shift since there is a substantial increase in the temperature of the nanowire during Raman measurements due to the lack of heat dissipation. GaN nanorods sample used in this work was contributed by Y. S. Park *et al* at Dongguk University, Seoul, Korea.

6.2 Experiment

In the present investigation, c-axis aligned GaN nanorods were grown on a Si (111) substrate using a radio-frequency plasma-assisted molecular beam epitaxy (RF-PAMBE). The Si substrate was degreased and then etched with HF and followed by thermal treatment at 900^{o}C for 30 minutes. The cleaned substrate showed a reconstructed (7x7) surface with measurement of reflection high-energy electron diffraction (RHEED). All growth procedures of GaN nanorods were carried out under N-rich conditions. The rf-plasma power was kept constant at 350 W during the growth. The growth rate was 1.5 μm/h. The details of the sample preparation steps can be found elsewhere.[191]

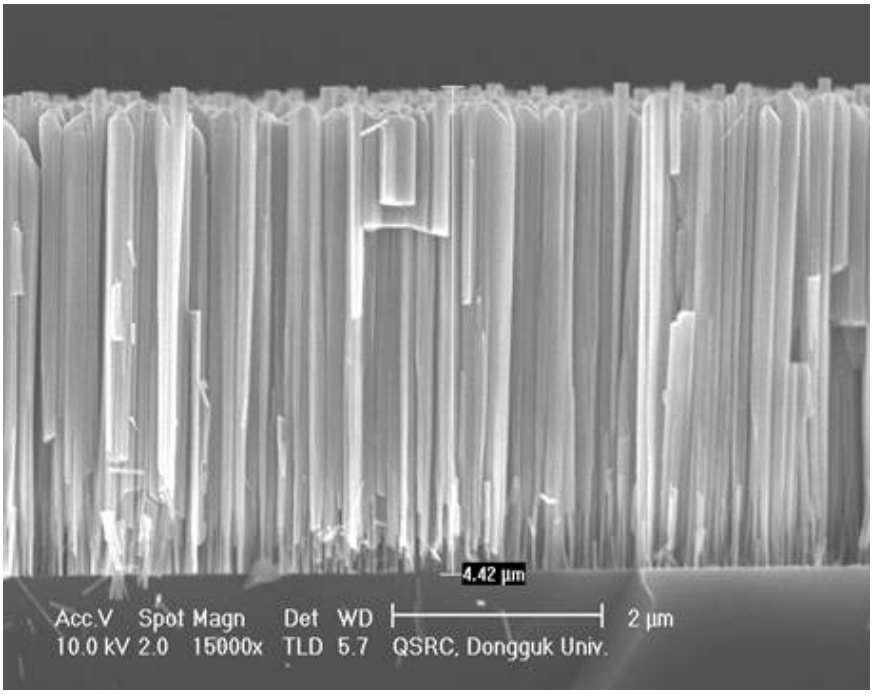

Figure 6.1: A cross-sectional high-resolution SEM micrograph of the GaN nanorods grown on a Si(111) substrate.

The morphology of the sample was characterized using a high-resolution scanning electron microscopy (HR-SEM image contributed by Y. S. Park *et al*). Micro-Raman spectroscopy was carried out using a backscattering geometry. The wavelength of 441.6 nm line of the Kimmon Electric's HeCd laser was used as an excitation. The polarization states of the incident and the scattered beam were not analyzed. The laser beam with a nominal power of 80 mW was focused onto a spot with ~5 μm in diameter. The Jobin-Yvon's spectrometer with a thermoelectrically-cooled charge coupled device (CCD) detector was used to collect the Stokes' and anti-Stokes' Raman spectra.

6.3 Result and discussion

According to group theory, $A_1(z) + 2B_1 + E_1(x,y) + 2E_2$ optical modes are predicted at the Γ point of the Brillouin zone of hexagonal GaN[192]. The two E_2 modes are Raman active, the A_1 and E_1 modes are both Raman and infrared active, and the two B_1 modes are optically silent. Since the A_1 and E_1 modes are polar, they split into longitudinal optical (LO) and transverse optical (TO) components. According to the Raman selection rules, only the $E_2^{(1)}$, $E_2^{(2)}$, and $A_1(LO)$ modes can be observed with the $z(-,-)\underline{z}$ scattering geometry of this experiment. Figure 6.2 shows the Stokes and anti-Stokes Raman spectrum for the GaN nanorods, the Raman spectrum of a single crystal bulk GaN sample (Kyma Technologies, Inc.) was also collected for comparison. The electron concentration of the bulk GaN obtained using C-V measurement is $<10^{16}$ cm^{-3}. It was also assumed that the bulk GaN is strain-free. In addition to the theoretically allowed modes, $A_1(TO)$ and $E_1(TO)$ are also present in the Raman spectrum of nanorods, which is possibly caused by the imperfect alignment of the nanorods and the finite collection angle of the microscope objective.

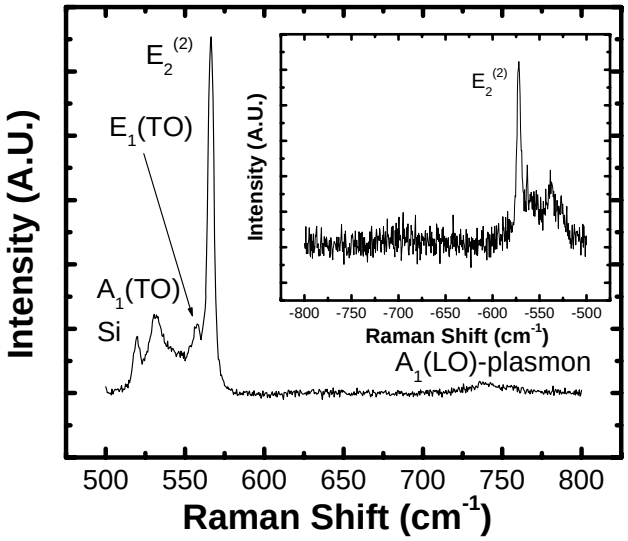

(a)

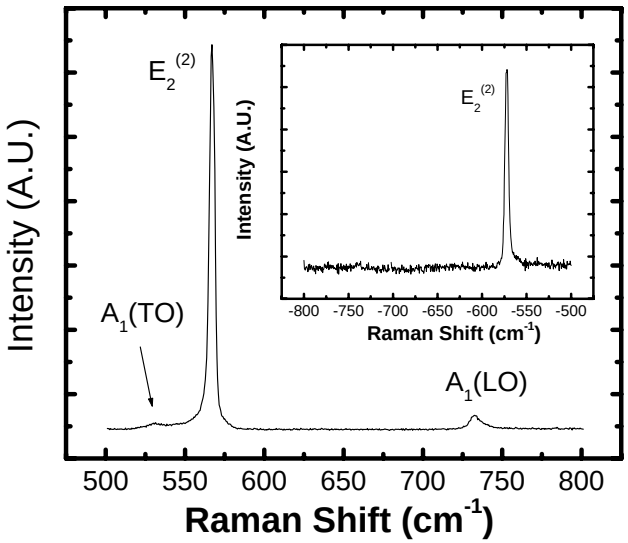

(b)

Figure 6.2: Raman spectrum of the GaN nanorod (a) and bulk GaN (b). The insets show the anti-Stokes part of the spectrum.

Upon illumination using focused laser beam, the local temperature of the sample can reach several hundred degrees Celsius, possibly causing downshift and broadening of the Raman peak. This heating effect is especially pronounced in micro- or nano-structured materials due to their reduced thermal conductivities.[193] Without taking the thermal effect into account, the experimental results can be misleading.[14] Therefore, the integrated intensity of E_2 phonon peaks for both Stokes (I_S) and anti-Stokes (I_{AS}) were obtained to estimate the local temperature of the samples. The local temperature was calculated using the following relationship;[194]

$$I_S / I_{AS} \propto \exp\left(\hbar\omega_{E2} / k_B T\right) \tag{6.1}$$

where ω_{E2} is the E_2 phonon mode frequency. The estimated temperatures are 505 K and 460 K for the GaN nanorods and the single crystal bulk GaN, respectively.

The temperature dependence of Raman scattering in GaN has been studied.[195, 196] Based on Li *et al.*'s work,[15] we have obtained the Raman peak positions using the estimated temperature (hereafter to be referred to as "temperature-calibrated" peak position). It was found that the temperature-calibrated E_2 mode frequency for the single crystal GaN is the same as what was measured by Raman scattering. The temperature-calibrated A_1(TO) and E_1(TO) mode frequencies of the GaN nanorods are also in excellent agreement with the observed experimental values. This can be an alternative way to verify the estimated temperatures. The measured E_2 mode frequency of the nanorods is very close to the temperature-calibrated value. Therefore, it can be concluded that our nanorods are relatively strain-free.

Due to the scattering geometry used and the aligned nature of the nanorods used in this work, we can expect that the observed LO peak is the A_1(LO) mode. Therefore, no intermixing between the E_1(LO) and A_1(LO) mode can be expected. In order to determine the exact position of the uncoupled A_1(LO) mode, it is important to prevent A_1(LO) mode from being coupled with E_1(LO) mode since the intermixing of the two LO phonon modes leads to the change of the LO mode peak position[197]. Since A_1(LO) phonons polarize along the c-axis of the Wurtzite unit cell, the plasmon oscillations coupled to it also polarize in that direction. Subsequently the physical parameters involved in the process such as the damping constants are those defined along c-axis assuming the anisotropy of the wurtzite crystal.

The intensity of the LPP mode is given by;[198]

$$I(\omega) = Const. \bullet A(\omega) \bullet \mathrm{Im}\left[-\varepsilon(\omega)^{-1}\right], \qquad (6.2)$$

where the $A(\omega)$ corrects for the deformation-potential and electro-optic mechanism.[18] By fitting the Raman spectrum of the LPP mode with the functional form given in Eq. 2, the plasmon frequency ω_P, plasmon damping constant γ and phonon damping constant Γ can be extracted. The free carrier concentration n_e and mobility μ can then be derived from the plasmon frequency and plasmon damping constant as:

$$\omega_P = \sqrt{\frac{4\pi n e^2}{\varepsilon_\infty m^*}}, \qquad (6.3)$$

$$\gamma = \frac{e}{m^* \mu}, \qquad (6.4)$$

where m^* is the effective mass of the free carrier, and $m^* = 0.22\, m_e$ in the case for GaN.[199]

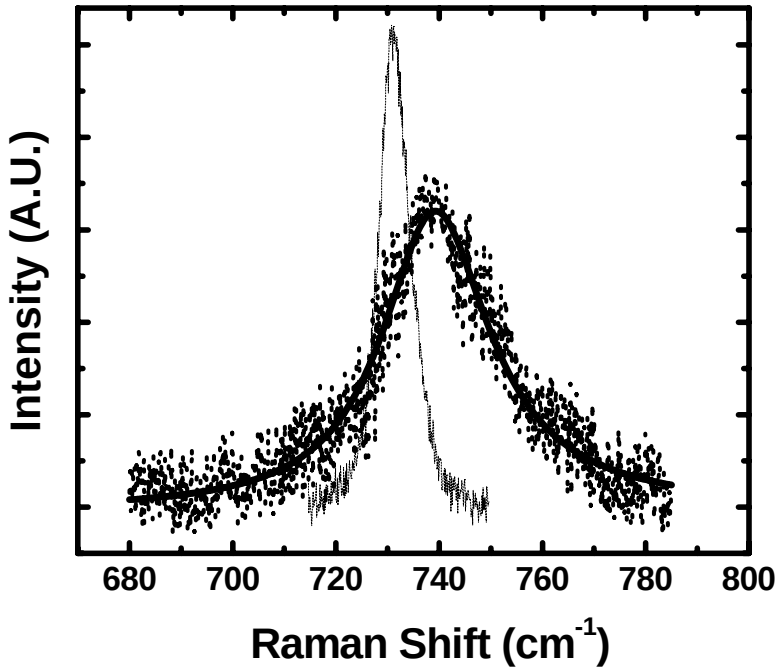

Figure 6.3: Raman spectrum of the LO phonon-plasmon coupled mode for GaN nanorod (dotted line) and bulk GaN (dashed line). The thick solid lines are the fitting curves for nanorods by line-shape analysis. The shift and broadening of the LPP mode is obvious with respect to the uncoupled A_1(LO) mode of the bulk GaN.

Satisfactory fitting results were obtained in the region of LPP mode for GaN nanorods and single crystal bulk GaN, as shown in Figure 6.3. The fitting parameters and results are summarized in Table 6.1. The electron concentration and mobility obtained from line shape analysis are 3.3×10^{17} cm^{-3} and 140 cm^2/Vs, respectively. The frequency for A_1(TO) mode, ω_{TO}, can be readily obtained from the Raman spectrum. However, care must be taken to specify the frequency for the uncoupled A_1(LO) mode: ω_{LO}.

Instead of blindly using 734 cm^{-1} which has been widely adopted as the frequency for the uncoupled $A_1(LO)$,[200] the temperature-calibrated $A_1(LO)$ frequency should be used as ω_{LO}. Since the electron concentration of the undoped bulk GaN is $<10^{16}$ cm^{-3}, the $A_1(LO)$ mode in the undoped bulk GaN is not shifted due to the LO phonon-plasmon coupling.[201] Therefore, we can use the value as the frequency of the uncoupled $A_1(LO)$ mode at T = 460K. We then downshifted it by 1.3 cm^{-1} to obtain the frequency of the uncoupled $A_1(LO)$ mode at T = 505K (the temperature of the nanorods), thus $\omega_{LO} = 731.2\ cm^{-1}$ is the frequency of the uncoupled $A_1(LO)$ mode used in the curve fitting. This precaution is further justified by the fact that the frequency of the $A_1(LO)$ mode of the undoped bulk GaN is at 732.5 cm^{-1} which is downshifted comparing with 734 cm^{-1} due to the elevated temperature.

Table 6.1: Parameters used in the line-shape analysis, and the fitting results for the plasma frequency, phonon damping constant and plasmon damping constant.(all in cm^{-1})

	ω_{TO} [a]	ω_{LO} [b]	$\varepsilon_{\infty\perp}$ [c]	ω_P	Γ	γ	$n_e(10^{17}\,cm^{-3})$	$\mu\,(cm^2/Vs)$
Nanorod	531.7	731.2	5.35	169.4	18.4	347	3.3	140

[a] Obtained by fitting the Raman spectrum with Lorentzian function.
[b] Calculated by considering the temperature effect. Obtained using the uncoupled $A_1(LO)$ peak position of the bulk GaN.
[c] Reference 19.

6.4 Conclusions

In summary, we have investigated the Raman scattering of aligned GaN nanorods grown by PAMBE. It was determined by Raman spectroscopy that the GaN nanorods are relatively strain-free. The free carrier concentration as well as electron mobility of the GaN nanorods were obtained by the line shape analysis of the coupled A_1(LO) phonon-plasmon mode. The electron concentration and mobility of electron obtained from line shape analysis are 3.3×10^{17} cm^{-3} and 140 cm^2/Vs, respectively. The local temperature of the nanorod sample was estimated based on the ratio of Stokes to anti-Stokes Raman peak intensity. Since the position of the LO phonon peak was found to be dependent on both the temperature and the LO phonon-plasmon coupling, it is crucial to consider temperature effect in determining the frequency of the uncoupled LO phonon mode for the line shape analysis. The frequency of A_1(LO) mode of an undoped bulk GaN was used as a reference to determine the frequency of the uncoupled A_1(LO) phonon mode of the GaN nanorods.

CHAPTER 7

OPTICAL SPECTROSCOPIC ANALYSIS OF SELECTED AREA EPITAXIALLY RE-GROWN GALLIUM NITRIDE

7.1 Introduction

Gallium nitride (GaN) has been considered a desirable material for high-power electronic device applications. One of the promising candidates for GaN-based power electronic device is metal-insulator-semiconductor field effect transistors (MISFETs). Successful fabrication of MISFETs necessitates high quality gate dielectric layers with a low density of interface states, semiconductor channel with high electron concentration, and high quality ohmic contacts for source and drain contacts. In the case of Si-based MISFET fabrication, ion implantation is frequently employed to produce highly doped region for ohmic contacts. However, this is not easily achievable in GaN-based MISFET since high temperature annealing is required to activate implanted dopants.[202] As an alternative, a GaN MISFET with selected area epitaxially re-grown n^+ layer was proposed and synthesized.[203] When MOVPE growth is performed over large areas using these low temperature conditions,[2] a poor (rough) surface morphology evolves. It is therefore necessary to examine the GaN grown in selected areas as to crystal quality and

other properties such as dopant incorporation rates that are expected to differ from those of large area uniform growth structures.

To fabricate highly functional devices, the material characteristics of the re-grown layer need to be elucidated to a high degree of spatial selectivity. Micro-Raman and micro-photoluminescence (PL) spectroscopy allows for contactless and non-destructive analysis for small volumes with high spatial resolution. Therefore, they are widely used for materials characterization in such micro-devices and substructures. In the present work, we have demonstrated that important electrical and structural properties can be obtained by using micro-Raman and PL spectroscopy collectively.

In polar semiconductors like GaN, the longitudinal-optical (LO) phonons couple strongly with plasmons through the macroscopic electric field.[204] The coupling between the plasmon and the LO phonons produce two coupled LO phonon-plasmon (LPP) modes, the ω_+ (LPP^+) and the ω_- (LPP^-).[205] Such modes were proposed by Varga,[206] and first observed in GaAs by Mooradian and Wright.[4] In this work, the LPP^+ mode was exploited to extract the carrier concentration and mobility from the Raman scattering experiment. The residual stress and crystal quality of overgrown layers were also determined, and results were compared with results of an undoped layer. Micro-photoluminescence spectroscopy was also performed as a complementary optical spectroscopy technique. The GaN MISFET sample investigated in this work was contributed by Y. N. Saripalli *et al* at Department of Materials Science and Engineering, NC State University.

7.2 Experiment

An ~500 nm thick undoped GaN buffer layer was deposited on a c-plane sapphire substrate using an organo-metallic vapor phase epitaxy (OMVPE) following standard previously published procedures for III-V semiconductors.[207, 208] A thin AlN buffer layer was first deposited on sapphire at 500 ^{o}C to facilitate 2D growth. Mesa regions were photolithographically defined and recess etched with a reactive ion etching using a hard mask of Cr-Ni over a SiN_x dielectric. A highly doped n^+ layer was grown selectively on the etched GaN buffer layer by OMVPE using a silicon nitride dielectric mask to define the etched recess in the source-drain region, silane (SiH_4) was used as the dopant source in the re-grown layer. A growth temperature of 800 ^{o}C facilitates the re-growth at the selected regions. The thickness of the re-grown layer is determined by a Dektak profilometer to be ~300 nm. An SEM image and the schematic cross-sectional view of the re-grown structure are shown in Figure 7.1. (SEM image contributed by Y. N. Saripalli *et al*). Complete details of equipment and processes used in the sample preparation procedure can be found elsewhere.[2]

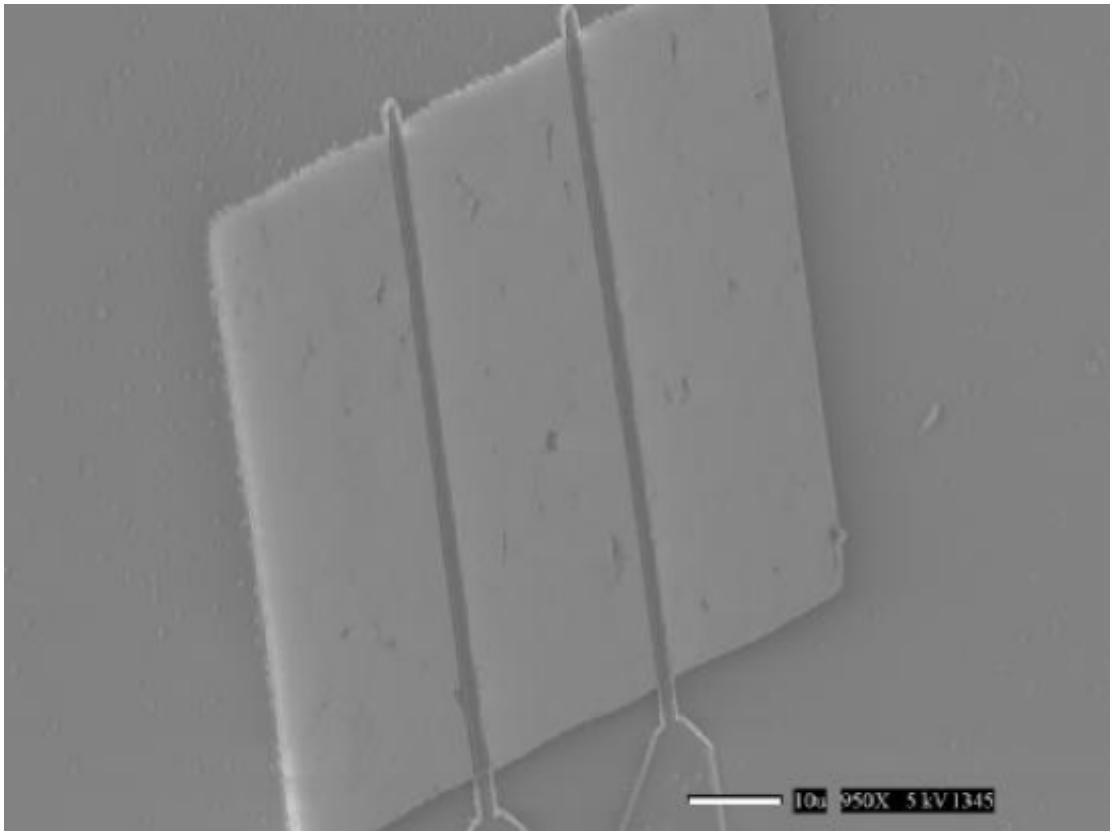

(a)

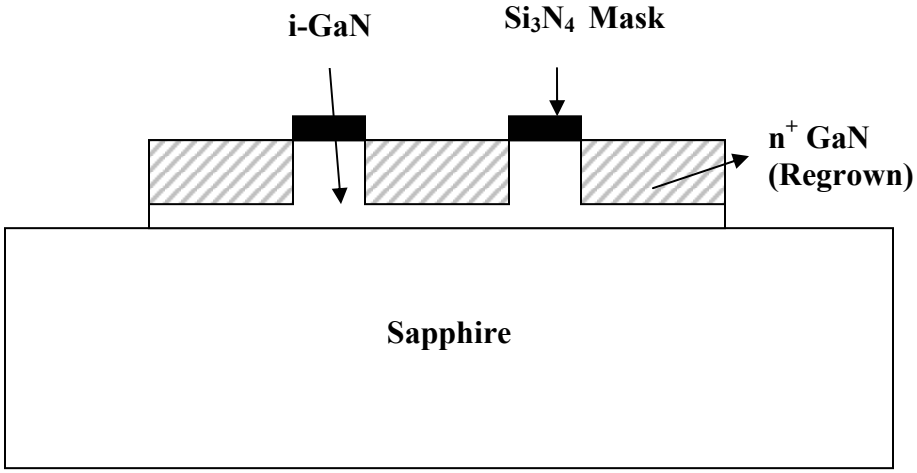

(b)

Figure 7.1**:** (a) Tilted SEM image of the GaN MISFET after source-drain region re-growth. (b) Schematic cross-sectional view of the structure after re-growth (not to scale).

Micro-Raman spectroscopy was carried out at room temperature using an optical microscope (Zeiss Axiotech) coupled with a spectrometer (Jobin-Yvon). The 441.6 nm line from a He-Cd laser (Kimmon Electric) was used for excitation, and the backscattering geometry was used for the Raman measurement. The polarization states of the incident and the scattered light were not analyzed. The laser beam (nominal power of 80 mW) was focused onto a spot with ~5 μm in diameter on the sample surface. Stokes' and anti-Stokes' Raman spectra were collected using the spectrometer with a thermoelectrically-cooled charge coupled device (CCD) detector. Micro-photoluminescence spectroscopy was performed using the 325 nm line from the He-Cd laser. Spectral analysis was carried out using OriginPro software.

7.3 Result and discussion

Wurtzite GaN belongs to the C_{6v}^4 space group, and group theory predicts $A_1(z) + 2B_1 + E_1(x,y) + 2E_2$ optical modes at the Γ point of the Brillouin zone of GaN.[209] Among these optical modes, the two E_2 modes are Raman active, the A_1 and E_1 modes are both IR and Raman active, and the two B_1 modes are silent. Because of the polar nature of III-V compounds, the A_1 and E_1 modes split into TO and LO components.

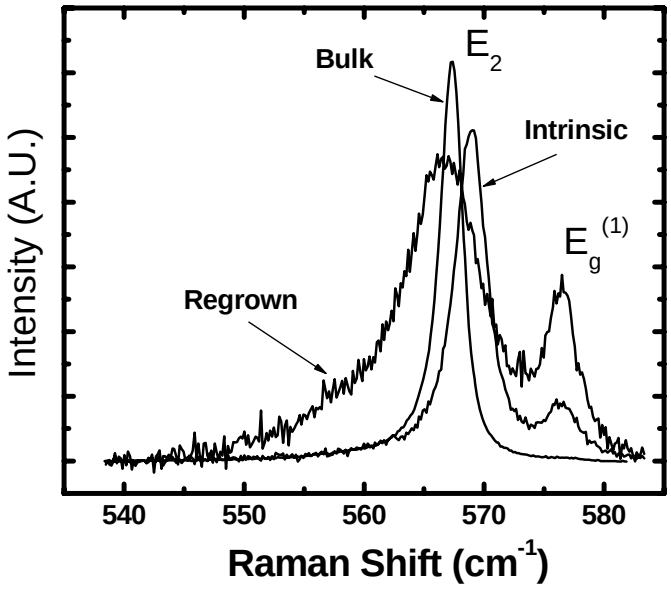

(a)

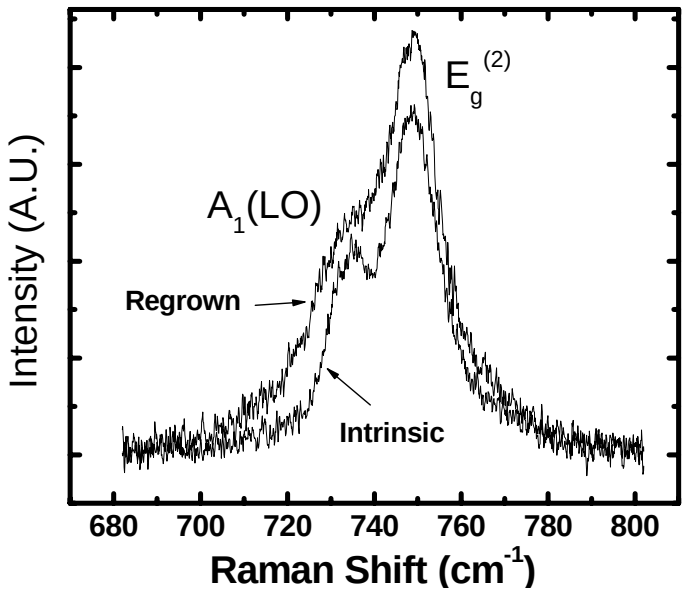

(b)

Figure 7.2: Room temperature Raman spectrum of E_2 (a) and A_1(LO) modes (b) of the intrinsic and re-grown GaN layers. The $E_g^{(1)}$ mode of sapphire substrate is also observed. The E_2 mode of the bulk GaN crystal is also plotted for comparison. The size of the excitation laser beam is about 5 μm in diameter.

Giving that the Z(X,-)$\underline{Z}$ scattering geometry is used and the c-axis of GaN is along Z-direction, only the Raman peaks due to A_1(LO), $E_2^{(1)}$ and $E_2^{(2)}$ modes are experimentally observed according to the selection rule. Figure 7.2 shows the $E_2^{(2)}$ mode of the re-grown GaN layer. The Raman spectra of the undoped GaN layer before processing and a bulk GaN crystal (Kyma Technologies, Inc.) were also collected for comparison. The sapphire E_g mode (at 576 cm^{-1}) was observed since GaN is transparent to the 441.6 nm line of the excitation laser. Since the re-grown GaN was presumably deposited on the undoped GaN buffer layer, it seems that the Raman spectrum collected at the regrown region will contain a substantial contribution from the undoped buffer layer. However, both the Raman spectrum and the PL spectrum (will be discussed later) collected at the re-grown region show that the undoped buffer layer left on the sapphire substrate after etching has a negligible effect on Raman and PL spectrum. Hereafter, we will regard the spectrum collected from the re-grown region as solely from the re-grown GaN.

The peak position and full width at half maximum (FWHM) of the Raman $E_2^{(2)}$ mode were determined by fitting the Raman peaks in Figure 7.1 with Lorentzian functions, and the results are listed in Table 7.1. The FWHM of the undoped intrinsic GaN layer are close to that of the bulk crystal, indicating well crystallized lattice structures. We also observed an up-shift of 1.7 cm^{-1} in the intrinsic GaN layer, comparing with that of the bulk crystal. Assuming that the bulk crystal is stress free and neglecting the hydrostatic stress contribution from point defects, this downshift implies a compressive biaxial stress in the intrinsic GaN layers. This residual stress in GaN thin film grown on sapphire substrates is usually observed due to the lattice mismatch and the

different thermal expansion of the two materials. Kisielowski *et al.* found that a biaxial stress of 1 GPa shifts the $E_2^{(2)}$ Raman peak of GaN by 4.2 ± 0.3 cm^{-1}.[210] This gives a 0.4 GPa biaxial compressive stress in the intrinsic GaN layer.

Table 7.1: Measured Raman mode frequencies and their FWHMs

	Intrinsic	Regrowth	Bulk	Sapphire
E_2	568.9	566.7	567.3	
FWHM	2.5	4.8	1.8	
A_1(LO)	733.2	745.4	732.8	
FWHM	5.5	30.1	4.7	
$E_g^{(1)}$				576.5
$E_g^{(2)}$				748.8

The $E_2^{(2)}$ Raman peak of the re-grown GaN layer is broadened and shows a slight down-shift (0.6 cm^{-1}), which corresponds to a 0.19 GPa biaxial tensile stress. It has been reported that the $E_2^{(2)}$ Raman peak becomes broadened and the residual stress relaxed as the doping concentration increases.[10] The residual biaxial stress is fully relaxed when the doping concentration reaches 1.6×10^{19} cm^{-3}.[211] The incorporation of Si produces negligible change for the lattice constant; it is believed that the residual stress relaxes through the Si-induced generation of misfit dislocation at the substrate-film interface.[10, 212] Romano *et al.*[213] proposed that crystallite coalescence caused tensile stress will increase with increasing Si doping concentration. Note that the $E_2^{(2)}$ Raman peak of the re-grown GaN layer does *not* contain any contribution from the $E_2^{(2)}$ Raman peak of the

intrinsic buffer layer lying underneath as demonstrated by the absence of any shoulder peak at 569 cm^{-1}. This fact helps to justify the claim regarding the contribution of the intrinsic buffer layer.

To make sure that the observed Raman peak shift is *not* caused by the different local temperatures existing in different regions, we collected the anti-Stokes part of the Raman spectrum for the intrinsic, re-grown GaN layer and the bulk GaN crystal. The integrated intensity of E_2 Raman mode for both Stokes (I_S) and anti-Stokes (I_{AS}) were obtained, their intensity ratio is determined by the temperature as[214]:

$$R = \frac{I_S}{I_{AS}} = \gamma \left(\frac{\omega_l - \omega_p}{\omega_l + \omega_p} \right)^4 \frac{\alpha_l + \alpha_S}{\alpha_l + \alpha_{AS}} \exp\left(\frac{\hbar \omega_p}{k_B T} \right), \tag{7.1}$$

where $\alpha_l, \alpha_S, \alpha_{AS}$ are the absorption coefficients for laser, Stokes and Anti-Stokes light, respectively. ω_l , ω_p are the frequencies of the laser and the E_2 phonon mode. The 4^{th} power term considers the different scattering cross section for Stokes and anti-Stokes light, while the factor γ describes the detection efficiency of the optical system.

If one is not interested in the absolute temperature but only the temperature difference (ΔT) between two samples, then Equation 7.1 can be simplified to exclude all the parameters except the exponential:

$$\frac{R_1}{R_2} = \exp\left[\frac{\hbar \omega_P (T_2 - T_1)}{k_B T_1 T_2} \right] \approx \exp\left[\frac{\hbar \omega_P \Delta T}{k_B T^2} \right], \tag{7.2}$$

where $R_{1,2}$ is the Stokes-Antistokes ratios of sample 1 and 2.

Assuming that the bulk GaN crystal is at room temperature, letting $T = 300\,K$ in Equation 7.2, the temperature differences between the intrinsic and regrown GaN layers and the bulk GaN crystal were found to be within 13 ^{o}C for our experiments.

Li *et al.*[215] have studied the first-order Raman scattering of Wurzite GaN film grown on sapphire, and simulated the temperature dependence by considering thermal expansion and multiple-phonon processes. In our case, the Raman peak shift due to the estimated temperature difference was calculated to be less than 0.2 cm^{-1} by using their model. Therefore we can safely disregard this thermal effect.

The LO phonon-plasmon coupled mode has been extensive studied in doped polar semiconductors such as GaN.[216, 217, 218] When the plasmon frequency ω_P approaches the frequency of LO phonon ω_{LO}, the collective oscillation of the free-electron gas starts to couple with the LO phonon via their associated longitudinal electric field. The coupled mode splits into two branches: the high-frequency plasmon like LPP^{+} mode and the low-frequency TO phonon-like LPP^{-} mode. In our case the plasmon is overdamped: $\omega_P < \gamma$ (γ is the plasmon damping constant), therefore only the LPP^{+} mode can be observed. The increasing free-electron concentration will cause the coupled mode to shift to higher frequency and broaden asymmetrically as shown in Figure 7.3. This fact was exploited to extract the carrier concentration and mobility from a Raman scattering experiment.[219]

The excitation laser light interacts with the LO phonon through an electro-optic mechanism and deformation potential, and interacts with the plasmon through an electro-optic mechanism and charge density fluctuation. To describe the Raman spectral line

shape of the LPP^+ mode, only the deformational potential and the electro-optic mechanism is needed. The intensity of the LPP^+ mode is given by:[220]

$$I(\omega) = Const. \bullet A(\omega) \bullet \mathrm{Im}\left[-\varepsilon(\omega)^{-1}\right], \tag{7.3}$$

$$\begin{aligned} A(\omega) &= 1 + 2C\frac{\omega_{TO}^2}{\Delta}\left[\omega_P^2\,\gamma\left(\omega_{TO}^2 - \omega^2\right) - \omega^2\Gamma\left(\omega^2 + \gamma^2 - \omega_P^2\right)\right] \\ &+ C^2\left[\frac{\omega_{TO}^4}{\Delta\left(\omega_{LO}^2 - \omega_{TO}^2\right)}\right]\left\{\omega_P^2\left[\gamma\left(\omega_{LO}^2 - \omega_{TO}^2\right) + \Gamma\left(\omega_P^2 - 2\omega^2\right)\right] + \omega^2\Gamma\left(\omega^2 + \gamma^2\right)\right\} \end{aligned}, \tag{7.4}$$

$$\Delta = \omega_P^2\,\gamma\left\{\omega^2\Gamma^2 + \left(\omega_{TO}^2 - \omega^2\right)^2\right\} + \omega^2\Gamma\left(\omega^2 + \gamma^2\right)\left(\omega_{LO}^2 - \omega_{TO}^2\right), \tag{7.5}$$

where C is the Faust-Henry coefficient.[221] ω_{LO}, ω_{TO} are the LO and TO phonon frequencies for A_1 mode. Γ is the phonon damping constant.

The dielectric constant in Equation 7.3 includes contributions from both the phonon and the plasmon:

$$\varepsilon(\omega) = \varepsilon_\infty\left[1 + \frac{\Omega^2}{\omega_{TO}^2 - \omega^2 - i\omega\Gamma} - \frac{\omega_P^2}{\omega\left(\omega + i\,\gamma\right)}\right], \tag{7.6}$$

Equations 7.3-7.6 were used to fit the experiment spectrum to obtain the three adjustable parameters: ω_P , γ and Γ. The parameters used in the curve fitting are listed in Table 7.2. The uncoupled A_1 mode frequency ω_{LO} and ω_{TO} was readily obtained from the Raman spectrum of the undoped bulk GaN crystal. The $E_g^{(2)}$ peak from the sapphire substrate was removed from the Raman spectrum (Fig. 2 (b)) prior to the line shape analysis. The fitted curves and the coupled modes after spectral subtraction are shown in Figure 7.3.

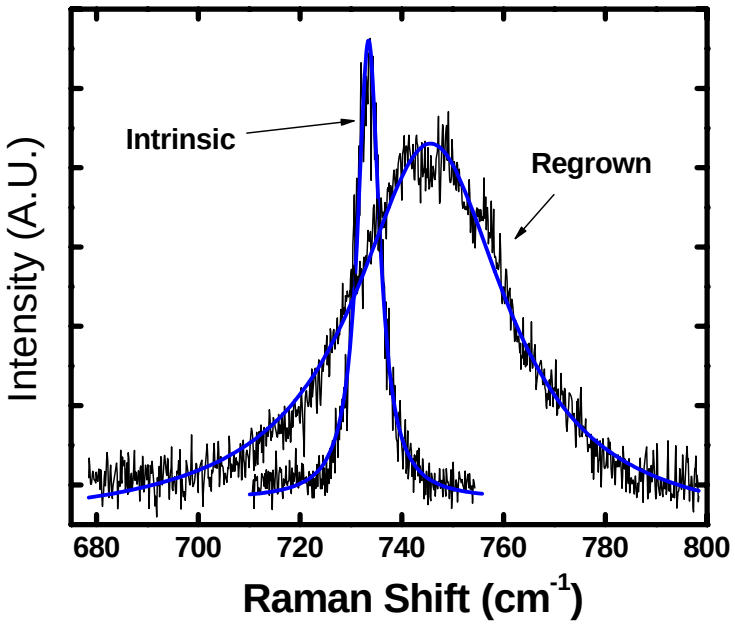

Figure 7.3: Curve fitting of LPP^+ mode of the intrinsic and re-grown GaN layer. The broken line is the measured spectral line after removing the $E_g^{(2)}$ peak of sapphire, the solid line is the fitted curve.

Table 7.2: Parameters used in the curve fitting and derived electrical properties. No fitting results were given for γ and Γ, since the line shape analysis method does not provide reliable result if the free-electron concentration is lower than 3×10^{16} cm^{-3}.[17]

	ω_{TO}	ω_{LO}	$\varepsilon_{\infty\perp}$	ω_P	Γ	γ	$n_e(10^{17}\,cm^{-3})$	$\mu\,(cm^2/Vs)$
Regrowth	532.3	732.8	5.35	204	42	286	**4.7**	**171**
Intrinsic	532.3	732.8	5.35	~ 40			< **0.3**	

Since the A_1 phonon polarizes along the c-axis, the plasmon oscillation coupled to it also polarizes in that direction. Subsequently the physics parameters involved in the process, like the damping constant, are those defined along c-axis assuming the anisotropy of the wurzite crystal. Once the plasmon frequency ω_P and plasmon damping constant γ were obtained, the carrier concentration n and the carrier mobility μ can be determined via:

$$\omega_P = \sqrt{\frac{4\pi n e^2}{\varepsilon_\infty m^*}} \ , \tag{7.7}$$

$$\gamma = \frac{e}{m^* \mu} \ , \tag{7.8}$$

where m^* is the effective mass of the free carrier. $m^* = 0.22\, m_e$ in GaN.[222]

A line shape analysis shows that the undoped GaN layer has a very low carrier concentration ($n_e < 3\times10^{16}$ cm^{-3}). This is also evidenced by the frequency and FWHM of the coupled mode, as can be seen in Figure 7.3. Since the line shape analysis method does not provide a reliable results if the free-electron concentration is lower than 3×10^{16} cm^{-3},[17] no fitting results were given for γ and Γ. Unintentional doping caused by diffusion of oxygen from sapphire substrate into a GaN film during growth process can form a degenerate thin layer at the interface.[223] [224] Huang *et al.*[225] found a very high free-electron concentration (8×10^{18} cm^{-3}) in a 1 μm thick layer at the interface using confocal Raman spectroscopy. Despite the fact that the intrinsic GaN layer studied in this work is only 500 nm think, no obvious peak shift or broadening in the LO phonon mode was observed. We thus can exclude the possibility of significant doping and/or formation of a degenerate interface layer in the undoped intrinsic GaN layer.

The free-electron concentration (4.7×10^{17} cm^{-3}) of the re-grown GaN, derived from the line shape analysis, is much smaller than the Si doping concentration (on the order of 10^{19} cm^{-3}, as determined by SIMS measurements). As an amphoteric impurity, a silicon atom can also act as an acceptor by substituting for a nitrogen atom. A more important aspect is that the incorporation of a high dose of impurity atoms may lead to high density of dislocations and other structural defects in GaN, which serve as deep compensation centers. Let us assume that the donor concentration is N_D, the concentration of the compensation centers is N_A, then the net carrier concentration is determined by $N_D - N_A$, which may be much smaller than the Si doping concentration.[226] Similarly, incorporation of Si at interstitial sites would likely form a high density of deep level compensating traps.

The larger LO phonon damping constant of the re-grown GaN and its broader $E_2^{(2)}$ peak comparing with the intrinsic GaN implies a higher density of structural defects exiting in the re-grown GaN. Note that the in-plane damping is more pronounced than the damping along c-axis.

The biaxial stress also causes LO phonon peak to shift. Since the measured 0.4 GPa biaxial stress only yields 0.3 cm^{-1} shift in A_1(LO) mode, we thus completely neglected the stress-induced shift in the coupled mode.

Figure 7.4 shows the PL spectra of the intrinsic and re-grown GaN layers and a bulk GaN crystal. The undoped intrinsic GaN layer exhibits a similar PL spectrum as that of the bulk GaN crystal: an intense near-band-edge (NBE) peak at 3.41 eV and a very weak yellow luminescence (YL) band located at about 2.2 eV. The YL is generally

attributed to the recombination at a Ga vacancy (V_{Ga}) related deep level, although definite determination of its origin remains as a subject of debate.[227, 228, 229]

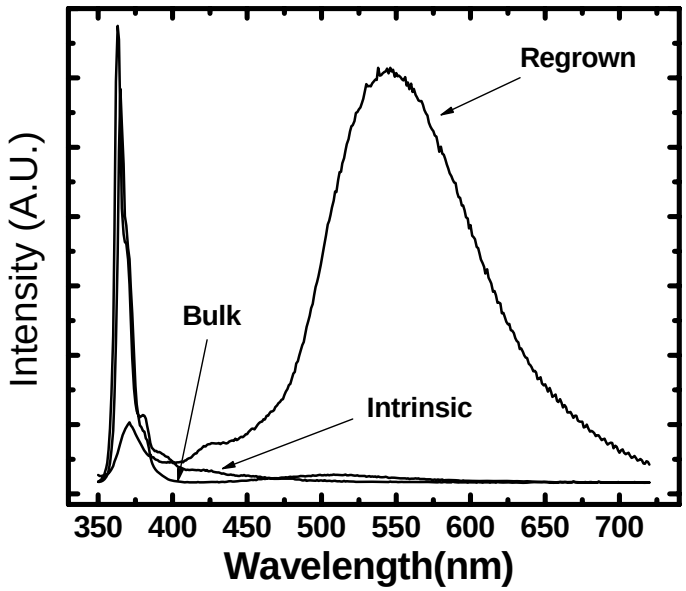

(a)

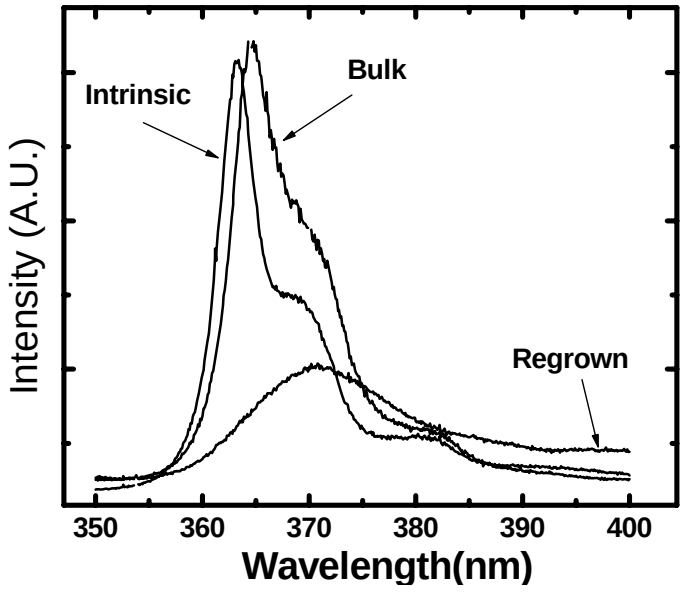

(b)

Figure 7.4: Room temperature PL spectrum (a) of the intrinsic and re-grown GaN layer. The spectrum of bulk GaN is plotted for comparison. Also shown is the zoom-in of the near-band-edge (NBE) part of PL spectrum (b).

The FWHM of the NBE peak of the intrinsic GaN layer is comparable to that of the bulk GaN sample and several phonon replicas can be found at the lower energy side. The PL spectrum of the intrinsic GaN layer is almost free of defect related visible luminescence bands, which shows that the intrinsic GaN layer has very low density of defects. This is important if the intrinsic GaN layer is to be used as the gate channel material in an electronic device.

The PL spectrum of the re-grown GaN layer exhibits an intense YL band and relatively weak NBE emission. It is generally believed that the YL intensity should decrease if the original V_{Ga} are replaced by Si donors, given that V_{Ga} is the main source of YL.[230, 231] The YL intensity was found to decrease at high level of Si doping ($N_{Si} > 10^{19}$ cm^{-3}).[232, 233] Despite the high level of Si doping in the re-grown GaN, the YL is greatly enhanced. This reveals that the majority of introduced Si atoms failed to substitute V_{Ga}, and could not contribute as donors. This analysis is in accord with the lower free carrier concentration (4.7×10^{17} cm^{-3}) found from the Raman spectrum. Another possible source for the enhanced YL is extended structural defects. Yang *et al*.[30] have shown that the YL intensity collected from the sapphire-GaN interface remained almost unchanged despite the increasing Si doping concentration, while the YL intensity collected from the front-side of GaN decreased for a certain range of doping levels. TEM images reveal that high densities of structural defects exit at the sapphire-GaN interface,[12, 234] this seems to imply that the high densities of dislocations and other defects at the sapphire-GaN interface may also be responsible for YL. Because these structure defects serve as deep compensation centers that can trap conduction electrons, high densities of structural defects will also be an origin of the lower carrier concentration in re-grown GaN.

The NBE peak in the PL spectrum is shown in Figure 7.4 (b) at higher resolution. The peak wavelength and its FWHM are summarized in Table 7.3. The blue-shift in the NBE peak of intrinsic GaN layer is caused by the same biaxial compressive strain observed in Raman spectrum. Using the stress (0.43 GPa) derived from the $E_2^{(2)}$ mode shift and the linear coefficient for stress-induced luminescence shift: 27 meV/GPa,[235] the blue- shift in the NBE peak of the intrinsic GaN layer is calculated to be 12 meV, which is exactly what is measured in Figure. 7.4 (b).

Table 7.3: Near-Band-Edge emission peak wavelength and FWHM

	Intrinsic	Regrowth	Bulk
NBE (nm)	363.1	369.9	364.4
FWHM (nm)	3	11.3	3.6

The 58 meV red-shift of the NBE colleted from the regrown GaN layer is too large to be solely attributed to the small tensile stress. The red-shift of the NBE peak and the peak broadening resulting from increased Si doping concentration has been attributed to the potential fluctuation induced by impurities.[236] [237] According to Yang *et al*.[30], the red-shift in NBE (ΔE_{UV}) can be related to the Si doping concentration N_{Si} through the empirical formula:

$$\Delta E_{UV} = K N_{Si}^{1/3} \qquad (7.9)$$

where the coefficient K is taken as -2.17×10^{-8} eV/cm. According to Equation 7.9, neglecting the small shift caused by the tensile stress, N_{Si} is calculated to be 2×10^{19} cm^{-3}, which agrees with the value measure by SIMS. Besides the NBE and yellow luminescence, a blue luminescence band can be observed at about 2.9 eV. This band is often observed in Si doped GaN, and is attributed to the V_{Ga} related complex. [238] Note that this band is absent when the re-grown GaN layer is excited from the sapphire side (Figure. 7.5).

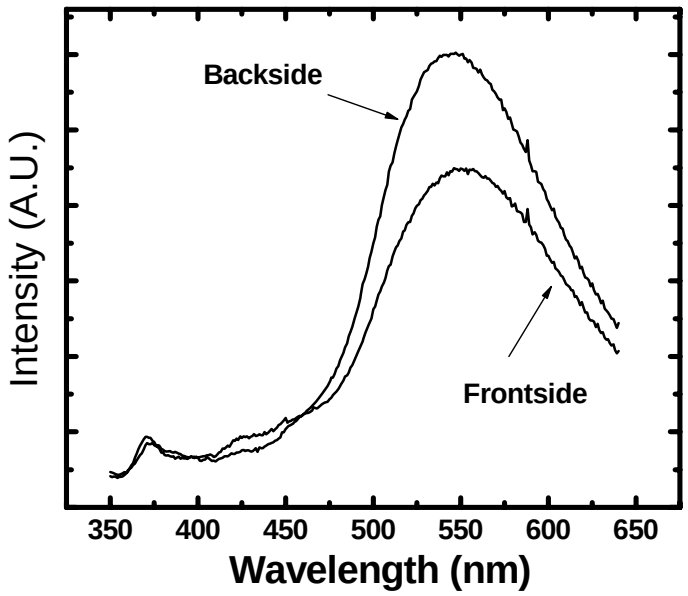

Figure 7.5: Room temperature PL spectrum collected from the back-side and front-side of the re-grown GaN layer.

We also collected the PL spectrum by exciting the sample from the sapphire side. Figure 7.5 shows the PL spectrum of the re-grown GaN layer when the back-side is

illuminated by the excitation laser. The intensity of YL increases and the intensity of NBE decreases slightly when excited from the sapphire side, which is similar to what has been reported in Ref. 22. Despite this small difference, an intense YL band and a weak NBE peak are the common spectral features of the re-grown GaN regardless of whether excitation occurred on the back-side or front-side. Since the PL spectrum of intrinsic GaN is quite different from that of re-grown GaN, it is reasonable to assume that the PL collected from the back-side of the re-grown region is mostly from the re-grown GaN layer, and not from the intrinsic buffer layer lying underneath. Muth *et al.*[239] have measured the absorption coefficient of GaN films grown on sapphire. A large absorption coefficient of $\sim 1.2 \times 10^5\,\mathrm{cm}^{-1}$ at 325 nm was obtained, which corresponds to a penetration depth of ~80 nm. Therefore, the thickness of the intrinsic buffer layer left underneath of the re-grown layer should be much smaller than 80 nm. This provides additional evidence that verifies the existence of the intrinsic buffer layer under the re-grown region.

7.4 Conclusions

In this work, a GaN MISFET with re-grown source-drain regions by selected area MOVPE n^+ layer has been analyzed by micro-Raman and micro-PL spectroscopy. The material properties of the re-grown n^+ layer and the intrinsic layer in the gate region were extracted using both spectroscopies. The free-carrier concentrations of the re-grown GaN layer and the intrinsic layer were determined by line shape analysis of the coupled plasmon-phonon mode to be $4.7 \times 10^{17}\,\mathrm{cm}^{-3}$ and $< 3 \times 10^{16}\,\mathrm{cm}^{-3}$, respectively. The relatively low carrier concentration resulting from either an inefficient substitution of V_{Ga} by Si, or a high density of structure defects that lead to the intense YL presented in the

PL spectrum. Both Raman and PL spectra show that the intrinsic layer is of very high quality.

From the shift of the $E_2^{(2)}$ Raman peak and the NBE PL peak, the biaxial compressive stress in the intrinsic layer was found to be 0.4 GPa, the residual stress was found to be fully relaxed in the re-grown layer. The Si doping concentration in the re-grown layer was found to be $2\times10^{19}\,\mathrm{cm}^{-3}$ by the red-shift of its NBE PL peak. Both Raman and PL spectra pointed out that the intrinsic buffer layer was much less than 80 nm thick, and that it had little effect on either spectrum of the re-grown layer.

CHAPTER 8

SUMMARY AND FUTURE DIRECTION

In summary, ZnO nanostructures were synthesized using two different thermal CVD growth methods under oxygen-deficient and oxygen-rich growth conditions. The as-grown nanostructures were of high crystal qualities as confirmed by XRD and Raman experiments. SEM images revealed a wide array of morphologies and sizes in ZnO nanostructures. Some correlations can be found between the predominant morphology of a sample and the growth conditions, although no general conclusion can be drawn regarding the correlation between the morphology and the growth parameters. Better control of morphology and size can be achieved by using an up-dated thermal CVD system.

The visible luminescence of ZnO nanostructures synthesized by the two different growth methods was markedly different, due to different native defects introduced during oxygen-deficient and oxygen-rich growth. The visible luminescence of the nanostructures synthesized in an oxygen-deficient environment was dominated by the blue-green band, while the oxygen-rich structures contained various emission bands but the blue-green band. The ZnO nanostructures were found to be mostly stress-free using Raman spectroscopy. Various broadening and enhancement effects in different Raman modes

were discussed. Samples synthesized by the up-dated growth system demonstrated less uniform optical properties that those synthesized by the oxygen-deficient growth method.

We have demonstrated that ultraviolet lasing occurs in single ZnO nanonails synthesized by thermal chemical vapor deposition. The lasing threshold was found to be $17MWcm^{-2}$. Very sharp emission peaks (FWHM = 0.08 nm) were observed in the single mode emission spectrum, indicating a high Q factor for the cavity formed by the hexagonal- shaped nanonails. The possibility of different lasing mechanisms has been discussed. We suggest that the lasing action occurs in WGMs which are confined inside a cavity formed by the hexagonal head of the nanonail.

We have carried out oxygen and vacuum annealing experiment to study the mechanism of GL of ZnO nanorods synthesized by thermal CVD. Our experiment results reveal that V_O is not the dominant recombination center for the GL observed in the present sample. A model based on the interplay between band bending at the surface and migration of positively charged impurity ions or Zn_i was proposed, which satisfactorily explains the observed change in PL after each annealing process. Its sensitivity to the oxygen ambient may be a useful property for the ZnO nanorod to be used in oxygen gas sensing applications.

Raman scattering of the aligned GaN nanorods has been investigated. It was determined by Raman spectroscopy that the GaN nanorods are relatively strain-free. The free carrier concentration as well as electron mobility of the GaN nanorods were obtained by line shape analysis of the coupled $A_1(LO)$ phonon-plasmon mode. The local temperature of the nanorod sample was estimated based on the ratio of Stokes to anti-Stokes Raman peak intensity. Since the position of the LO phonon peak was found to be

dependent on both the temperature and the LO phonon-plasmon coupling, it is crucial to consider temperature effect in determining the frequency of the uncoupled LO phonon mode for the line shape analysis.

Further work on the thermal CVD growth of ZnO nanostructures is needed in order to make the growth process for more controllable and more repeatable. This goal has been partially achieved using the up-dated thermal CVD system; however, the optical uniformity of the ZnO nanostructures should be further improved. It has been demonstrated that the surface depletion layer exerted substantial influence on the luminescence of ZnO nanostructures. We have also suggested that the existence of band bending gave rise to the electric-field induced effect, in order to explain the unusually strong LO phonon scattering observed in some samples. Further research is needed to verify this hypothesis. Other interesting electro-optic effects may also be induced by the built-in electric field in the surface layer, especially the effect of this electric field on the material's nonlinear optical properties, such as the second-order susceptibility $\chi^{(2)}$ of ZnO nanostructures. The simple picture of a uniform dielectric cavity is in fact an over-simplification for a ZnO nanostructure, and many new physics phenomena can be better explored once the existence of the surface layer is taken into consideration. Surface passivation of ZnO nanostructures need be tested experimentally in an attempt to improve the efficiency of the excitonic emission and field emission, possibly by orders of magnitude. For the timing being, only well-aligned nanostructures can be analyzed by the line-shape analysis of the coupled mode due to E_1-A_1 mode mixing. New characterization techniques should be developed in order to analyze randomly oriented nanostructures.

BIBLIOGRAPHY

[1] K. H. Hellwege, O. Madelung, A. M. Hellege, *Numerical Data and Functional Relationship in Science and Technology* (Springer-Verlag, New York, 1987).

[2] T. Sekiguchi, S. Miyashita, K. Obara, T. Shishido, and N. Sakagami, J. Cryst. Growth **214/215**, 72 (2000).

[3] T. Sakagami, M. Yamashita, T. Sekiguchi, S. Miyashita, K. Obara, and T. Shishido, J. Cryst. Growth **229**, 98 (2001).

[4] W.-J. Li, E.-W. Shi, W.-Z. Zhong, and Z.-W. Yin, J. Cryst. Growth **203**, 186 (1999).

[5] W. B. Pearson, *A Handbook of Lattice Spacing and Structures of Metals and Alloys*, V. 2, New York: Pergamon Press, 1967.

[6] International Tables for X-Ray Crystallography, The International Union of Crystallography, 1965.

[7] R. D. Vispute et al., Appl. Phys. Lett. **73**, 348 (1998).

[8] A. Mang, K. Reimann, and S. Rubenacke, Solid State Commun. **94**, 251 (1995).

[9] A. Ohtomo et al., Appl. Phys. Lett. **77**, 2204 (2000).

[10] R. P. Koffyberg, Phys. Rev. B **13**, 4470 (1976).

[11] E. R. Segnit and A. E. Holland, J. Am. Ceram. Soc. **48**, 412 (1965).

[12] W. Yang, *et al*. Appl. Phys. Lett. **78**, 18 (2002).

[13] S. M. Sze, *Physics of Semiconductor Devices*, 2nd ed. New York, 1981.

[14] D. S. Ginley and C. Bright, Mater. Res. Bull. 25, 15 (2000); E. M. Kaidashev et al., Appl. Phys. Lett. **82**, 3901 (2003).

[15] J. D. Albrecht, et al. J. Appl. Phys. **86**, 12 (1999)

[16] T. Minami, H. Sato, H. Nanto, and S. Takata, Jpn. J. Appl. Phys., Part 2 **24**, L781 (1985).

[17] D. C. Look, J. W. Hemsky, and J. R. Sizelove, Phys. Rev. Lett. **82**, 2552 (1999); D. C. Look, D. C. Reynolds, J. R. Sizelove, R. L. Jones, C. W. Litton, G. Cantwell, and W. C. Harsch, Solid State Commun. **105**, 399 (1998).

[18] J. D. Albrecht, P. P. Ruden, S. Limpijumnong, W. R. L. Lambrecht, and K. F. Brennan, J. Appl. Phys. **86**, 6864 (1991).

[19] A. F. Kohan, G. Ceder, D. Morgan, and C. G. Van de Walle, Phys. Rev. B **61**, 15019 (2000).

[20] C. G. Van de Walle, Physica B **308–310**, 899 (2001).

[21] H. Kato, M. Sano, K. Miyamoto, and T. Yao, J. Cryst. Growth 237–239, **538** (2002).

[22] S. Y. Myong, S. J. Baik, C. H. Lee, W. Y. Cho, and K. S. Lim, Jpn. J. Appl. Phys., Part 2 **36**, L1078 (1997).

[23] V. Assuncao, E. Fortunato, A. Marques, H. Aguas, I. Ferreira, M. E. V. Costa, and R. Martins, Thin Solid Films **427**, 401 (2003).

[24] B. M. Ataev, A. M. Bagamadova, A. M. Djabrailov, V. V. Mamedo, and R. A. Rabadanov, Thin Solid Films 260, **19** (1995).

[25] C. H. Park, S. B. Zhang, and S.-H. Wei, Phys. Rev. B **66**, 073202 (2002).

[26] M. L. Cohen, Phys. Scr., T T1, 5 (1982).

[27] J. Ihm, A. Zunger, and M. L. Cohen, J. Phys. C **12**, 4409 (1979).

[28] T. Sekiguchi, S. Miyashita, K. Obara, T. Shishido, and N. Sakagami, J. Cryst. Growth **214/215**, 72 (2000).

[29] T. Sakagami, M. Yamashita, T. Sekiguchi, S. Miyashita, K. Obara, and T. Shishido, J. Cryst. Growth **229**, 98 (2001).

[30] K. Matsumoto and K. Noda, J. Cryst. Growth **102**, 137 (1990).

[31] J.-M. Ntep, S. S. Hassani, A. Lusson, A. Tromson-Carli, D. Ballutaud, G. Didier, and R. Triboulet, J. Cryst. Growth **207**, 30 (1999).

[32] N. Takahashi, K. Kaiya, T. Nakamura, Y. Momose, and H. Yamamoto, Jpn. J. Appl. Phys., Part 2 **38**, L454 (1999).

[33] M. Kasuga and S. Ogawa, Jpn. J. Appl. Phys., Part 1 **22**, 794 (1983).

[34] M. Suscavage et al., MRS Internet J. Nitride Semicond. Res. 4S1, G3.40 (1999).

[35] D. C. Look, D. C. Reynolds, J. R. Sizelove, R. L. Jones, C. W. Litton, G. Cantwell, and W. C. Harsch, Solid State Commun. **105**, 399 (1998).

[36] J. G. E. Gardeniers, Z. M. Rittersma, and G. J. Burger, J. Appl. Phys. **83**, 7844 (1998).

[37] S. K. Tiku, C. K. Lau, and K. M. Lakin, Appl. Phys. Lett. **36**, 318 (1980).

[38] K.-K. Kim, J.-H. Song, H.-J. Jung, W.-K. Choi, S.-J. Park, and J.-H. Song, J. Appl. Phys. **87**, 3573 (2000); K.-K. Kim, J.-H. Song, H.-J. Jung, W.-K. Choi, S.-J. Park, J.-H. Song, and J.-Y. Lee, J. Vac. Sci. Technol. **18**, 2864 (2000).

[39] Y. Chen, D. M. Bagnall, H.-J. Koh, K.-T. Park, K. Hiraga, Z.-Q. Zhu, and T. Yao, J. Appl. Phys. **84**, 3912 (1998).

[40] R. D. Vispute et al., Appl. Phys. Lett. **73**, 348 (1998).

[41] Y. Liu, C. R. Gorla, S. Liang, N. Emanetoglu, Y. Lu, H. Shen, and M. Wraback, J. Electron. Mater. **29**, 69 (2000).

[42] Y. W. Heo, et al. Appl. Phys. Lett. **81**, 3046 (2002).

[43] Y. C. Kong, et al. Appl. Phys. Lett. **78**, 407 (2001).

[44] R. Zhang, Y. Lifshitz, and S. Lee, Adv. Mater. **15,** 635 (2003).

[45] M. H. Huang, et al. Adv. Mater. **13,** 113 (2001).

[46] S. C. Lyu, et al. Chem. Phys. Lett. **363**, 134 (2002).

[47] S. Y. Li, et al. J. Crystal Growth, **247**, 357 (2003).

[48] B. D. Yao, et al. Appl. Phys. Lett. **81**, 757 (2002).

[49] Y. S. Park, *et al*. Phys. Rev. **143**, No. 2 (1966).

[50] W. Y. Liang and A. D. Yoffe, Phys. Rev. Lett. **20**, 59 (1968).

[51] J. F. Muth, R. M. Kolbas, A. K. Sharma, S. Oktyabrsky, and J. Narayan, J. Appl. Phys. **85**, 1884 (1999).

[52] D. C. Reynolds, D. C. Look, B. Jogai, C. W. Litton, G. Cantwell, and W. C. Harsch, Phys. Rev. B **60**, 2340 (1999).

[53] A. Teke, Ü. Özgür, S. Doğan, X. Gu, H. Morkoç, B. Nemeth, J. Nause, and H. O. Everitt, Phys. Rev. B **70**, 195207 (2004).

[54] S. F. Chichibu, T. Sota, G. Cantwell, D. B. Eason, and C. W. Litton, J. Appl. Phys. **93**, 756 (2003).

[55] S. F. Chichibu, A. Tsukazaki, M. Kawasaki, K. Tamura, Y. Segawa, T. Sota, and H. Koinuma, Appl. Phys. Lett. **80**, 2860 (2002).

[56] K. Thonke, T. Gruber, N. Teofilov, R. Schönfelder, A. Waag, and R. Sauer, Physica B **308–310**, 945 (2001).

[57] C. Boemare, T. Monteiro, M. J. Soares, J. G. Guilherme, and E. Alves, Physica B **308–310**, 985 (2001).

[58] D. C. Reynolds, D. C. Look, B. Jogai, R. L. Jones, C. W. Litton, H. Harsch, and G. Cantwell, J. Lumin. **82**, 173 (1999).

[59] R. P. Wang, G. Xu, and P. Jin, Phys. Rev. B. **69**, 113303 (2004).

[60] J. F. Muth, R. M. Kolbas, A. K. Sharma, S. Oktyabrsky, and J. Narayan, J. Appl. Phys. **85**, 7884 (1999).

[61] K. Vanheusden, W. L. Warren, C. H. Seager, D. R. Tallant, J. A. Voigt, and B. E. Gnade, J. Appl. Phys. **79**, 7983 (1996). K. Vanheusden, C. H. Seager, W. L. Warren, D. R. Tallant and J. A. Voigt, Appl. Phys. Lett. **68**, 403 (1996).

[62] A. van Dijken, E. A. Meulenkamp, D. Vanmaekelberg and A. Meijerink, J. Phys. Chem. B **104**, 1715 (2000).

[63] T. Sekiguchi, N. Ohashi and Y. Terada, Jpn. J. Appl. Phys. **36**, L289 (1997).

[64] X. Liu, X. H. Wu, H. Cao and R. P. H. Chang, J. Appl. Phys. **95**, 3141 (2004).

[65] W. S. Shi, O. Agyeman, and C. N. Xu, J. Appl. Phys. **91**, 5640 (2002).

[66] B. X. Lin, Z. X. Fu, Y. B. Jia and G. H. Liao, J. Electrochemical. S. **148**, G110 (2001).

[67] M. Anpo, Y. Kubokawa, J. Phys. Chem. **88**, 5556 (1984).

[68] S. H. Bae, S. Y. Lee, H. Y. Kim and S. Im, Optic. Mater. **17**, 327 (2001).

[69] Y. G. Wang, S. P. Lau, H. W. Lee, S. F. Yu, B. K. Tay, X. H. Zhang and H. H. Hng, J. Appl. Phys, **94**, 354 (2003).

[70] J. A. Zapien, Y. Jiang, X. M. Meng, W. Chen, F. C. K. Au, Y. Lifshitz, S. T. Lee, Appl. Phys. Lett. **84**, 1189 (2004).

[71] H. Q. Yan, J. Johnson, M. Law, R.R. He, K. Knutsen, J. R. Mckinney, J. Pham, R. Saykally, P. D. Yang. Adv. Mater. **15,** 1907 (2003).

[72] J. Johnson, H. Q. Yan, P. D. Yang, R. J. Saykally, J. Phys. Chem. B **107**, 8816 (2003).

[73] X. H. Han, G. Z. Wang, Q. T. Wang, L. Cao, R. Liu, B. S. Zou, J. G. Hou, Appl. Phys. Lett. **86**, 223106 (2005).

[74] S. F. Yu, C. Yuen, S.P Lau, W. I. Park, G-C Yi, Appl. Phys. Lett. **84,** 3241(2004).

[75] H-C. Hsu, C-Y. Wu, W-F. Hsieh, J. Appl. Phys. **97**, 064315 (2005).

[76] J. C. Johnson, H. J. Choi, K. P. Knutsen, R. D. Schaller, P. D. Yang, R. J. Saykally, Nature Materials **1,** 106 (2002).

[77] Y. Xu, R. K. Lee, A. Yariv, Phys. Rev. A. **61**, 033808 (2000).

[78] J. Wiersig, Phys. Rev. A **67**, 023807 (2003).

[79] S. Chang, N. B. Rex, R. Chang, G. Chong, L. J. Guido, Appl. Phys. Lett. **75**, 166 (1999).

[80] X. Liu, W. Fang, Y. Huang, X. H. Wu, S. T. Ho, H. Cao, R. P. H. Chang, Appl. Phys. Lett. **84**, 2488 (2004).

[81] T. Nobis, E. M. Kaidashev, A. Rahm, M. Lorenz, M. Grundmann, Phys. Rev. Lett. **93**, 103903 (2004).

[82] S. Roy, S. Basu, Bull. Mater. Sci. **25**, 513 (2002).

[83] R. Katoh, A. Furube, K, Hara, S. Murata, H. Sugihara, H. Arakawa, and M. Tachiya, J. Phys. Chem B **106**, 12957 (2002).

[84] P. Sharma, S. Kumar, and K. Sreenivas, J. Mater. Res. **18**, 545 (2003)

[85] N. Ohashi, K. Kataoka, T. Ohgaki, T. Miyagi, H. Haneda, K. Morinaga, Appl. Phys. Lett. **83**, 4857 (2003).

[86] C. Y. Lee, T. Y. Tseng, S. Y. Li, and P. Lin, Tamkang J. Sci. Eng, **6**, 127 (2003).

[87] Cui.Y. Lauhon, L.J. Gudiksen, M.S. Wang, and J. Lieber, Appl. Phys. Lett. **78**, 2214 (2001).

[88] W. I. Park, D.H. Kim, S. W. Jung, and G-C. Yi, Appl. Phys. Lett. **80**, 4232 (2002).

[89] W. I. Park, Y.H. Jun, S. W. Jung, and G-C. Yi, Appl. Phys. Lett. **82**, 964 (2003).

[90] X. Liu, X. H. Wu, H. Cao, and R. P. H. Chang, J. Appl. Phys. **95**, 3141 (2004).

[91] B.P. Zhang, N.T. Binh, Y. Segawa, K. Wakatsuki, N. Usami, Appl. Phys. Lett. **83**, 1635 (2003).

[92] X. Duan, Y. Huang, Y. Cui, J.Wang, and C. M. Lieber, Nature, **409,** 66 (2001).

[93] E. M. Wong, P. C. Searson, Appl. Phys. Lett. **74,** 2939 (1999).

[94] A. E. Hichou, M. Addou, J. Ebothe, and M. Troyon, J. Lumin. **113,** 183 (2005).

[95] Q. Wan, C. L. Lin, X. B. Yu, and T. H. Wang, Appl. Phys. Lett. **84**, 124 (2004).

[96] B. D. Yao, Y. F. Chan, and N. Wang, Appl. Phys. Lett. **81**, 757 (2002).

[97] J. Y. Lao, J. Y. Huang, D. Z. Wang, and Z. F. Ren, Nano Lett. **3**, 235 (2002).

[98] D. Wang, H. W. Seo, C-C. Tin, M. J. Bozack, J. R. Williams, Y. Tzeng, and M. Park, J. Appl. Phys. **99**, 093112 (2006).

[99] A-J. Cheng, D. Wang, H. W. Seo, C. Liu, M. Park, and Y. Tzeng, Diamond & Related Matter. **15**, 426 (2006).

[100] Cui.Y. Lauhon, L.J. Gudiksen, M.S. Wang, and J. Lieber, Appl. Phys. Lett. **78**, 2214 (2001).

[101] C. Y. Lee, T. Y. Tseng, S. Y. Li, and P. Lin, Tamkang J. Sci. Eng, **6**, 127 (2003).

[102] F-Q. He, Y-P. Zhao, Appl. Phys. Lett. **88**, 193113 (2006).

[103] M. Ohring, "The Material Science of Thin Film", 1st ed. (Academic, London, 1992)

[104] A-J. Cheng, Master Thesis (2006).

[105] P. X. Gao, and Z. L. Wang, Small **1,** No.10, 945 (2005).

[106] B. A. Korgel, Science **309,** 1683 (2005).

[107] X. Y. Kong, Y. Ding, R. Yang, Z. L. Wang, Science **303**, 1348 (2004).

[108] W. Y. Liang and A. D. Yoffe, Phys. Rev. Lett. **20**, 59 (1968).

[109] D. G. Thomas, J. Phys. Chem. Solids **15**, 86 (1960).

[110] K. A. Alim, V. A. Fonobeov, A. A. Balndin, Appl. Phys. Lett. **86**, 053103 (2005).

[111] X. Liu, X. H. Wu, H. Cao and R. P. H. Chang, J. Appl. Phys. **95**, 3141 (2004).

[112] S. A. Studenikin, N. Golego, and M. Cocivera, J. Appl. Phys. **84**, 2287 (1998).

[113] L. E. Greene, M. Law, J. Goldberger, F. Kim, J. C. Johnson, Y. Zhang, R. J. Saykally, and P. Yang, Angew. Chem., Int. Ed. 42, 3031 (2003).

[114] L. Wu, Y. Wu, X. Pan, and F. Kong, Opt. Mater. **28**, 418 (2006).

[115] Y. Harada and S. Hashimoto, Phys. Rev. B **68**, 045421 (2003).

[116] I. Shalish, H. Temkin and V. Narayannamurti, Phys. Rev. B **69**, 245401 (2004).

[117] D. Li, Y. H. Leung, A. B. Djurišić, Z. T. Liu, M. H. Xie, S. L. Shi, S. J. Xu and W. K. Chan, Appl. Phys. Lett. **85**, 1601 (2004).

[118] D. Wang, N. Sathitsuksanoh, An-jen Cheng, Y. H. Tzeng, H. W. Seo, C.-C. Tin, M. J. Bozack, J. R. Williams, and M. Park, J. Appl. Phys. **99**, 113509 (2006).

[119] P. S. Xu, Y. M. Sun, C. S. Shi, F. Q. Xu, and H. B. Pan, Nucl. Instrum. Methods Phys. Res. B **199**, 286 (2003).

[120] N. E. Korsunska, L. V. Borkovska, B. M. Bulakh, L. Yu. Khomenkova, V. I. Kushnirenko and I. V. Markevich, J. Lumin.**733**, 102 (2003).

[121] E. Bylander, J. Appl. Phys. **49**, 1188 (1978).

[122] A. F. Kohan, G. Ceder, D. Morgan, and C. G. Van de Walle, Phys. Rev. B **61**, 15019 (2000).

[123] W. M. Kwok, Y. H. Leung, A. B. Djurišić, W. K. Chan, and D. L. Phillips, Appl. Phys. Lett. **87**, 093108 (2005).

[124] R. B. Lauer, J. Phys. Chem. Solids **34**, 249 (1973).

[125] C. Gaspar, F. Costa, and T. Monteiro, J. Mater. Sci.: Mater. Electron. **12**, 269 (2001).

[126] L. Bergman, M. Dutta, C. Balkas, R.F. Davis, D. Alexson, and R.J. Nemanich. J. of Appl. Physics **85**, 3535 (1999).

127 W. Hayes and R. Laudon, "Scattering of Light by Crystals", John Wiley & Sons, New York (1978).

[128] K. W. Adu, H. R. Gutierrez, U. J. Kim, G. U. Sumanasekera, and P. C. Eklund, Nano Lett. **5**, 409 (2005).

[129] L. Bergman, M. Dutta, M.A. Stroscio, R.F. Davis, and R.J. Nemanich. Phys. Rev. B. **59**, 12977,1999.

[130] C. A. Arguello, D. L. Rousseau, and S. P. S. Porto, Phys. Rev. **181**, 1351 (1969).

[131] L. Bergman, M. D. Bremser, W. G. Perry, R. F. Davis, M. Dutta, and R. J. Nemanich, Appl. Phys. Lett. 71, 2157 (1997).

[132] R. Loudon, Adv. Phys. **13**, 423 (1964).

[133] G. H. Wei, J. Zi, K. Zhang, and X. Xie, J. Appl. Phys. **82**, 4693 (1997).

[134] M. Cardona, Light Scattering in Solids II, (1982).

[135] H. J. Stolz, G. Abstreiter, Solid State Commun. **36**, 857 (1980).

[136] D. M. Bagnall, Y. F. Chen, Z. Zhu, T. Yao, S. Koyama, M. Y. Shen, T. Goto, Appl. Phys. Lett. **70**, 2230 (1997).

[137] J. A. Zapien, Y. Jiang, X. M. Meng, W. Chen, F. C. K. Au, Y. Lifshitz, S. T. Lee, Appl. Phys. Lett. **84**, 1189 (2004).

[138] H. Q. Yan, J. Johnson, M. Law, R.R. He, K. Knutsen, J. R. Mckinney, J. Pham, R. Saykally, P. D. Yang. Adv. Mater. **15,** 1907 (2003).

[139] J. Johnson, H. Q. Yan, P. D. Yang, R. J. Saykally, J. Phys. Chem. B **107**, 8816 (2003).

[140] X. H. Han, G. Z. Wang, Q. T. Wang, L. Cao, R. Liu, B. S. Zou, J. G. Hou, Appl. Phys. Lett. **86**, 223106 (2005).

[141] S. F. Yu, C. Yuen, S.P Lau, W. I. Park, G-C Yi, Appl. Phys. Lett. **84,** 3241(2004).

[142] H-C. Hsu, C-Y. Wu, W-F. Hsieh, J. Appl. Phys. **97**, 064315 (2005).

[143] J. C. Johnson, H. J. Choi, K. P. Knutsen, R. D. Schaller, P. D. Yang, R. J. Saykally, Nature Materials **1,** 106 (2002).

[144] Y. Xu, R. K. Lee, A. Yariv, Phys. Rev. A. **61**, 033808 (2000).

[145] J. Wiersig, Phys. Rev. A **67**, 023807 (2003).

[146] S. Chang, N. B. Rex, R. Chang, G. Chong, L. J. Guido, Appl. Phys. Lett. **75**, 166 (1999).

[147] X. Liu, W. Fang, Y. Huang, X. H. Wu, S. T. Ho, H. Cao, R. P. H. Chang, Appl. Phys. Lett. **84**, 2488 (2004).

[148] T. Nobis, E. M. Kaidashev, A. Rahm, M. Lorenz, M. Grundmann, Phys. Rev. Lett. **93**, 103903 (2004).

[149] H. W. Seo, D. Wang, Y. Tzeng, N. Sathitsuksanoh, C. C. Tin, M. J. Bozack, J. R. Williams, M. Park, MRS. Symp. Proc. **829,** B2.26.1 (2005).

[150] D. X. Zhao, Y. C. Liu, D. Z. Shen, Y. M. Lu, L. G. Zhang, X. W. Fan, J. Appl. Phys. **94**, 5605 (2003).

[151] P. L. Knight, A. Miller, Vertical-Cavity Surface Emitting Laser, (Springer-Verlags, 1999).

[152] A. K. Bhowmik, Appl. Opt. **39,** 3071 (2000).

[153] K. Vanheusden, W. L. Warren, C. H. Seager, D. R. Tallant, J. A. Voigt, and B. E. Gnade, J. Appl. Phys. **79**, 7983 (1996). K. Vanheusden, C. H. Seager, W. L. Warren, D. R. Tallant and J. A. Voigt, Appl. Phys. Lett. **68**, 403 (1996).

[154] A. van Dijken, E. A. Meulenkamp, D. Vanmaekelberg and A. Meijerink, J. Phys. Chem. B **104**, 1715 (2000).

[155] T. Sekiguchi, N. Ohashi and Y. Terada, Jpn. J. Appl. Phys. **36**, L289 (1997).

[156] X. Liu, X. H. Wu, H. Cao and R. P. H. Chang, J. Appl. Phys. **95**, 3141 (2004).

[157] W. S. Shi, O. Agyeman, and C. N. Xu, J. Appl. Phys. **91**, 5640 (2002).

[158] B. X. Lin, Z. X. Fu, Y. B. Jia and G. H. Liao, J. Electrochemical. S. **148**, G110 (2001).

[159] M. Anpo, Y. Kubokawa, J. Phys. Chem. **88**, 5556 (1984).

[160] S. H. Bae, S. Y. Lee, H. Y. Kim and S. Im, Optic. Mater. **17**, 327 (2001).

[161] Y. G. Wang, S. P. Lau, H. W. Lee, S. F. Yu, B. K. Tay, X. H. Zhang and H. H. Hng, J. Appl. Phys, **94**, 354 (2003).

[162] T. Inukai, M. Matsuoka, K. Ono, Thin Solid Films **257**, 22 (1995).

[163] J. D. Ye, S. L. Gu, S. M. Zhu, F. Qin, S. M. Liu, X. Zhou, L. Q. Hu, R. Zhang, Y. Shi and Y. D. Zheng, J. Appl. Phys. **96**, 5308 (2004).

[164] I. Shalish, H. Temkin and V. Narayannamurti, Phys. Rev. B **69**, 245401 (2004).

[165] T. Nobis, E. M. Kaidashev, A. Rahm, M. Lorenz, J. Lenzner and M. Grundmann, Nano Lett. **4,** 797 (2004).

[166] D. Li, Y. H. Leung, A. B. Djurišić, Z. T. Liu, M. H. Xie, S. L. Shi, S. J. Xu and W. K. Chan, Appl. Phys. Lett. **85**, 1601 (2004).

[167] Y. Harada and S. Hashimoto, Phys. Rev. B **68**, 045421 (2003).

[168] K. C. Hui, H. C. Ong, P. F. Lee and J. Y. Dai, Appl. Phys. Lett. **86**, 152116 (2005).

[169] J. Lagowski, E. S. Sproles, Jr, and H. C. Gatos. J. Appl. Phys. **48**, 3566 (1977).

[170] Chunming Jin, Ph.D. Dissertation, North Carolina State University (2003).

[171] J. F. Muth, R. M. Kolbas, A. K. Sharma, S. Oktyabrsky, and J. Narayan, J. Appl. Phys.

85, 7884 (1999).

[172] N. Y. Garces, L. Wang, L. Bai, N. C. Giles, L. E. Halliburton, and G. Cantwell, Appl. Phys. Lett. **81**, 622 (2002).

[173] N. E. Korsunska, L. V. Borkovska, B. M. Bulakh, L. Yu. Khomenkova, V. I. Kushnirenko and I. V. Markevich, J. Lumin. **102–103**, 733 (2003).

[174] N. E. Korsunska, I. V. Markevich, L. V. Borkovska, L. Yu. Khomenkova, M. K. Sheinkman and O. Yastrubchak, Physica B. **308–310**, 967 (2001).

[175] K. H. Hellwege, O. Madelung, A. M. Hellege, *Numerical Data and Functional Relationship in Science and Technology* (Springer-Verlag, New York, 1987).

[176] R. J. Kokes, J. Phys. Chem. **66**, 99 (1962).

[177] A. F. Kohan, G. Ceder, D. Morgan, and C. G. Van de Walle, Phys. Rev. B **61**, 15019 (2000).

[178] V. Gupta and A. Mansingh, J. Appl. Phys. **80**, 1063 (1996).

[179] Z. B. Fang, Z. J. Yan, Y. S. Tan, X. Q. Liu and Y. Y. Wang, Appl. Sur. Sci. **241**, 303 (2005).

[180] M. V. Klein in: Light Scattering in Solids, Ed. M. Cardona, Spinger-Verlag, Berlin, Heidelberg, New York 1975.

[181] A. Mooradian and G. B. Wright, Phys. Rev. Lett., **16**, 999 (1966).

[182] B. B. Varga, Phys. Rev. A, **137**, 1896 (1965).

[183] T. Kozawa, T. Kachi, H. Kano, Y. Taga, M. Hashimoto, N. Koide, and K. Manabe, J. Appl. Phys. **75**, 1098 (1994).

[184] P. Perlin, J. Camassel, W. Knap, T. Taliercio, J. C. Chervin, T. Suski, I. Grzegory, and S. Porowski, Appl. Phys. Lett. **67**, 2524 (1995).

[185] H. Harima, H. Sakashita, and S. Nakashima, Materials Science Forum, **264-268**, 1363 (1998).

[186] N. Wieser, M. Klose, F. Scholz and J. Off, Materials Science Forum **264**, 1351 (1998).

[187] D. Meister, M. Böhm, M. Topf, W. Kriegseis, W. Burkhardt, I. Dirnstorfer, S. Rösel, B. Farangis, B. K. Meyer, A. Hoffmann, H. Siegle, C. Thomsen, J. Christen and F. Bertram, J. Appl. Phys. **88**, 1811 (2000).

[188] H. Siegle, A. Hoffmann, L. Eckey, C. Thomsen, J. Christen, F. Bertram, D. Schmidt, D. Rudloff, and K. Hiramatsu, Appl. Phys. Lett. **71**, 2490 (1997).

[189] E. Frayssinet, W. Knap, S. Krukowski, P. Perlin, P. Wisniewski, T. Suski, I. Grzegory and S. Porowski, J. Crystal Growth **230**, 442 (2001).

[190] M. Park, J. J. Cuomo, W.-C. Yang, B. J. Rodriguez, R. J. Nemanich, O. Ambacher, J. Appl. Phys. **93**, 9542 (2003).

[191] Y. S. Park, C. M. Park, D. J. Fu, T. W. Kang, and J. E. Oh, Appl. Phys. Lett. **85**, 5718 (2004); Y. S. Park, S. H. Lee, J. E. Oh, C. M. Park, and T. W. Kang, accepted for publication in J. Crystal Growth (2005).

[192] W. Hayes and R. Laudon, "Scattering of Light by Crystals", John Wiley & Sons, New York (1978).

[193] K. A. Alim, V. A. Fonobeov, A. A. Balndin, Appl. Phys. Lett. **86**, 053103 (2005).

[194] M. Balkanski, R. F. Wallis, and E. Haro, Phys. Rev. B **28**, 1928 (1983).

[195] W. S. Li , Z. X. Shen, Z. C. Feng , S. J. Chua, J. Appl. Phys. **87**, 3332 (2000)

[196] M.S.Liu, L.A.Bursill, S. Prawer, K. Nugent, Y. Z. Tong, G. Y. Zhang, Appl. Phys. Lett. **74**, 3125 (1999).

[197] C. A. Arguello, D. L. Rousseau, S. P. S. Porto, Phys. Rev. **181**, 1351(1969).

[198] G. Irmer, V. V. Toporov, B. H. Bairamov, J. Monecke, Phys. Status. Solidi. B **119**, 595 (1983).

[199] K. H. Hellwege, O. Madelung, A. M. Hellege, *Numerical Data and Functional Relationship in Science and Technology* (Springer-Verlag, New York, 1987).

[200] F. Demangeot, J. Frandon, M. A. Renucci, C. Meny, O. Briot, R. L. Aulombard, J. Appl. Phys. **82**, 1305 (1997).

[201] M. Park, J-P. Maria, J. J. Cuomo, Y. C. Chang, J. F. Muth, R. M. Kolbas, R. J. Nemanich, E. Carlson, J. Bumgarner, Appl. Phys. Lett. **81**, 1797 (2002).

[202] S.O. Kucheyev, J.S. Williams, S.J. Pearton, Materials Science and Engineering R-Reports, **33**, (51) 2001.

[203] Y.N. Saripalli, C. Zeng, J.P. Long, D.W. Barlag, M.A.L. Johnson, D. Braddock, J. Cryst. Growth, Accepted Sept 2005.

[204] M. V. Klein in: Light Scattering in Solids, Ed. M. Cardona, Spinger-Verlag, Berlin, Heidelberg, New York 1975.

[205] A. Mooradian and G. B. Wright, "Observation of the interaction of plasmons with longitudinal optical phonons in GaAs", Phys. Rev. Lett., **16**, 999 (1966).

[206] B. B. Varga, "Coupling of plasmons to polar phonons in degenerate semiconductors", Phys. Rev. A, **137**, 1896 (1965).

[207] H. Amano, N. Sawaki, I. Akasaki, Y. Toyoda, Appl. Phys. Lett. **48**, 353 (1986).

[208] S. Nakamura, Jpn. J. Appl. Phys **30** (1991) L1705.

[209] W. Hayes and R. Laudon, "Scattering of Light by Crystals", John Wiley & Sons, New York (1978).

[210] C. Kisielowski, J. Krüger, S. Ruvimov, T. Suski, J. W. Ager III, E. Jones, Z. Liliental-Weber, M. Rubin, E. R. Weber, M. D. Bremster and R. F. Davis, Phys. Rev. B, **54**, 17745 (1996).

[211] I-H. Lee, I-H. Choi, C-R. Lee, E-J. Shin, D. Kim, S. K. Noh, S-J. Son, K. Y. Lim and H. J. Lee, J. Appl. Phys. **83**, 5787 (1998).

[212] S. Ruvimov, Z. Liliental-Weber, T. Suski, J. W. Ager III, J. Washburn, J. Krueger, C. Kisielowski, E. R. Weber, H. Amano and I. Akasaki, Appl. Phys. Lett. **69**, 990 (1996).

[213] L. T. Romano, C. G. Van de Walle, J. W. Ager, W. Götz and R. S. Kern, J. Appl. Phys.**87**, 7745 (2000).

[214] M. Balkanski, R.F.Wallis, E. Haro, Phys. Rev. B. **28**, 1928 (1983).

[215] W. S. Li, Z. X. Shen, Z. C. Feng, S. J. Chua, J. Appl. Phys. **87**, 3332 (2000).

[216] T. Kozawa, T. Kachi, H. Kano, Y. Taga, M. Hashimoto, N. Koide, K. Manabe, J. Appl. Phys. **75**, 1098 (1994).

[217] P. Perlin, J. Camassel, W. Knap, T. Taliercio, J.C.Chervin, T. Susli, I. Grzegory, S. Porowski, Appl. Phys. Lett. **67**, 2524 (1995).

[218] M. Park, J. P. Maria, J. J. Cuomo, Y. C. Chang, J. F. Muth, R. M. Kolbas, R. J. Nemanich, E. Carlson, J. Bumgarner, Appl. Phys. Lett. **81**, 1797 (2002).

[219] M. Park, J. J. Cuomo, B. J. Rodriguez, W. C. Yang, R. J. Nemanich, O. Ambacher, J. Appl. Phys. **93**, 9542 (2003).

[220] G. Irmer, V. V. Toporov, B. H. Bairamov, J. Monecke, Phys. Status. Solidi. B **119**, 595 (1983).

[221] W. L. Faust, C. H. Henry, Phys. Rev. Lett. **17**, 1265 (1996).

[222] K. H. Hellwege, O. Madelung, A. M. Hellege, Numerical Data and Functional Relationship in Science and Technology (Springer-Verlag, New York, 1987).

[223] X. L. Xu, C. D. Beling, S. Fung, Y. E. Zhao, N. F. Sun, T. N. Sun, Q. L. Zhang, H. H. Zhan, B. Q. Sun, J. N. Wang, W. K. Ge, P. C. Wong, Appl. Phys. Lett. **76**, 152 (2000).

[224] J. W. P. Hsu, D. V. Lang, S. Richter, R. N. Kleiman, A. M. Sergent, R. J. Molna, Appl. Phys. Lett. **77**, 2873 (2000).

[225] Y. Huang, X. D. Chen, S. Fung, C. D. Beling, C. C. Ling, Z. F. Wei, S. J. Xu, C. Y. Zhi, J. Appl. Phys. **96**, 1120 (2004).

[226] J. Jayapalan, B. J. Skromme, R. P. Vaudo, and V. M. Phanse, Appl. Phys. Lett. **73**, 1188 (1998).

[227] J. Neugebauer and C. G. Van de Walle, Appl. Phys. Lett. **69**, 503 (1996).

[228] G. C. Yi and B. W. Wessels, Appl. Phys. Lett. **69**, 3028 (1996).

[229] H. M. Chen, Y. F. Chen, M. C. Lee, and M. S. Feng, Phys. Rev. B **56**, 6942 (1997).

[230] H. C. Yang, T. Y. Lin, M. Y. Huang and Y. F. Chen, J. Appl. Phys. **86**, 6124 (1999).

[231] X. Zhang, P. Kung, A. Saxler, D. Walker, T. C. Wang and M. Razeghi, Appl. Phys. Lett. **67**, 1745 (1995).

[232] I.-H. Lee, I.-H. Choi, C.-R. Lee, S.-J. Son, J.-Y. Leem and S. K. Noh, J. Cryst. Growth **182**, 314 (1997).

[233] R. Seitz, C. Gaspar, T. Monteiro, E. Pereira, M. Leroux, B. Beamont and P. Gibart, J. Cryst. Growth **189-190**, 546 (1998).

[234] X. H. Wu, P. Fini, E. J. Tarsa, B. Heying, S. Keller, U. K. Mishra, S. P. Denbaars, and J. S. Speck, J. Cryst. Growth **189-190**, 231 (1998).

[235] W. Rieger, T. Metzger, H. Angeger, R. Dimitov, O. Ambacher, M. Stutzmann, Appl. Phys. Lett. **68**, 970 (1996).

[236] S. Ruvimov, Z. L. Weber, T. Suski, J. W. Ager, J. Washburn, J. Krueger, C. Kisielowski, E. R. Weber, H. Amano and I. Akasaki, Appl. Phys. Lett. **69**, 990 (1996).

[237] L.-H. Lee, J. J. Lee, P. Kung, F. J. Sanchez and M. Razeghi, Appl. Phys. Lett. **74**, 102 (1999).

[238] M. A. Reshchikov, H. Morkoc, J. Appl. Phys. **97**, 061301 (2005).

[239] J. F. Muth, J. H. Lee, I. K. Shmagin, R. M. Kolbas, H. C. Casey Jr., B. P. Keller, U. K. Mishra and S. P. DenBaars, Appl. Phys. Lett. **71**, 2572 (1997).

[240]E. Yablonovitch, K. M. Leung, Nature **351**, 278 (1991).

[241]J. G. Fleming, S. Y. Lin, Optics Letters **24**, 49 (1999).

[242]T. F. Krauss, R. M. DelaRue, S. Brand, Nature **383**, 699 (1996).

[243]U. Gruning, V. Lehmann, S. Ottow, K. Busch, Appl. Phys. Lett. **68**, 747 (1996).

[244]H. W. Lau, G. J. Parker, R. Greef, M. Holling, Appl. Phys. Lett. **67**, 1877(1995).

[245]R. Zengerle, Journal of Modern Optics **34**, 1589 (1987).

[246]G. Subramania, K. Constant, R. Biswas, M. M. Sigalas, K-M. Ho, Appl. Phys. Lett. **74**, 3933 (1999).

[247]O. D. Velev, T. A. Jede, R. F. Lobo, A. M. Lenhoff, Chem. Mater. **10**, 3597(1998).

[248]D. Kang, J. E. Maclennan, N. A. Clark, A. A. Zakhidov, R. H. Baughman, Phys. Rev. Lett. **86**, 4052 (2001).

[249]S. Asher, V. L. Alexeev, A. V. Goponenko, A. C. Sharma, I. K. Lednev, C. S. Wlicox, D. N. Finegold, J. Am. Chem. Soc. **125**, 3322 (2003).

[250]V. L. Alexeev, A. C. Sharma, A. V. Goponenko, S. Das, I. K. Lednev, C. S. Wilcox, D. N. Finegold, S. Asher, Anal. Chem. **75**, 2316 (2003).

[251]K. Lee, S. Asher, J. Am. Chem. Soc. **122**, 9534 (2000).

[252]A. Blanco, C. Lopez, R. Mayoral, H. Miguez, F. Meseguer, A. Mifsud, J. Herrero, Appl. Phys. Lett. **73**, 1781 (1998).

[253]R. D. Pradhan, J. A. Bloodgood, G. H. Watson, Phys. Rev. B **55**, 9503 (1997).

[254]R. M. Amos, J. G. Rarity, P. R. Tapster, T. J. Shepherd, Phys. Rev. E **61**, 2929 (1999).

[255]S. Wong, V. Kitaev, G. A. Ozin, J. Am. Chem. Soc. **125**, 15589 (2003).

[256]H. Miguez, S. M. Yang, G. A. Ozin, Appl. Phys. Lett. **81**, 2493(2002).

[257]Y. A. Vlasov, X. Z. Bo, J. C. Sturm, D. J. Norris, Nature (London) **414**, 289 (2001).

[258]A. S. Dimitrov, K. Nagayama, Langmuir **12**, 1303(1996).

[259]H-Y. Ko, J. Park, H. Shin, J. Moon, Chem.Mater. **16**, 4212 (2004).

[260]J. Aizenberg, P. V. Braun, P. Wilzius, Phys.Rev.Lett. **27**, 2997 (2000).

[261]Y-H. Ye, S. Badilescu, V-V. Truong, Appl. Phys. Lett. **79**, 872 (2001).

[262]K. M. Chen, X. Jiang, L. C. Kimerling, P. T. Hammond, Langmuir **16**, 7825 (2000).

[263]Y. Yin, Z-Y. Li, Y Xia, Langmuir **19**, 622 (2003).

[264]D. Wang, M. Park, J. Park, J. Moon, Appl. Phys. Lett. **86**, 241114 (2005).

[265]N. W. Ashcroft and N. D. Mermin, "Solid State Physics", W. B. Saunders Company, (1976).

[266]M. Patrini, M. Galli, M. Belotti, L. Andreani, and G. Guizzetti, J. Appl. Phys. **92**, 1816 (2002).

[267]M. Haurylau, S. M. Weiss, and P. M. Fauchet, Proc. of SPIE 5511, **38** (2004).

[268]M. Qiu, Appl. Phys. Lett. **81**, 1163 (2002).

[269]W. L. Vos, R. Sprik, A. V. Blaaderen, A. Imhof, A. Lagendijk, G. H. Wegdam, Phys. Rev. B. **53**, 16231 (1996).

[270]I. E. Psarobas, Opt. Comm. **162**, 21 (1999).

[271]K. W.-K. Shung, Y. C. Tsai, Phys. Rev. B **48**, 11265 (1993)

[272]D. M. Mittleman, J. F. Bertone, P. Jiang, K. S. Hwang, V. L. Colvin, J. Chem. Phys. **111**, 345 (1999)

APPENDIX

OPTICAL PROPERTY OF A SINGLE DROPLET OF PHOTONIC CRYSTALS ASSEMBLED BY INK-JET PRINTING

Introduction

Photonic crystal (PC) or photonic band gap material is a material that possesses a periodic modulation of the refractive index. Such a material exhibits a so-called photonic band gap where certain ranges of frequencies of the electromagnetic waves cannot propagate, which is analogous to the electronic band gap in semiconductors. By tailoring the photonic band gap, light can be manipulated in a photonic crystal.

Shortly after the first proposal for photonic crystals, efforts have been made to fabricate the 3D-PC structure. The first 3D-PC fabricated by Yablonovitch[240] was mechanically drilled out of a dielectric block. To reduce the size of the PC structure into the optical regime, top-down techniques like lithography and etching techniques as well as multiple laser beam interference were utilized to create 3D periodicity in semiconductor materials.[241, 242, 243, 244, 245] An alternative way to synthesize 3D crystals is to make use of self-assembly of colloidal suspensions, which does not require the use of elaborate microfabrication technique. The as-grown 3D colloidal PC can be used as

precursors or template to fabricate other more complex photonic structure like inverted opals.[246, 247] 3D colloidal PC provides a versatile backbone structure into which functional substances can be infiltrated to make active optic components and sensors.[248, 249, 250, 251] Early PCs based on colloidal particles were synthesized by gravitational sedimentation of close-packed colloidal spheres in solution; a process often takes days or weeks, depending on the volume concentration either fcc or bcc structure can be formed.[252] Another route to fabricating 3D-PC is to use charged colloidal spheres in solution, where the electrostatic forces between the colloidal spheres that control the crystallization can be regulated by pH of the liquid.[253] To improve the crystallization quality, controlled shear stress was applied during the crystal growth, forming a large-area twinned fcc single crystal.[254] A widely employed method to form colloidal PCs is controlled drying also known as convective self-assembly.[255, 256, 257, 258] This technique can produce single-crystal planar films with controlled thickness.

The colloidal PCs studied in this work is produced by the self-assembly of monodisperse polystyrene colloidal spheres into hemispherical colloidal aggregates of internally ordered structure. The aggregates are formed from colloidal droplets patterned on the substrate by ink-jet printing as the solvent is rapidly removed from the droplet.[259] Unlike many other techniques of patterned growth of colloidal PCs,[260, 261, 262, 263] the substrate does not need to be patterned first and no template is needed, i.e., the droplet itself serves as the template. This technique has the potential to produce more complex patterns.

To study a photonic band gap effect, reflectance or transmission spectroscopy is often employed. Optical stop band will be manifested as a positive and negative peak in

reflectance and transmission spectrum, respectively. For a photonic crystal deposited on an opaque material such as silicon, reflectance spectroscopy is the only choice. Due to the small size of the individual droplets (~10 μm in diameter), it is difficult to obtain the reflectance spectrum using a conventional reflectance spectroscopy. Although several research groups have studied the optical properties of microstructured photonic crystals either microscopically or macroscopically,[256, 263] little has been done to study the optical response of a 3-dimensionally confined photonic crystal microstructure like this hemispherical photonic crystal droplet. This work thus provides some insight into the optical properties of this kind of photonic structure. In our investigation, we used micro-reflectance spectroscopy and successfully collected a reflectance spectrum from an individual colloidal droplet. The photonic crystal samples investigated in this work were contributed by Jungho Park and Jooho Moon at Yonsei University, Seoul, Korea.

Experiment

The array of droplets of the photonic crystal was prepared on silicon wafers using an ink-jet printing method. The colloidal ink containing monodispersed polystyrene particles was injected through the nozzle in the ink-jet printer. As the ink dries, the colloidal particles were self-organized to form the three-dimensional fcc lattice. Samples with three different colloidal sizes (190 nm, 210 nm, and 270 nm in diameter) of polystyrene particles were prepared. The details of the fabrication process can be found elsewhere.[259]

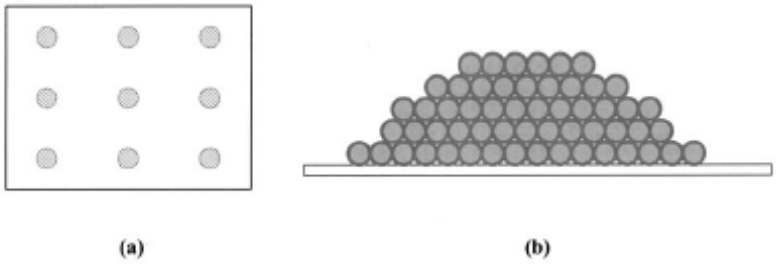

Figure A.1: Schematic diagram of the (a) plan view of the array of the droplet of PC with PS colloidal particles, and (b) side view of the individual droplet.

Atomic force microscopy (AFM) was performed using a Nanonics Imaging NSOM/SPM-1000 with a glass probe. The AFM image was collected using a tapping-mode. Micro-reflectance spectroscopy was carried out using a Zeiss microscope coupled with a light source and a spectrometer. The sample was irradiated using a UV/visible light source (DT-1000 Ocean Optics). The light from the broadband light source was focused onto a single droplet of colloidal aggregate *via* a microscope objective lens. Micro-reflectance spectra were collected using Jobin-Yvon's TRIAX 550 spectrometer equipped with a thermoelectrically-cooled charge coupled device (CCD) detector. The spectral position and the full-width-at-half-maximum (FWHM) of the reflectance peaks were determined by fitting the spectrum with a Lorentzian function. Bruggeman's and Maxwell-Garnett's effective medium approximation were used to model the dielectric properties of the colloid/air composite.

Result and Discussion

Figure A.1 shows the schematic diagram of the droplet of photonic crystal with polystyrene particles. Visual observation through an optical microscope yields three distinct colors for the droplets with different colloidal particle sizes. Figure A.2 shows the AFM images of the sample with colloidal particles with 210 nm and 270 nm in diameter. It can be clearly seen that the arrangement of the colloidal particle matches that of the (111) plane of an fcc crystal. According to the manufacturer, the error in the size distribution is approximately 3%.

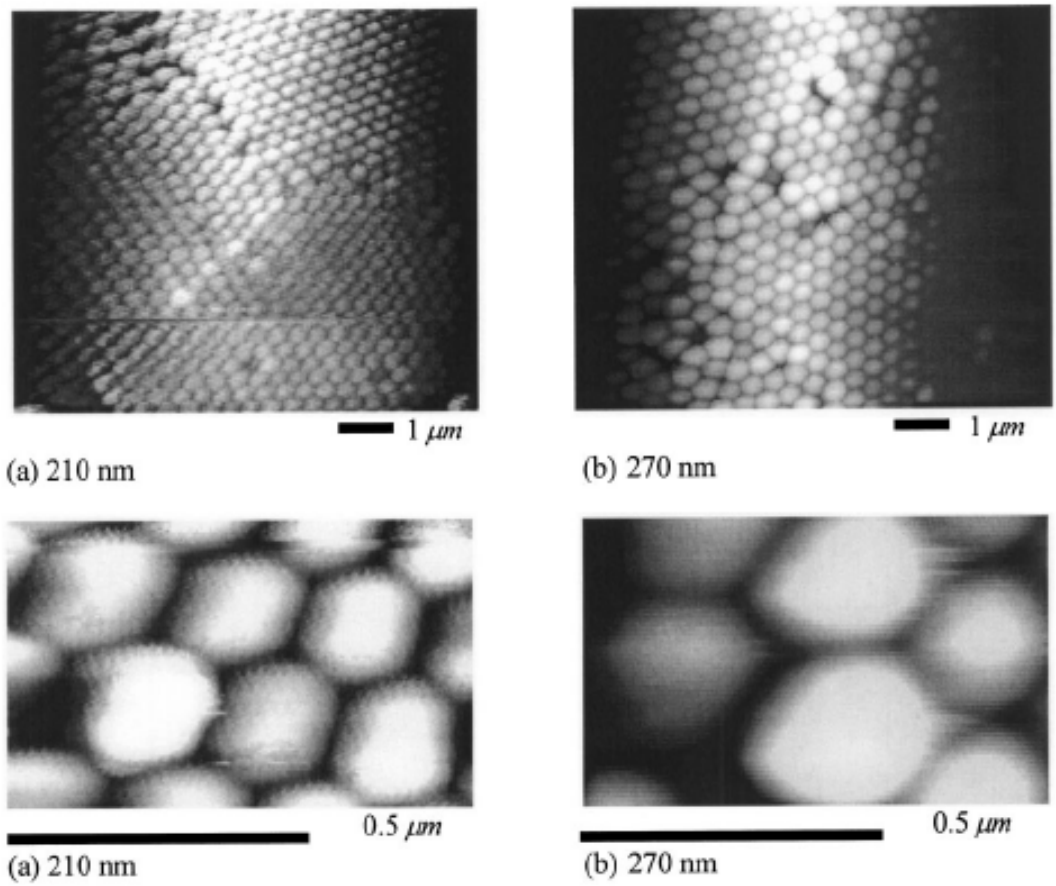

Figure A.2: AFM image of colloidal photonic crystal islands assembled from different sized polystyrene particles: (a) 210 nm and (b) 270 nm. (Ref. 264)

Figure A.3 shows the reflectance spectra of a single photonic crystal droplet which is composed of colloidal particles of one size. The 3 different spectra correspond to 3 different particle sizes (190 nm, 210 nm, and 270 nm). As the particle size increases, the position of the reflectance peak shifts to a longer wavelength, implying that the position of the photonic band gap shifts to lower energy (Figure A.2.).

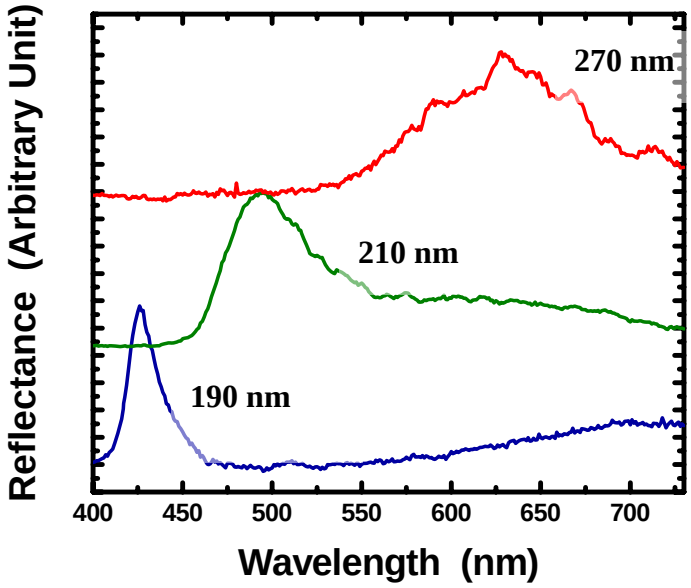

Figure A.3: Micro-reflectance spectra of a single PC droplet which is composed of colloidal particles of one size. The three different spectra correspond to three different particle sizes (190 nm, 210 nm, and 270 nm).

Constructive interference will occur when the wavevector of the incident and scattered beam satisfy the following relations[265]; $\boldsymbol{G}_{hkl} = \boldsymbol{k'} - \boldsymbol{k}$, where $\boldsymbol{G}$ is the reciprocal lattice vector, hkl represents Miller indices, and $\boldsymbol{k'}$ and $\boldsymbol{k}$ are wavevectors of the incident and scattered beam, respectively. Bragg's law can be expressed as;

$$\frac{\lambda}{n_{eff}} = 2d \sin\theta \qquad \text{(A.1)}$$

where λ is the wavelength of the light, d is the interplanar spacing, θ is the Bragg angle, and n_{eff} is the effective refractive index of the material. In the fcc crystal, interplanar spacing of (111) plane, d_{111}, can be expressed in terms of the diameter of the colloidal particle D; $d_{111} = 0.816D$. In the case of normal incidence (Bragg angle θ = 90˚) to a fcc crystal, the Bragg's law can be expressed as; $\lambda_{max} = 2 \times 0.816 \cdot n_{eff} \cdot D$.

Theoretical effective refractive indices (n_{eff}) were obtained *via* Bruggeman's effective medium theory;[266, 267, 268]

$$f \frac{\varepsilon_{ps} - \varepsilon_{eff}}{\varepsilon_{ps} + 2\varepsilon_{eff}} + (1-f) \frac{\varepsilon_{air} - \varepsilon_{eff}}{\varepsilon_{air} + 2\varepsilon_{eff}} = 0 \qquad \text{(A.2)}$$

where f is the filling fraction of the colloidal/air composite (f = 0.74 for fcc lattice), ε_{ps} ($=n_{ps}^2$), ε_{air} ($=n_{air}^2$), ε_{eff} ($=n_{eff}^2$) are dielectric constants of polystyrene, air, and effective dielectric constant, respectively. According to the Maxwell-Garnett effective medium approximation; [269, 270]

$$\frac{\varepsilon_{eff} - \varepsilon_{air}}{\varepsilon_{eff} + 2\varepsilon_{air}} = f \frac{\varepsilon_{ps} - \varepsilon_{air}}{\varepsilon_{ps} + 2\varepsilon_{air}} \qquad \text{(A.3)}$$

The effective dielectric constants, effective refractive indices, and theoretical and observed reflectance peak positions are tabulated in Table A.1. Figure A.4 shows a plot of peak position *vs.* diameter of the colloid. It can be clearly seen that the observed peak positions fit fairly well with the theoretical predictions based on both Bruggeman and Maxwell-Garnett. Therefore, it can be concluded that the Bragg's law and effective medium theories which describe the propagation of light in a photonic crystal can still be applied to microstructures as small as 10 μm in diameter (approximately 30 to 50 of polystyrene beads across the droplets).

Table A.1: The effective dielectric constants, effective refractive indices, and theoretical and observed reflectance peak positions.

Diameter (nm)	ε_{eff}^{B}	ε_{eff}^{MG}	n_{eff}^{B}	n_{eff}^{MG}	λ^{B} (nm)	λ^{MG} (nm)	λ^{exp} (nm)
190	2.05	2.00	1.43	1.41	443.7	438.6	428
210	2.05	2.00	1.43	1.41	490.4	484.8	501
270	2.05	2.00	1.43	1.41	630.5	623.3	633

Note: $\varepsilon_{ps} = (1.59)^2$ and $\varepsilon_{air} = 1.0$

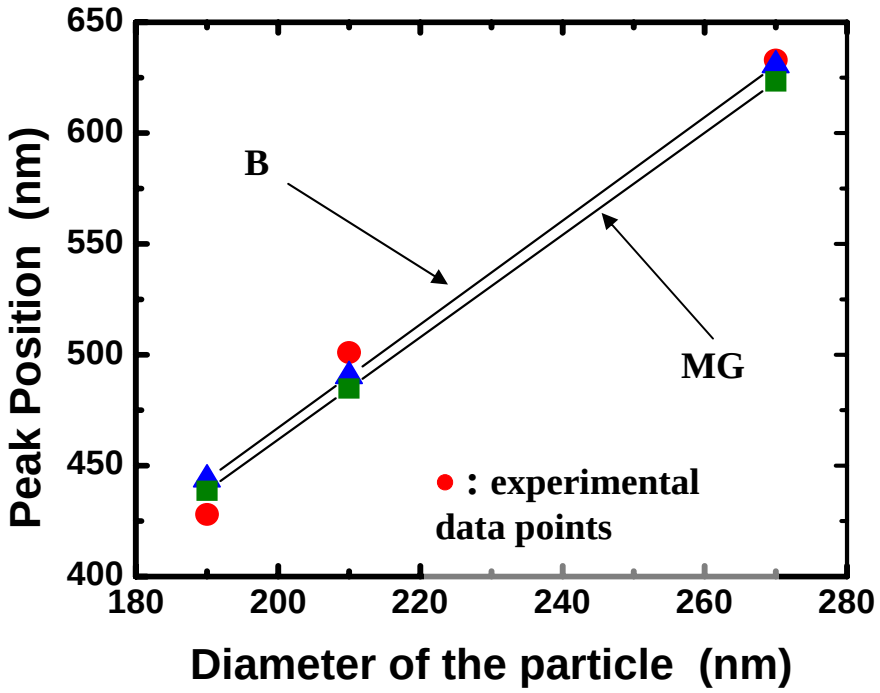

Figure A.4: Experimental observed peak position *vs.* diameter of the colloid was plotted along with the curves predicted by Bragg's law and the effective medium approximations (labeled as B and MG).

We also observed the broadening of the reflection peak as the size of the polystyrene bead increases. This broadening may be related to the higher density of defects in the photonic crystal made of larger beads, or it can be attributed to the fact that there are less repeating units in the photonic crystal made of larger beads than in the one made of smaller beads. Details of the microstructure-property relationship of the photonic crystal droplets are being investigated.

Figure A.5 shows the reflection spectra for photonic crystal islands made of the same polystyrene particles (190 nm) but with different island sizes. The primary reflection peak for the largest photonic crystal island is located at 442 nm, which is in excellent agreement with the Bragg's law and effective medium theory. Besides the strong reflection peak at 442 nm, there are also some sidebands at longer wavelength region, which is probably due to the constructive interference between the top and bottom layer of the photonic crystal island.[271]

The primary reflection peak was broadened and the intensity of the sideband reflection peaks was increased, when the size of the PC island was reduced. The former can be simply explained as a result of the diffraction of reflected light when the size of the island is small, which is similar to the peak broadening observed in X-ray diffraction experiments. The latter can be understood when one realizes that due to the hemispherical shape of the island, the height of the island will scale in the same way as the diameter of the island. Thus the height is also reduced, and at certain range it may enhance the interference between the top layer and bottom layer of the photonic crystal island. However, because of the shape of the island, the top and bottom layer are not parallel to each other, therefore the interference peaks are not regularly spaced in the reflection spectrum as usually occurred in planar photonic crystals.[272]

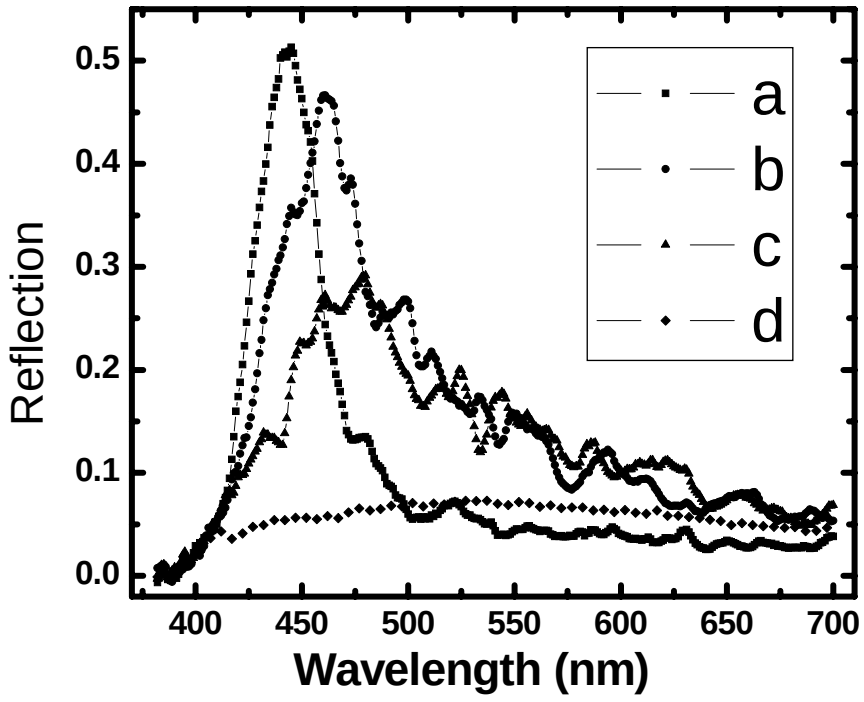

Figure A.5: Micro-reflection spectrum for photonic crystal islands made of the same polystyrene particles (190 nm) but with different island sizes. The approximate diameters of the islands are (a) 15 μm, (b) 7 μm, (c) 4 μm and (d) 2 μm.

As the size of the photonic crystal island decreases, the primary reflection peak shifts to a longer wavelength. It is speculated that inter-particle spacing between the polystyrene particles may be increased as the size of the island decreases. However, further investigation is needed to verify this hypothesis.

Conclusions

In summary, micro-reflection spectra of hemispherical photonic crystal islands have been collected. The polystyrene colloids with three different sizes (190 nm, 210 nm, and 270 nm in diameter) were used and the polystyrene colloidal particles were self-assembled to form fcc lattices with three different lattice spacing. It was observed from the reflectance spectra that the position of the optical stop band shifts as the size of the colloidal particle changes. The observed reflectance peak position fit well to the theoretical predictions based on Bruggeman and Maxwell-Garnett effective medium approximations. For large photonic crystal island with a diameter of ~10 μm, the behavior of the reflection peaks can be well described by Bragg's law and effective medium approximations; however, no reflection peaks were observed when the size of the island was smaller than ~2 μm. As the size of the island decreases, the primary reflection peak shifts to longer wavelength and its intensity decreases. The photonic crystal arrays may find application in biosensing.